LEABHARLANN CHOLÁISTE NA TRÍONÓIDE, BAILE ÁTHA CLIATH | TRINITY COLLEGE LIBRARY DUBLIN
Ollscoil Átha Cliath | The University of Dublin

Terms and Conditions of Use of Digitised Theses from Trinity College Library Dublin

Copyright statement

All material supplied by Trinity College Library is protected by copyright (under the Copyright and Related Rights Act, 2000 as amended) and other relevant Intellectual Property Rights. By accessing and using a Digitised Thesis from Trinity College Library you acknowledge that all Intellectual Property Rights in any Works supplied are the sole and exclusive property of the copyright and/or other IPR holder. Specific copyright holders may not be explicitly identified. Use of materials from other sources within a thesis should not be construed as a claim over them.

A non-exclusive, non-transferable licence is hereby granted to those using or reproducing, in whole or in part, the material for valid purposes, providing the copyright owners are acknowledged using the normal conventions. Where specific permission to use material is required, this is identified and such permission must be sought from the copyright holder or agency cited.

Liability statement

By using a Digitised Thesis, I accept that Trinity College Dublin bears no legal responsibility for the accuracy, legality or comprehensiveness of materials contained within the thesis, and that Trinity College Dublin accepts no liability for indirect, consequential, or incidental, damages or losses arising from use of the thesis for whatever reason. Information located in a thesis may be subject to specific use constraints, details of which may not be explicitly described. It is the responsibility of potential and actual users to be aware of such constraints and to abide by them. By making use of material from a digitised thesis, you accept these copyright and disclaimer provisions. Where it is brought to the attention of Trinity College Library that there may be a breach of copyright or other restraint, it is the policy to withdraw or take down access to a thesis while the issue is being resolved.

Access Agreement

By using a Digitised Thesis from Trinity College Library you are bound by the following Terms & Conditions. Please read them carefully.

I have read and I understand the following statement: All material supplied via a Digitised Thesis from Trinity College Library is protected by copyright and other intellectual property rights, and duplication or sale of all or part of any of a thesis is not permitted, except that material may be duplicated by you for your research use or for educational purposes in electronic or print form providing the copyright owners are acknowledged using the normal conventions. You must obtain permission for any other use. Electronic or print copies may not be offered, whether for sale or otherwise to anyone. This copy has been supplied on the understanding that it is copyright material and that no quotation from the thesis may be published without proper acknowledgement.

On the Acoustics of Installed Subsonic Jets

Ciarán J. O'Reilly

A thesis submitted to the University of Dublin in part-fulfilment of the requirements for the degree of

Doctor of Philosophy

Department of Mechanical and Manufacturing Engineering,

Trinity College Dublin,

February 2009.

TRINITY COLLEGE
16 AUG 2000
LIBRARY DUBLIN

Declaration

This thesis has not been submitted previously as an exercise for a degree at this or any other university. Except where otherwise acknowledged, the research is entirely the work of the author. Permission is granted for the library of Trinity College Dublin to lend or copy this thesis upon request.

Ciarán J. O'Reilly

February 2009

Summary

The reduction of community exposure to aircraft noise is an important consideration in the design of future aircraft. A review is currently under way of novel aircraft configurations, which may exploit the fuselage, wings and empennage, as acoustic shields in order to reduce the engine noise transmitted towards the ground during take-off and approach. To assess the acoustic benefits attainable with such configurations, suitable design evaluation methodologies must firstly be developed. The complex physical noise sources must be represented in a manner appropriate for input into propagation methods.

In this thesis, the development of an innovative methodology to compute the reduction in the sound pressure level from a shielded jet configuration is described. Analyses centres on the European FP6 NACRE project's wind-tunnel test programme, in which a simplified jet shielding configuration was examined. Directional point sources are located from the mean flow properties of a Reynolds-averaged Navier-Stokes solution using a variation on Lighthill's acoustic analogy.

The location of these sources is calibrated with the source locations identified from the test data. A scheme is introduced to divide the jet into sub-volumes. This limits the number of sources retained to represent jet noise in propagation codes, and therefore, reduces the computational demand required for a jet shielding prediction. A numerical approach, to include the refractive effects of the mean-flow in jet noise propagation, is outlined. The shielding factor from this source distribution is evaluated using the Fresnel-Kirchhoff method.

Isolated and shielded predictions have been made for a NACRE test case, at a range of frequencies, and compared with the available data. Good agreement with

isolated data may be achieved using the proposed jet model. However, shielding predictions over-value the reduction in sound pressure level when compared with the NACRE values.

A thorough discussion is made of the possible causes of this disagreement, and of the implications of these results. Many important trends and considerations have been identified, in this thesis, which may guide future investigations into the acoustics of installed jets.

Acknowledgments

There have been a lot of people over the past few years who have given me their support, and inspired my thoughts. I thank them all! A few people, in particular though, deserve special acknowledgement, for without them, it is hard to imagine where I would be today.

Firstly, my parents, Seán and Geraldine – your unconditional support, throughout my life, is deeply appreciated. Although Russia can not be seen from our home, with parents like you, the horizon of possibilities is a very long way off.

The rest of my family – John (and all his family), Declan (regular supplier of free coffee to this "poor student") and Gerald – I might not be able to choose my brothers, but if I could, I would pick you all (well, maybe not Ger... "Ahh, poor wee Ger!"... I love him just the same!).

If Carlsberg made PhD supervisors they would all be like Henry. Thank you for all the discussion and value-added guidance! I am very grateful. Thank you, also, to the rest of the staff in the Parsons Building!

I have had the pleasure of sharing the "dungeon" with a lot of great people throughout my time there – Eoin, Sebastien, Aviral, Erik, Jens, Alessandro – but in particular Enda, Bharath, Leandro and Cathal. I can not overstate the value to me (of some) of the conversations I have had with you.

Saving the best for last, I would like to say a special thank you to Clare – my girlfriend, "partner", friend,..., and much more! I am forever grateful for your patience and support over the years. I can only hope that your exposure to unhealthy levels of *jet noise* will have no long-term repercussions!

Summary

The reduction of community exposure to aircraft noise is an important consideration in the design of future aircraft. A review is currently under way of novel aircraft configurations, which may exploit the fuselage, wings and empennage, as acoustic shields in order to reduce the engine noise transmitted towards the ground during take-off and approach. To assess the acoustic benefits attainable with such configurations, suitable design evaluation methodologies must firstly be developed. The complex physical noise sources must be represented in a manner appropriate for input into propagation methods.

In this thesis, the development of an innovative methodology to compute the reduction in the sound pressure level from a shielded jet configuration is described. Analyses centres on the European FP6 NACRE project's wind-tunnel test programme, in which a simplified jet shielding configuration was examined. Directional point sources are located from the mean flow properties of a Reynolds-averaged Navier-Stokes solution using a variation on Lighthill's acoustic analogy.

The location of these sources is calibrated with the source locations identified from the test data. A scheme is introduced to divide the jet into sub-volumes. This limits the number of sources retained to represent jet noise in propagation codes, and therefore, reduces the computational demand required for a jet shielding prediction. A numerical approach, to include the refractive effects of the mean-flow in jet noise propagation, is outlined. The shielding factor from this source distribution is evaluated using the Fresnel-Kirchhoff method.

Isolated and shielded predictions have been made for a NACRE test case, at a range of frequencies, and compared with the available data. Good agreement with

isolated data may be achieved using the proposed jet model. However, shielding predictions over-value the reduction in sound pressure level when compared with the NACRE values.

A thorough discussion is made of the possible causes of this disagreement, and of the implications of these results. Many important trends and considerations have been identified, in this thesis, which may guide future investigations into the acoustics of installed jets.

Acknowledgments

There have been a lot of people over the past few years who have given me their support, and inspired my thoughts. I thank them all! A few people, in particular though, deserve special acknowledgement, for without them, it is hard to imagine where I would be today.

Firstly, my parents, Seán and Geraldine – your unconditional support, throughout my life, is deeply appreciated. Although Russia can not be seen from our home, with parents like you, the horizon of possibilities is a very long way off.

The rest of my family – John (and all his family), Declan (regular supplier of free coffee to this "poor student") and Gerald – I might not be able to choose my brothers, but if I could, I would pick you all (well, maybe not Ger... "Ahh, poor wee Ger!"... I love him just the same!).

If Carlsberg made PhD supervisors they would all be like Henry. Thank you for all the discussion and value-added guidance! I am very grateful. Thank you, also, to the rest of the staff in the Parsons Building!

I have had the pleasure of sharing the "dungeon" with a lot of great people throughout my time there – Eoin, Sebastien, Aviral, Erik, Jens, Alessandro – but in particular Enda, Bharath, Leandro and Cathal. I can not overstate the value to me (of some) of the conversations I have had with you.

Saving the best for last, I would like to say a special thank you to Clare – my girlfriend, "partner", friend,..., and much more! I am forever grateful for your patience and support over the years. I can only hope that your exposure to unhealthy levels of *jet noise* will have no long-term repercussions!

The author would like to thank the European Commission and the NACRE project (contract number AIP4-CT-2005-516068) partners for their funding and collaboration.

Contents

Summary i

Acknowledgments iii

List of Figures xi

List of Tables xiii

1 Introduction 1

1.1 Motivation 2

1.2 Jet Noise Shielding 4

1.3 Defining a Jet Noise Source 6

1.4 Propagation of Acoustic Sources 8

1.5 Scope of Thesis 10

1.6 Structure of Thesis 10

2 Acoustic Propagation and Scattering Prediction 13

2.1 Acoustic Propagation Equations 13

2.1.1 The Linearised Euler Equations 14

2.1.2 Wave Equations 15

2.1.3 Frequency Domain Equations 16

2.2 Numerical Methods 16

2.2.1 Discretisation Methods 16

2.2.2 High-Frequency Methods 20

2.3 Discussion 22

3 Jet Noise Modelling **23**

3.1 Review of Jet Noise Theory and Modelling 23

3.2 Lighthill's Acoustic Analogy 27

3.2.1 Solving Lighthill's Equation 28

3.2.2 Modelling the Correlation Tensor 30

3.2.3 Far-Field Spectral Density 34

3.3 The Tam-Auriault Method 34

3.3.1 Solving the Adjoint Formulation 35

3.3.2 Modelling the Source Term 37

3.3.3 Adjoint Green's Function 37

3.4 RANS Input 38

3.5 Discussion 39

4 A Jet Source Localisation Strategy **41**

4.1 A Jet Noise Model for Shielding Applications 41

4.2 Point Source Distribution for Shielding Applications 45

4.3 Reducing the Number of Sources 46

4.3.1 Defining the Jet Volume 47

4.3.2 Localisation of Jet Sources 48

4.3.3 Selecting Sub-Volume Dimensions 49

4.4 Jet Noise Shielding Prediction 52

4.5 Mean Flow Refraction Effect 54

4.5.1 Wave Expansion Discretisation 55

4.5.2 Implementation of WEM Boundary Conditions 57

4.6 Discussion 58

5 Jet Noise Shielding Assessment **61**

5.1 Jet Test Setup 61

5.2 Jet RANS Computations 68

5.3 Full Source Model Predictions 70

5.3.1 Jet Model Calibration 70

5.3.2 Isolated Model Predictions 75

5.3.3 Source Location Effect 80
5.4 Jet Spatial Volume 83
5.5 Jet Source Reduction Schemes 86
5.5.1 Uniform Sub-Volumes 86
5.5.2 Scaled Sub-Volumes 90
5.5.3 Computational Savings 94
5.6 Mean Flow Propagation Effects 96
5.6.1 Source Convection 96
5.6.2 Flow Refraction 99
5.7 NACRE Partner's Predictions 101
5.8 Summary 103

6 Discussion **105**
6.1 A Lack of Shielding? 105
6.1.1 The Role of Jet Noise Models 106
6.1.2 Alternative Propagation Paths 108
6.1.3 Near-Field Shield Location Effects 110
6.1.4 Pylon Effects 113
6.2 Remaining Considerations 114
6.2.1 Increasing the Shielded Amplitude 114
6.2.2 Two Frequency Regimes 114
6.2.3 Is Jet Noise Shielding a Practical Possibility? 115
6.2.4 The Shielding Factor as a Measure? 115
6.3 New Areas of Interest 116

7 Conclusions **119**

A The Wave Expansion Method **121**
A.1 In Inhomogeneous, Irrotational, Steady Flows 121
A.2 Wave Expansion Discretisation 122
A.3 Implementation of WEM Boundary Conditions 124

Bibliography 124

List of Figures

1.1 NACRE's Pro-Green configuration. 3
1.2 Turbofan engine noise components. 4
1.3 Shielding of a point-source by a flat plate. 5
1.4 Noise-producing regions in a simple jet. 6
1.5 BEM propagation onto an airframe geometry. 9

4.1 Schematic of spacing strategy. 51
4.2 Schematic of the jet sub-volumes. 52
4.3 Schematic of the Fresnel-Kirchhoff shielding method. 53
4.4 Wave expansion discretisation stencil. 56
4.5 A Kirchhoff surface external to the jet flow. 58
4.6 Radiation of a point source in a sheared flow. 59

5.1 View of the isolated nozzle in CEPRA19. 62
5.2 View of the nozzle installed over the shield in CEPRA19. 62
5.3 Location of the microphone arrays. 64
5.4 View of the nozzle installed over the shield with pylon. 64
5.5 Isolated SPLs measured at the flyover arc. 65
5.6 Location of EUROPIV shield. 65
5.7 Shielding factor measured at the flyover arc. 66
5.8 Beam-forming axial source localisation. 66
5.9 Noise spectrum at the flyover arc. 67
5.10 Dassault's $\kappa - \epsilon$ RANS solution. 69
5.11 Axial calibration: source power distribution. 71

5.12 Axial calibration: jet models axial source power distribution. 72
5.13 Beam-forming axial source location: jet models. 73
5.14 Uncalibrated jet models: isolated SPL directivity. 76
5.15 Calibrated jet models: isolated SPL directivity. 77
5.16 Noise spectra: jet models. 78
5.17 Axial source location: isolated SPL directivity. 81
5.18 Axial source location: shielding factor directivity. 82
5.19 Axial model: isolated SPL directivity. 84
5.20 Axial model: shielding factor directivity. 85
5.21 Source reduction using uniform blocks: isolated SPL directivity. . . . 87
5.22 Source reduction using uniform blocks: shielding factor directivity. . 88
5.23 Source reduction using uniform blocks: source residual. 89
5.24 Source reduction using scaled blocks: isolated SPL directivity. 91
5.25 Source reduction using scaled blocks: shielding factor directivity. . . 92
5.26 Source reduction using scaled blocks: source residual. 93
5.27 Computatinal time of the FKM against the number of sources. . . . 95
5.28 Source convection: isolated SPL directivity. 97
5.29 Source convection: shielding factor directivity. 98
5.30 Flow refraction: isolated SPL directivity. 99
5.31 Flow refraction: shielding factor directivity. 100
5.32 EUROPIV model for Dassault's BEM computation. 101
5.33 NACRE partners: isolated SPL directivity. 102
5.34 NACRE partners: shielding factor directivity. 102

6.1 Shielding factor from monopoles at jet exit. 106
6.2 Point source with the EUROPIV and nozzle. 109
6.3 Shield approximations: shielding factor from a monopole. 109
6.4 Shield generated noise: RANS for installed NACRE configuration. . 111
6.5 Shield generated noise: shielding factor directivity. 111

List of Tables

5.1 NACRE jet flow conditions. 68
5.2 Calibrated Model constant values. 70
5.3 Number of point sources for each of the source distributions. 94

Chapter 1

Introduction

> *"Given for one instant an intelligence, which could comprehend all the forces by which nature is animated and the respective positions of the beings which compose it,... nothing would be uncertain, and the future as the past would be present before its eyes."*
>
> – Pierre Simon de Laplace

> *"Should I refuse a good dinner simply because I do not understand the process of digestion?"*
>
> – Oliver Heaviside

Aircraft noise has long been a major concern to residents around airports. Over the past 20 years, air travel has grown by an average of 4.8% each year. Latest long-term predictions by Airbus [3] and Boeing [14] forecast an average annual growth rate of 5% for the period between 2007 and 2027. This means that the number of aircraft will double over the next 15 years. It is accepted that future industry growth is likely to depend on further reductions in the environmental impact of airline operations [21].

The prediction of noise generation and radiation from turbulent flows has been the subject of continuous research for over 50 years, however, the essential problem in modelling this noise source remains the limited knowledge of the properties of

turbulence [51]. Ever-increasing numerical simulation capabilities offer the prospect of an aid to understanding the most fundamental aspects of the physics of turbulent noise source mechanisms. For the moment though, complete simulation of the jet turbulence and the noise it generates and radiates is still too computationally expensive for use as a practical design tool.

In order to develop design tools to evaluate the reduction in jet noise attainable with new aircraft shielding configurations, Heaviside's pragmatism might be more appropriate than Laplace's wishful thinking. In this thesis, a new methodology for describing a jet noise source for use in airframe shielding evaluation is presented.

1.1 Motivation

The negative impact on the health and productivity of populations exposed to high noise levels is well documented [9, 68, 46, 36, 35]. The continuing strengthening of regulations on community noise near airports has ensured that the reduction of noise generated by aircraft at take-off and approach remains an essential consideration in the design of new commercial aircraft. In its January 2001 report "European Aeronautics: A Vision for 2020", the Advisory Council for Aeronautics Research in Europe (ACARE)[1] set the goal of a reduction in perceived noise to half of current levels for aircraft entering service from 2020.

While attempting to reach this ambitious target, through aircraft design, noise reduction must be balanced with many other considerations. The two major environmental issues for aircraft – noise and emissions – are not unrelated. In the past, reduction of engine noise was often achieved at the expense of weight and aerodynamic drag, leading to higher fuel consumption. With growing concern about the climate impact of aircraft emissions and rising uncertainty over oil prices, future noise benefits must be secured without compromising fuel burn. This has prompted a review of novel engine installations and airframe configurations, which could possi-

[1] ACARE is a European consortium responsible for establishing and carrying forward a strategic research agenda that will influence all European stakeholders in the planning of research programmes, particularly national and EU programmes, in line with the Vision 2020 and the goals it identifies.

bly be exploited to reduce community exposure to aircraft engine noise. The leading concept is to position the engines above the aircraft so that the fuselage, wings and empennage would act as a noise shield or barrier.

This proposal is currently being investigated in a large number of research projects, including the European FP6[2] funded New Aircraft Concepts Research (NACRE)[3] project and the Silent Aircraft Initiative (SAI). For more information on NACRE and SAI, the reader is referred to [67, 75].

Figure 1.1: European NACRE project's "Pro-Green" configuration with the engines shielded by a U-shaped empennage.

Design evaluation tools must be developed, which can acoustically evaluate such novel shielding configurations within the financial, time and computational constraints of industry.

[2]FP6 is the European Community's Sixth Framework Programme for Research, Technological Development and Demonstration. It is a collection of the actions at EU level to fund and promote research.

[3]The NACRE project has directly funded this present work.

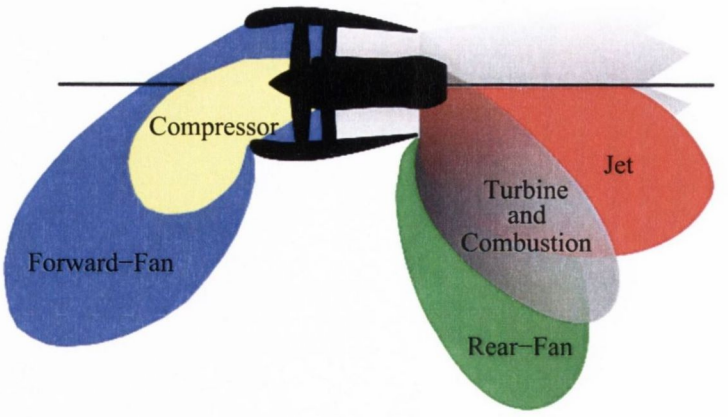

Figure 1.2: Engine noise components for a typical modern turbo-fan engine. The shapes are representative of the relative direction and amplitude of the source components.

Although engine noise is comprised of many component sources, as can be seen in figure 1.2, this thesis only considers the jet noise component, which is a leading engine noise source, particularly at take-off.

The future goal of this work is the development of an acoustic design tool, which can be used in acoustic shielding optimisation. As a constraint for any design tool, it must be at least capable of predicting sound pressure level differences for geometrical variations sufficiently accurately, while being at the same time computationally cheap enough to allow for a large number of computations in an acceptable time frame.

1.2 Jet Noise Shielding

The generation of jet noise, and its propagation and scattering, may be described in principle by the complete compressible Navier-Stokes equations. However, solving these non-linear partial differential equations for the acoustic field, over the large domains in question, will not be practical for the foreseeable future. In order to evaluate the scattering of jet noise by the airframe, it is necessary to make appropriate approximations of these governing equations.

The domain considered in jet noise shielding problems is separated into two regions – inside, and outside the turbulent jet region – and it is assumed that the

sound only radiates outwards from the jet region. This approximation may have implications for cases where the back-scatter is significant. The separation of the domain implies that the jet shielding problem is separated into two steps:

1. Source definition: this represents the complex turbulent jet flow, from an isolated jet, as an acoustic source, and

2. Source propagation: this models the propagation of these sources to the far-field using an appropriate method, which may for example, account for the scattering of the sound by an acoustic shield.

Figure 1.3: Shielding of a point-source by a flat plate. A quiet shadow-zone is visible below the shield.

To acoustically evaluate airframe shielding configurations, the sound pressure level (SPL) from both an *isolated* and an *installed* jet must be evaluated at a far-field receiver. The effectiveness of an acoustic shield is typically quantified in terms of the insertion loss or shielding factor,

$$F_S = 20 \log_{10} \left(\frac{p_{shielded}}{p_{isolated}} \right) = \mathrm{SPL}_{shielded} - \mathrm{SPL}_{isolated}\,, \tag{1.1}$$

where p is the acoustic pressure.

This metric has two advantages. Firstly, it provides an easily understood measure of the benefit of a design at an observer position, which can be provided to regulatory authorities and the general public alike – *"this design will reduce the noise by ten decibels"*. Secondly, it is a relative measure and so uncertainties in the evaluation of the isolated and shielded values will often tend to cancel each other, so long as they are constant between both conditions. For example, estimation of absolute amplitude levels are not necessary for shielding factor prediction. For these reasons, the shielding factor is a popular measure to present a design evaluation result.

1.3 Defining a Jet Noise Source

Aircraft engines produce jet mixing noise as a result of exhaust flow mixing with the external flow downstream of the exhaust nozzle. As the flow emerges from the nozzle exit into the external fluid, a free shear layer originating at the lips of the nozzle forms. This layer separates the fast moving jet from the external fluid, and, at a certain critical Reynolds number, it becomes unstable and breaks down into a turbulent mixing-layer. Small-scale turbulence near the nozzle exit produces high-frequency sound. As the mixing-layer expands and the turbulence grows, the sound produced is of lower frequency. Jet mixing-noise as a whole is broadband.

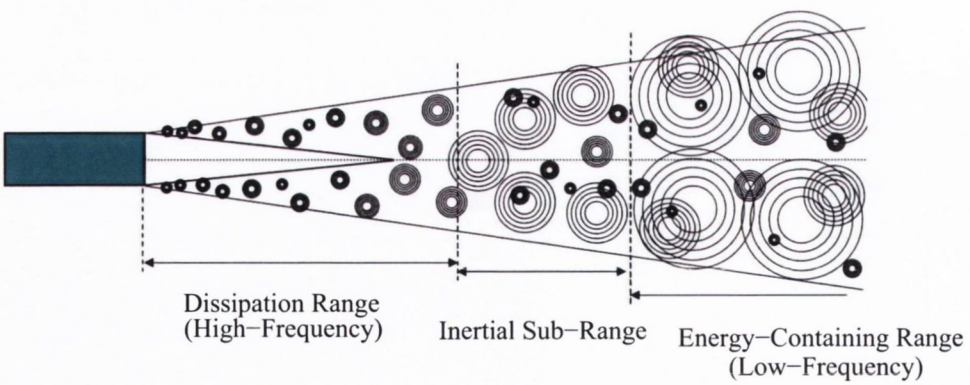

Figure 1.4: Noise-producing regions in a simple jet.

In addition to this mixing noise, jet shock noise can occur when a supersonic flow is not fully expanded to the local ambient pressure. Shock waves are formed in the flow, which generate noise consisting of both shock-cell screech and shock-associated noise. However, this jet noise source is not a significant noise source for commercial aircraft engines, where the flow is typically subsonic. In this present work, only jet mixing-noise is considered and is referred to simply as *jet noise*.

To make predictions of the radiated noise from a turbulent jet flow it is necessary to describe the properties of the turbulence. This is the essence of the jet noise problem. At present, turbulence, and in particular the mechanisms by which it generates noise, are not well understood [51]. A jet mixing-noise source term typically results from some recasting of the governing non-linear fluid dynamics equations into a form that describes linear acoustic propagation, with the source defined as the residual terms [57] or by some heuristic evaluation [81]. This *source* term quite often includes propagation effects.

Although the motion of a turbulent jet flow is described by the Navier-Stokes equations, obtaining the solution for the acoustic variables is a difficult numerical problem. Significant numerical challenges must be overcome as acoustic fluctuations are very small in comparison to the aerodynamic fields. Acoustic fluctuations are so small that they will often fall within machine precision limits. However, recent advances in computational capabilities allow direct numerical simulations (DNS) [61, 40] of the governing equations. These complete solutions provide, and will continue to provide, insights into the subtleties, which comprise the source mechanisms within jets. This could greatly advance our fundamental understanding of jet noise. However, such simulations are computationally very expensive – prohibitively so within a design context.

Large-eddy simulation (LES) [16, 87] is a technique in which the large-scale motions of the flow are calculated, while the effect of the smaller universal scales are modelled using a sub-grid scale model. The filtered Navier-Stokes equations are solved, incorporating an additional sub-grid scale stress term. Although this again is a very promising approach, difficulties must still be overcome. Despite being computationally less demanding than DNS, LES is still significantly more computation-

ally expensive and problematic than solving the Reynolds-averaged Navier-Stokes (RANS) equations with a turbulence model.

At present, practical fluid flow calculations, including jet noise predictions, over large structures are generally based on RANS type simulations. This method provides *averaged* flow-field information, which when used with semi-empirical noise analogy models and calibrated with data, have the capacity to provide reasonable jet noise predictions [8, 81]. Crucially for design evaluation, these predictions are attainable within a short time period and with very modest computational requirements. For the problems at hand – that of modelling the jet flow in order to predict the shielding effect provided by an acoustic shield – a RANS solution is to taken to be the basis for jet noise source definition.

1.4 Propagation of Acoustic Sources

The governing equations are generally reduced considerably, through a series of more restrictive assumptions, before being solved in order to make predictions about the acoustic shielding effect attainable from an airframe. Quite often, the propagation is considered to simply obey the linear wave equation. Once equations with an acceptable level of approximation have been derived to describe the acoustic propagation, there are many numerical methods available to solve such equations. These methods vary greatly, in terms of the accuracy of the solution, the robustness and stability of the method, the computational demand, and the ability to include complex geometries and base-flows.

Discretisation methods break a computational domain into points or elements, and a set of system equations is defined, with boundary conditions to limit the solution. For full-domain methods, such as the finite difference method (FDM), the finite element Method (FEM) or the wave expansion method (WEM), the discretisation is of the full domain and the partial differential equations (PDE) are solved. For boundary element methods (BEM), the PDEs are first converted into reduced-order integral equations using Gauss-Green's theorem. The problem is thus reduced from a volume to an often more economical surface integral. This Boundary Integral

Equation (BIE) formulation relies upon the existence of known Green's functions for the governing equations, which must model the flows within the enclosed volumes.

The highly oscillatory nature of acoustic fields makes numerical computation of high-frequency solutions very challenging. It is known from the Nyquist theory of signal processing analysis that, in order to avoid aliasing effects, the sampling rate must be at least twice that of the highest frequency involved. Thus, a minimum of two points per wavelength will usually be required in numerical discretisation methods. The Helmholtz number is the ratio of the characteristic dimension of the domain to the acoustic wavelength, which is often used to characterise an acoustic propagation problem size. Even for computational domains of modest Helmholtz number, the number of unknowns required to resolve an acoustic solution can be in the millions. For this reason, the BEM, which reduces the dimensionality of a problem, usually has an advantage over full-domain discretisation methods, for the computation of acoustic scattering. On the other hand, full-domain methods are much better equipped to deal with inhomogeneity in the base media.

Figure 1.5: BEM propagation of a monopole located in the forward nacelle onto an airframe geometry.

When the wavelength of the sound is small compared to the characteristic dimension of the scattering body approximate high-frequency methods must be used. The diffraction can be estimated using Fresnel-Kirchhoff diffraction theory, which is based on physical optics. Computation of the diffracted sound may be reduced

to explicit surface integrals, performed over the illuminated face of the scatterer. In the high-frequency limit, wave theory can be replaced by geometrical acoustic theory, in which the sound in considered to behave like rays or beams. Ray-tracing techniques consist of the calculation of the paths of all sound rays between the source and the receiver, and the computation of the sound pressure by summation of the contributions of these sound rays. No diffraction is therefore modelled in pure ray theory.

1.5 Scope of Thesis

In this thesis, analyses was confined to the shielded jet flow examined in the NACRE wind-tunnel test programme, which was a high-Reynold's-number subsonic coaxial flow, with the primary flow heated. A steady-state RANS solution provided mean flow properties for the isolated jet. The turbulent mixing-noise of the jet was the only noise source considered, and this was modelled using an acoustic analogy.

It was assumed that the acoustic shield used in NACRE could be approximated as a flat surface and, therefore, the Fresnel-Kirchhoff shielding prediction method was considered to be sufficiently accurate to assess the shielding factor across a broad range of frequencies. Isolated and shielded predictions were computed, and compared with the NACRE data, and also with predictions computed by NACRE partners using alternative approaches.

It is a prerequisite of this work that modelling methodologies used are low in computational demand and practical within a design evaluation environment. The more specific assumptions, which were made in this work, are discussed as they are introduced in the chapters to follow.

1.6 Structure of Thesis

In chapter 2, a review of acoustic propagation theory is made, and the more relevant of numerical propagation methods are discussed in some more detail. In chapter 3, the present understanding of jet noise theory is reviewed. Lighthill's acoustic analogy

and Tam and Auriault's jet noise model are presented in detail.

In chapter 4, a variation on Lighthill's analogy is introduced, which is to be used to model equivalent jet noise sources for use in shielding predictions. This model attempts to exploit the possible advantages in the form of the Tam and Auriault method. A scheme is presented to reduce the number of sources retained in shielding computations to represent the jet noise. The Fresnel Kirchhoff shielding method is outlined, and a technique to correct the sound propagation for refraction by the mean jet flow is proposed.

In chapter 5, the predictions computed using the modelling methodology from chapter 4 are presented, and comparisons are made with the NACRE isolated and installed data, along with predictions from alternative methodologies. A number trends pertinent to modelling installed jet noise are identified. In chapter 6, a broad discussion of the findings of this present work is made and possible areas for new investigations are suggested. Finally, in chapter 7, the conclusions of this investigative work are stated.

Chapter 2

Acoustic Propagation and Scattering Prediction

The state of a fluid, at time t, can be completely described by specifying the velocity, $\mathbf{u}$, and any two thermodynamic variables, such as the pressure, p, density, ρ, or entropy, S [48]. The evolution of these fields in time is described by the equations of mass continuity, conservation of momentum and conservation of energy. An equation of state is required to close the system. In most circumstances, these governing equations are reduced considerably, through a series of more restrictive assumptions, before a solution is sought. In this chapter, the development of acoustic propagation equations, of interest to the jet noise shielding problem, are reviewed and some of the solution techniques discussed.

2.1 Acoustic Propagation Equations

The full non-linear fluid-dynamic equations for a compressible fluid are

$$\frac{D\rho}{Dt} + \rho\nabla.\mathbf{u} = \rho q\,, \tag{2.1a}$$

$$\rho\frac{D\mathbf{u}}{Dt} = -\nabla p + \nabla.\boldsymbol{\sigma} + \mathbf{f}, \tag{2.1b}$$

$$\rho T\frac{DS}{Dt} = \sigma_{ij}\frac{\partial u_i}{\partial x_j} + K\nabla^2 T\,, \tag{2.1c}$$

where ρ, p, S and $\mathbf{u}$ the absolute density, pressure, entropy and velocity respectively; $D/Dt \equiv \partial/\partial t + \mathbf{u}.\nabla$ is the substantive derivative, q is an external volume flow source, $\nabla.\boldsymbol{\sigma}$ accounts for the viscous forces, $\mathbf{f}$ denotes an externally applied volume force, T is the temperature, and K is the conductivity coefficient. The subscripts i and j denote Einstein's summation notation. It is taken that $p = p(\rho, S)$.

2.1.1 The Linearised Euler Equations

For acoustic computations outside the source region, derivation of acoustic perturbation equations begins by neglecting viscous, external and heat transfer terms, and linearising the equations about the mean flow. Expressing the field variables in terms of mean and fluctuating components (with subscript 0 and primes denoting mean and fluctuating values respectively), and ignoring products of small values, leads to the homogeneous linearised fluid-dynamics equations, referred to as the homogeneous linearised Euler equations (LEE)

$$\frac{D_0\rho'}{Dt} + \rho'\nabla.\mathbf{u}_0 + \mathbf{u}'.\nabla\rho_0 + \rho_0\nabla.\mathbf{u}' = 0\,, \tag{2.2a}$$

$$\frac{D_0\mathbf{u}'}{Dt} + \mathbf{u}'.\nabla\mathbf{u}_0 + \frac{1}{\rho_0}\nabla p' - \frac{\rho'}{\rho_0^2}\nabla p_0 = 0\,, \tag{2.2b}$$

$$\frac{D_0 S'}{Dt} + \mathbf{u}'.\nabla S_0 = 0\,. \tag{2.2c}$$

$D_0/Dt \equiv \partial/\partial t + \mathbf{u}_0.\nabla$ is the substantive derivative with respect to the mean flow. To close the system, for an ideal gas with constant specific heats, c_v and c_p, the pressure fluctuations can be expressed in terms of the density and entropy fluctuations by

$$p' = c_0^2\rho' + \left(\frac{\partial p}{\partial S}\right)_0 S'\,, \tag{2.3}$$

where $c_0 = \sqrt{c_p RT/c_v}$ is the ambient speed of sound, R is the gas constant and T is the absolute temperature.

Equations (2.2) describe the propagation of all small amplitude disturbances in an inviscid flow. This may include vortical and entropy disturbances in addition to acoustic perturbations. A difficulty of the LEE model of acoustic propagation is that the system also supports hydrodynamic instabilities, which can overwhelm the acoustic field in a numerical simulation.

2.1.2 Wave Equations

As $\mathbf{u}'$ is a three-component vector, there are five simultaneous equations in the LEE, which must be solved for the five independent variables. It is desirable, therefore to reduce equations (2.2) to a single partial differential equation (PDE) for a single scalar field quantity – some *potential*, ϕ.

A linearised velocity-potential wave equation for inhomogeneous moving media, may be derived [69], when the ambient flow is considered to be non-rotational and steady, and when the entropy per unit mass has the same value at every point and for all time, as

$$\frac{1}{\rho_0}\nabla.\left(\rho_0\nabla\phi\right) - \frac{D_0}{Dt}\left(\frac{1}{c_0^2}\frac{D_0}{Dt}\phi\right) = 0\,. \tag{2.4}$$

In a potential flow, the acoustic pressure is related to the potential by

$$p' = -\rho_0\frac{D_0}{Dt}\phi\,, \tag{2.5}$$

and the acoustic velocity by

$$\mathbf{u}' = \nabla\phi\,. \tag{2.6}$$

The restriction of an irrotational isentropic mean flow is limiting in practice since most engineering applications involve at least a minor deviation from potential mean flow. In comparison with the five independent variables of the LEEs, equation (2.4) is a second-order PDE, with one unknown. This represents a considerable reduction in the computational resources required when equivalent meshes are used.

At low Mach numbers, the mean flow density and the speed of sound may be assumed to be constant, and equation (2.4) can be reduced to the convected wave equation

$$\nabla^2\phi - \frac{1}{c_0^2}\frac{D_0^2}{Dt^2}\phi = 0\,, \tag{2.7}$$

which has the same form as the ordinary wave equation with a convected time derivative. The assumption of incompressibility is approximately valid when $|\mathbf{u}_0|^2/c_0^2 = M_0^2 \ll 1$, which limits the use of equation (2.7). For homogeneous non-moving ambient media, these wave equations reduce to the (ordinary) wave equation

$$\nabla^2\phi - \frac{1}{c_0^2}\frac{\partial^2}{\partial t^2}\phi = 0\,, \tag{2.8}$$

2.1.3 Frequency Domain Equations

For a harmonic source, the frequency domain equivalents of the LEE or the wave equations may be obtained by replacing the time derivative operator by $i\omega$, where $i = \sqrt{-1}$ and ω is the angular frequency. The frequency-domain equivalent of equation (2.4) is, therefore

$$\frac{1}{\rho_0}\nabla.\left(\rho_0\nabla\phi\right) - L\left(\frac{1}{c_0^2}L\,\phi\right) = 0\,, \tag{2.9}$$

where L is the complex linear operator $(i\omega + \mathbf{u}_0.\nabla)$. In the case of a homogeneous non-moving ambient medium, the frequency domain velocity-potential obeys the Helmholtz equation

$$\nabla^2\phi + k^2\phi = 0\,, \tag{2.10}$$

where $k = \omega/c_0$ is the wave number.

2.2 Numerical Methods

The governing PDEs may only be solved analytically using Green's functions for free propagation through simple flows. The scattering from certain highly-symmetrical geometries in a static ambient flow, may also be determined through separation of variables [18]. These exact solutions rely heavily on the availability of known functions, and their use, for the most part, is limited to the assessment of the accuracy of numerical methods. For most scattering applications of practical interest, it is necessary to use numerical methods to evaluate solutions of the governing field equations.

2.2.1 Discretisation Methods

Finite Difference Method

The finite difference method (FDM) is a full-domain discretisation technique, and is a popular way to model Helmholtz problems [4, 95, 39]. The basic principles of the finite difference method are:

- Discretisation of the domain into a finite number of points uniformly distributed within the domain,
- Approximation of the derivatives of the governing equation by interpolating polynomials, formulated in terms of surrounding points in the grid, and
- Solution of a system of equations of the form $\mathbf{Ax} = \mathbf{b}$, where, for the FDM, $\mathbf{A}$ is the banded coefficient matrix, $\mathbf{b}$ is the forcing vector determined by the boundary conditions and loadings applied on the physical domain, and $\mathbf{x}$ is the approximated field variable at each discretisation point.

Finite Element Method

The finite element method (FEM) is probably the most widely used method in the numerical modelling of problems of general engineering interest due to its adaptability and straightforward implementation [95, 39]. Like the FDM, the full domain is discretised in the FEM. The method is based on the following concepts:

- Transformation of the original differential problem to its respective integral formulation (weighted residual or variational),
- Division of the continuum into small non-overlapping sub-domains called elements, over which the system integral equations may be summed,
- Approximation of the field variable distributions and the geometry of the continuum domain, in terms of a set of shape functions, which are locally defined in each element, and
- Solution of a system of equations of the form $\mathbf{Ax} = \mathbf{b}$, where, in this case, $\mathbf{A}$ is a sparse coefficient matrix.

In most applications the finite element method is used with the Galerkin formulation for the weighted residuals.

Boundary Element Method

The boundary element method (BEM) has become one of the most prominent methods in the numerical analysis of the Helmholtz equation [19, 17, 93, 92]. This numerical method for field problems is based on boundary integral equations. The problem's dimensionality is reduced by one, so that three-dimensional domains are reduced to a two-dimensional surface integral. There are two main approaches in obtaining a boundary integral equation formulation for acoustic problems – the so-called *direct* and *indirect* methods. For the direct or indirect formulation, the boundary element solution is obtained by the following procedure:

- The field equations are transformed to a boundary integral using divergence theorem,
- The boundary is discretised, and discrete integral equations are formed using loading points situated on the boundary, leading to a system of equations,
- When these equations are restrained, a system of equations of the form $\mathbf{Ax} = \mathbf{b}$, is solved, where $\mathbf{A}$ is a full coefficient matrix in the BEM, and $\mathbf{x}$ is the distribution of boundary values, and
- The field variable at any point in the domain may be obtained by integrating the product of boundary values and the fundamental solution over the boundary.

The main advantage of full-domain discretisation methods, like the FDM or FEM, over BEM is that inhomogeneities in the propagation medium can be easily introduced into the models. BEMs are reliant on valid Green's functions within the enclosed volume for propagation. Although many useful acoustic predictions can be achieved using wave/Helmholtz equation type formulations, some recent advances in aeroacoustic computations have focused on the LEE [63] and the full Euler equations [78, 84], which for example, use a time-domain discontinuous Galerkin method, that may allow acoustic modelling with complex background flows.

On the other hand, the FDM and FEM may require prohibitive computational resources for large domains. The BEM requires discretisation of the surface instead of the full domain. This results in a considerable reduction of the computational modelling requirements, especially in the case of acoustic applications for aircraft. However, this advantage is somewhat offset by the full structure of the system matrix, which means that a full-domain method in three-dimensions may be still be more computationally efficient, if certain solving strategies are applied.

Despite the fact that these discretisation methods have been widely used for many years, their efficiency is limited to lower frequencies. At higher frequencies, the computational cost required to obtain an accurate solution rapidly consumes available computational resources. Many alternative numerical techniques have been developed over the past number of years, which attempt to address some of the problematic issues associated with the traditional methods. The computational cost is closely related with the number of points per wavelength needed to accurately discretise each dimension of the domain under consideration. Existing FDM and FEM methods using polynomial interpolations require a mesh spacing of about six to ten points per wavelength to obtain acceptable accuracy in the solution of the Helmholtz equation [23].

Wave Expansion Method

In order to alleviate some of these limitations, associated with traditional methods, new physically based methods, such as the wave expansion method (WEM), were developed [23, 24, 74]. The WEM solves the inhomogeneous moving-media Helmholtz equation by full-domain discretisation, relating the value of the unknown at each discrete point of the domain to the values at a selected set of neighbouring points. The WEM represents a local interpolation formula to obtain the field values in the domain. The procedure to obtain a wave expansion method solution is

- Discretisation of the domain into a finite number of points distributed within the domain,
- Formulate the relationship between a point and its surrounding points in the

grid using the summation of hypothetical plane waves, and

- Solve of a system of equations of the form $\mathbf{Ax} = \mathbf{b}$, where $\mathbf{A}$ is a sparse coefficient matrix and $\mathbf{x}$ is the field variable at each discrete point.

For more information on this methods the reader is directed to Appendix A.

This discretisation methods offers an enormous improvement in computational efficiency, by reducing the number of points per wavelength required to obtain accurate solutions to as low as two to three, and the sparse system matrix, has a high bandwidth especially in three-dimensional problems. This discretisation is perhaps optimal, as it valid down to the Nyquist limit of two points per wavelength.

2.2.2 High-Frequency Methods

Ray tracing

Ray tracing techniques are based on geometrical acoustics, where the sound is considered to act like rays [94, 76]. This assumption is valid when the wavelength of the propagated sound is small compared to the dimensions of the scattering surface, and large compared to the roughness of the surface. The method has been extensively used for scattering problems in computational electromagnetics and for rendering 3D images with lighting effects in computer graphics. For these type of applications the external media can always be treated as uniform, and so much of the development of ray tracing has focused on this case. For aeroacoustic scattering problems this is not always the case.

Ray model techniques consist of the calculation of the paths of all sound rays between the source and the receiver, and the computation of the sound pressure by summation of the contributions of these sound rays. There are several variations of the algorithm. In the basic algorithm the sound source emits sound rays, which are then reflected at surfaces according to their specular reflection and the sound pressure at the receiver is computed as an incoherent sum of the rays that intersect at the receiver. The receivers are typically spheres of finite radius, and the detection mechanism makes it possible to compute the sound energy density inside the receiver volume.

Classical ray tracing algorithms are not well suited to the addition of diffraction theory, in particular, smooth surface diffraction effects are difficult to implement with non-smooth geometry. Ray tracing methods may also fail to find all significant propagation paths containing diffraction. The receiver position and diffracting edges are often approximated by volumes of space, which can lead to false hits and paths counted multiple times. Moreover, important propagation paths may be missed by all samples. In order to minimise the likelihood of large errors, ray tracing systems often generate a large number of samples, which requires a large amount of computational resources. Advantage may be taken of parallel computing systems in these cases.

Fresnel-Kirchhoff Diffraction Techniques

The Fresnel-Kirchhoff diffraction method (FKM) is an approximate method for the determination of the field scattered by an object, through an assumption about the specific form of the field distribution on the surface. It is based on *physical*[1] optics. In contrast to geometrical acoustics, the scattering is frequency dependent and it, therefore, provides a more accurate estimate of the scattering [18].

To predict the scattering effect from a flat plate using the FKM, the geometric complement of the problem [13] is considered – that is, an acoustic source separated from a receiver by a slot in an infinitely long rigid plate. The acoustic pressure at the receiver may then be obtained using the Helmholtz-Kirchhoff integral equation. Assuming that the acoustic field on the shielded side of the infinitely long plate is zero, and that the field in the aperture is the same as it would be in a completely free field, the integral surface reduces to the area of the slot. Babinet's principle, that complementary diffracting objects have complementary diffraction patterns, reverts back to the original shielding problem of interest.

The assumptions involved place significant limitations on the geometries, which the FKM may be applied to. These assumptions are also better approximated at higher frequencies. Although the accuracy of predictions reduces at lower frequen-

[1] Physical denotes that it is more physical than geometrical optics and not that it is an exact physical theory

cies, the method does not fail completely. The method is also dependent on knowing Green's functions for the integral equation and so its application is, in general, limited to homogeneous non-rotating propagation media. Promising calculations have also been reported recently, which attempt to include curved scattering surfaces, such as those of an aircraft fuselage [62].

2.3 Discussion

In this present work, the propagation field was considered to be homogeneous and non-moving. As both the location of jet noise sources and the effectiveness of acoustic shields are highly dependent on frequency, the analyses was conducted in the frequency domain. The governing field equation was, therefore, the Helmholtz equation. This selection is very much in keeping with traditional acoustic analogies for modelling jet noise, as is shown chapter 3.

The NACRE tests examined were performed with a (nominally) stationary medium beyond the jet, and so, this assumption is appropriate for the majority of the acoustic propagation domain under consideration. This choice also facilitates the selection of the FKM to predict the shielding effect, and so limits required computational demand.

In chapter 4, however, it is proposed that the effect of the mean jet flow on sound propagation through the jet, may be accounted for by solving equation (2.9) for an irrotational inhomogeneous moving media within the vicinity of the jet, using the WEM. This exception is employed in order to provide a correction factor to the source directivity, and so to enable an assessment of the effect of flow refraction on shielding predictions.

Chapter 3

Jet Noise Modelling

At present, jet noise predictions for industrial design purposes are frequently based on Reynold's-averaged Navier-Stokes (RANS) solutions with statistical models of space-time correlation functions. In this chapter, a review of jet noise theories is presented. The two most relevant jet noise models to this study – Lighthill's acoustic analogy, and Tam and Auriault's model – are then examined in detail.

3.1 Review of Jet Noise Theory and Modelling

Early Acoustic Analogies

Lighthill's two-part paper [57, 58] in 1952 and 1954 established the acoustic analogy theory, and is regarded as marking not only the beginning of jet noise research but also the birth of aeroacoustics. Lighthill recast the full compressible Navier-Stokes equations in the form of an inhomogeneous acoustic wave equation with all non-linearities included on the right-hand-side and, thus, considered to be an acoustic *source* term. Lighthill's source takes the form of a double-divergence, and therefore, the source is considered to be quadrupole in nature. In Lighthill's theory, the jet is interpreted as being comprised of acoustically compact, or small-scale, random sound-producing turbulent fluctuations, which are correlated over a limited space-time area. As these acoustic sources are thought to be convected downstream, the radiated sound field is stronger in the downstream direction, and there is a

Doppler shift in the frequency [34]. Lighthill's equation shows that there is an *exact analogy* between the density fluctuations that occur in any real flow and the small amplitude density fluctuations that would result from a convecting quadrupole source distribution in a fictitious non-moving acoustic medium.

The appeal of Lighthill's equation is that it is relatively easy to solve for the linear response of the base-flow using a Green's function solution, assuming that the source term is known. However, a full description of Lighthill's source is equivalent to solving the full non-linear governing equations. Despite this, the broadband effect of the source can be estimated using a combination of statistical modelling and a RANS solution.

As all the non-linearities are included on the right-hand-side of Lighthill's equation, all acoustic-flow interaction terms are also hidden in this *source* term, including the refraction of the sound away from the jet axis. Lilley [60] attempted in 1974 to separate these acoustic-flow interactions from the source term, as he derived a third-order wave equation, which described compact convecting sources, whose sound fields are modified by the sheared mean-flow. Lilley's analogy does remove some of the sound production redundancy from the source terms, but not all of it [51]. On the other hand, it may be more difficult to solve Lilley's third-order partial differential equation than Lighthill's equation.

This comparison between Lighthill's and Lilley's analogies defines an acoustic analogy as an implicit linearisation of the governing equations about some base-flow, with the remaining terms being considered as external noise source. It typifies the trade-off that takes place in defining an acoustic analogy, as the simpler the base-flow, the greater the complexity of the source term, if the equations are to remain exact [51]. It also raises the philosophical question as to what exactly constitutes a source mechanism in a free jet, a question that is at the heart of modern aeroacoustic research. Indeed, it can still be said that there is no clear understanding of the physics of noise generation in free turbulent flows.

Other acoustic analogies, such as those by Powell [70], Howe [47], and Möhring [64], formulated the source term in terms of the vorticity of the flow. The appeal of these analogies is that it is more intuitive that sound is produced in a turbulent

flow by vorticity than by the double-divergence of a second-order stress tensor, as in Lighthill's analogy.

Large-Scale Structures

In the 1970s, Crow and Champagne [29]; Lau *et alia* [55]; Fuchs [41]; Brown and Roshko [20], and others identified, the existence of large-scale coherent flow structures, which generate noise in jet flows, and dominate the sound field in downstream directions. While there is no real consensus as to the precise mechanisms, which underlie this source component, some popular candidates for single stream jets include vortex pairing [56], wavy-wall-type mechanisms [91, 28, 26], and vortex eigenoscillations [54].

These structures can be considered to introduce a type of large-scale deterministic source mechanism, in addition to the earlier small-scale random mechanism. The jet region between the nozzle exit and the end of the potential core has been shown to be characterised by such coherent structures. Their violent collapse at the end of the potential core may also constitute an additional source mechanism [52].

Tam *et alia* [82] investigated the possibility that two source mechanisms existed for supersonic jets – one, a low frequency component generated in the downstream direction by large-scale structures; the other, a high-frequency component radiated by the small-scale turbulent structures of the flow, with a relatively uniform directivity, that dominates in the sideline and the upstream directions. Tam [79] proposed two similarity spectra related to each mechanism. Viswanathan [88] showed that these similarity components also agree well with data for subsonic jets. However, the underlying physics of this two-mechanism hypothesis remains unclear and it is noted [44, 51] that it may not correspond to any physical flow structure.

In the region immediately downstream of the nozzle exit, sound production may be more efficient due to the presence of the nozzle itself, as identified experimentally by Tinney *et alia* [86] and numerically by Viswanathan *et alia* [89]. As this strong source is not evident when the nozzle is not included, as in Bogey and Bailly's [15] work, it can be inferred that a source mechanism is related to the presence of the nozzle. Although whether this is strictly a jet noise source, or not, is a matter

of opinion.

It should be noted that the characteristics of these large-scale source mechanisms precludes the use of steady-state RANS computations to characterise them.

Recent Jet Noise Models

Tam and Auriault [81] introduced a model in 1999, through a heuristic argument, on an analogy between the molecular pressure from the kinetic theory of gases and the turbulent pressure from packets of small-scale turbulence. The sources are explicitly modelled and their propagation is described by the linearised Euler equations. As with predictions based on Lighthill's analogy, statistical modelling of the turbulence is required, and a RANS solution of jet is often used to provide averaged flow properties. Although this model initially appeared to be a break from earlier acoustic analogies, Morris and Farassat [65] showed that if consistent assumptions are made concerning the statistical modelling, both approaches can yield identical results.

Tam and Auriault also proposed [81] the use of three empirical parameters in their model, which are evaluated by a best-fit of experimental data, to supposedly exclude the contribution from the large-scale turbulent structures to the RANS solution. In a comparison between this model and various acoustic analogies, Afsar *et alia* [1] found the Tam-Auriault model to be sensitive to slight changes in the mean flow profile.

Béchara *et alia* [7], and Bailly and Juvé [5] proposed a Stochastic Noise Generation and Radiation (SNGR) jet noise prediction method in 1990s. An unsteady velocity field is generated by stochastic simulation with a collection of discrete random Fourier modes, with the same local statistical properties as the RANS solution of the flow. This turbulent field is used as a source term in Euler's equations, linearised about the mean jet flow from the RANS solution. Despite recent work to improve the physics of the synthetic turbulence [12], SNGR does not appear to have yielded any improvement to date, over Lighthill's analogy-based models, of far-field SPL predictions of jet noise, despite the additional computational costs required [5, 10, 11].

In a variation on SNGR, Ewert [37] incorporates synthetic turbulence in a

Random Particle-Mesh (RPM) method. In this method, fluctuating quantities are generated by spatially filtering convective white noise, with a shape function. These quantities are used in a time-domain realisation of the Tam-Auriault jet noise source. This method is seen as an algorithmic extension of traditional statistical broadband methods. It is too early to draw any conclusions on this approach, as quantitative results are not available as yet.

Summary

As a RANS solution is to provide information on flow properties, for this present work, the presence of large-scale jet noise structures is ignored. It is assumed that this approximation has a small impact on acoustic predictions at angles away from the jet axis, which are of interest here. As such, only the small-scale jet noise structures are considered.

In the following sections, Lighthill's acoustic analogy is presented in depth, as it forms the core of modern jet noise models. The Tam-Auriault method is also presented, as it is popularly used as a jet noise model, and as the method has shown good agreement with a large set of data [81], it may provide some insight into jet noise modelling in a broader sense.

3.2 Lighthill's Acoustic Analogy

Lighthill recast the exact equations of motion (equations (2.1)) as

$$\frac{\partial^2 \rho'}{\partial t^2} - c_0^2 \nabla^2 \rho' = \frac{\partial^2 T_{ij}}{\partial x_i \partial x_j}\,, \tag{3.1}$$

where ρ' is the acoustic density fluctuation and c_0 is the ambient speed of sound. T_{ij} is Lighthill's stress tensor

$$T_{ij} = \rho u_i u_j + \left[(p - p_0) - c_0^2 (\rho - \rho_0)\right] \delta_{ij} + \sigma_{ij}\,, \tag{3.2}$$

where p and ρ are the absolute local pressure and density, p_0 and ρ_0 are the ambient pressure and density, δ_{ij} is a Kronecker delta function, σ_{ij} is a viscous stress tensor, and the subscripts i and j denote Einstein's summation notation. For a high-

Reynolds-number flow the source term T_{ij} can be approximated by the Reynold's stress as $T_{ij} = \overline{\rho} u_i u_j$, where $\overline{\rho}$ is the local mean density.

3.2.1 Solving Lighthill's Equation

Lighthill's equation has the same form as the wave equation that governs the acoustic field from a quadrupole source in a stationary medium. If any solid boundaries, which may be present, do not appreciably influence the sound field, the solution can be expressed using a time-dependent free-space Green's function, G. The density fluctuations at a receiver point located at $\mathbf{x}$, from a compact turbulent source volume distribution located at $\mathbf{x_s}$, are

$$\rho'(\mathbf{x}, t) = \frac{1}{c_0^2} \int \int_{-\infty}^{\infty} \mathrm{G}(\mathbf{x}, \mathbf{x_s}, t, t_s) \frac{\partial^2 T_{ij}}{\partial x_{si} \partial x_{sj}} (\mathbf{x_s}, t_s) \, dt_s \, d\mathbf{x_s} , \tag{3.3}$$

where t and t_s are the receiver and sources times. The analyses often proceeds with the evaluation of the time integral, which exploits the sifting property of an impulse function[1], followed by the changing of the spatial derivatives to a time derivative using multipole expansion, which assumes that the source and receiver are many wavelengths apart [43]. This leads to

$$\rho'(\mathbf{x}, t) = \frac{1}{4\pi c_0^4} \frac{r_i r_j}{r^3} \int \frac{\partial^2}{\partial t^2} T_{ij} \left(\mathbf{x_s}, t - \frac{|\mathbf{x} - \mathbf{x_s}|}{c_0} \right) d\mathbf{x_s} , \tag{3.4}$$

where $\mathbf{r}$ is the vector separating $\mathbf{x}$ and $\mathbf{x_s}$, and $r = |\mathbf{x} - \mathbf{x_s}|$. The volume integral is over the source volume V.

The far-field spectral density is related to the Fourier transform of the auto-correlation function of the far-field density as

$$S(\mathbf{x}, \omega) = \frac{c_0^4}{2\pi} \int_{-\infty}^{\infty} \exp(i\omega\tau) \left\langle \rho'(\mathbf{x}, t) \, \rho'(\mathbf{x}, t + \tau) \right\rangle d\tau , \tag{3.5}$$

where $\langle \rangle$ denotes an ensemble average. It therefore follows that

$$\begin{aligned} S(\mathbf{x}, \omega) = & \frac{1}{32\pi^3 c_0^4} \frac{r_i r_j r_k r_l}{r^6} \int \int \int \exp(i\omega\tau) \\ & \times \left\langle \frac{\partial^2}{\partial t^2} T_{ij}(\mathbf{x_1}, t_1) \frac{\partial^2}{\partial t^2} T_{kl}(\mathbf{x_2}, t_2 + \tau) \right\rangle d\tau \, d\mathbf{x_1} \, d\mathbf{x_2} , \end{aligned} \tag{3.6}$$

[1] $\int \delta(t_s - t + |\mathbf{x} - \mathbf{x_s}|/c_0) \, \mathrm{f}(t_s) \, dt_s = \mathrm{f}(t - |\mathbf{x} - \mathbf{x_s}|/c_0)$

where $\mathbf{x_1}$ and $\mathbf{x_2}$ are two points in the source region, $t_1 = t - |\mathbf{x} - \mathbf{x_1}|/c_0$ and $t_2 = t - |\mathbf{x} - \mathbf{x_2}|/c_0$. The cross-correlation tensor in this equation may be rewritten as

$$\left\langle \frac{\partial^2}{\partial t^2} T_{ij}\left(\mathbf{x_1}, t_1\right) \frac{\partial^2}{\partial t^2} T_{kl}\left(\mathbf{x_2}, t_2 + \tau\right) \right\rangle = \frac{\partial^4}{\partial \tau^4} \left\langle T_{ij}\left(\mathbf{x_1}, t\right) T_{kl}\left(\mathbf{x_2}, t + \tau + \frac{\boldsymbol{\eta}.\mathbf{r}}{c_0 r}\right) \right\rangle , \tag{3.7}$$

where $\boldsymbol{\eta} = \mathbf{x_2} - \mathbf{x_1}$ is a separation vector.

Inserting equation (3.7) back into equation (3.6) and changing the variable of integration, the spectral density may be rewritten as[2]

$$S\left(\mathbf{x}, \omega\right) = \frac{\omega^4}{32\pi^3 c_0^4} \frac{r_i r_j r_k r_l}{r^6} \int\int\int \exp\left(i\omega\left(\tau - \frac{\boldsymbol{\eta}.\mathbf{r}}{c_0 r}\right)\right) \boldsymbol{R}_{ijkl}\left(\mathbf{x_1}, \boldsymbol{\eta}, \tau\right) \, d\tau \, d\boldsymbol{\eta} \, d\mathbf{x_1} , \tag{3.8}$$

with

$$\boldsymbol{R}_{ijkl}\left(\mathbf{x_1}, \boldsymbol{\eta}, \tau\right) = \left\langle T_{ij}\left(\mathbf{x_1}, t\right) T_{kl}\left(\mathbf{x_2}, t + \tau\right) \right\rangle . \tag{3.9}$$

$\boldsymbol{R}_{ijkl}$ is a fourth-order two-point time-delayed correlation tensor.

The correlation tensor in equation (3.8) is measured in a fixed-frame of reference. In order to evaluate the intensity spectrum using this equation it is useful to introduce a moving-axis transformation into the separation vector. Introducing $\boldsymbol{\xi} = \boldsymbol{\eta} - \hat{\mathbf{i}}\, c_0 M_c \tau$ into equation (3.8) gives

$$S\left(\mathbf{x}, \omega\right) = \frac{\omega^4}{32\pi^3 c_0^4} \frac{r_i r_j r_k r_l}{r^6} \int\int\int \exp\left(i\omega\left(C\tau - \frac{\boldsymbol{\xi}.\mathbf{r}}{c_0 r}\right)\right) \mathbf{R}_{ijkl}\left(\mathbf{x_1}, \boldsymbol{\xi}, \tau\right) \, d\tau \, d\boldsymbol{\xi} \, d\mathbf{x_1} , \tag{3.10}$$

where $\hat{\mathbf{i}}$ is a unit vector in the mean flow direction, M_c is the convective Mach number of the source, $C = 1 - M_c \cos\theta$ is a convection (or Doppler) factor, $\cos\theta = r_1/r$ and r_1 is the component of $\mathbf{r}$ aligned with the mean jet flow direction. This optional moving-axis transformation essentially decouples the convection of the noise-generating turbulent eddies from the correlation tensor, and may leave it easier to model. If this transformation is not included, source convection must be modelled within the correlation tensor. $\mathbf{R}_{ijkl}$ is a fourth-order two-point time-delayed moving-axis correlation tensor and $\mathbf{R}_{ijkl}\left(\mathbf{x_1}, \boldsymbol{\xi}, \tau\right) = \boldsymbol{R}_{ijkl}\left(\mathbf{x_1}, \boldsymbol{\eta}, \tau\right)$.

[2]It should be noted that the Fourier transform of the time derivative of function f is $F\left[\partial^n f/\partial^n \tau\right] = (-i\omega)^n F\left[f\right]$, where n is the order of the derivative.

3.2.2 Modelling the Correlation Tensor

In order to evaluate the spectral density, it is necessary to measure or deduce analytically $\mathbf{R}_{ijkl}(\mathbf{x_1}, \boldsymbol{\xi}, \tau)$. This remains a difficult problem, though a number of approximate models have been developed over the past 50 years. Lighthill himself used dimensional analysis of a simple jet, and famously established that the acoustic power radiated by a jet should vary with the eight-power of the jet velocity.

The turbulence velocity vector is normally separated into mean and fluctuating parts. If the mean flow is approximated as parallel to the jet axis [59, 73]

$$u_i(\mathbf{x}, t) = \overline{u}_i(\mathbf{x})\,\delta_{1i} + u'_i(\mathbf{x}, t)\ , \tag{3.11}$$

where $\overline{u}_i$ is the time-averaged velocity and u'_i is the fluctuating velocity, thus the correlation tensor may be expressed as

$$\begin{aligned}\mathbf{R}_{ijkl}(\mathbf{x_1}, \boldsymbol{\xi}, \tau) =& \overline{\rho}^2 \left(\overline{u'_{1i} u'_{1j} u'_{2k} u'_{2l}} + \overline{u}_{11}\overline{u}_{21} \left(\delta_{1i}\delta_{1k}\overline{u'_{1j}u'_{2l}} \right.\right. \\ &\left.\left. + \delta_{1j}\delta_{1l}\overline{u'_{1i}u'_{2k}} + \delta_{1j}\delta_{1k}\overline{u'_{1i}u'_{2l}} + \delta_{1i}\delta_{1l}\overline{u'_{1j}u'_{2k}} \right) \right)\ ,\end{aligned} \tag{3.12}$$

where u_{1i} denotes $u_i(\mathbf{x_1})$. The first term in equation (3.12) involves only turbulence self-interactions, whereas the rest of the terms involve interaction between the mean-shear-flow and the turbulence. Lilley [59] introduced the terminology self-noise and shear-noise to indicate noise generated by turbulence-turbulence interactions and noise generated by turbulence-mean-shear interactions.

Ribner's work [73, 72] is the principle basis for many statistical jet noise models. With an assumption that the joint probability of u'_{1i} and u'_{2i} is normal, the fourth-order self-noise correlation term in equation (3.12) can be written in terms of second-order tensors as

$$\overline{\rho}^2\, \overline{u'_{1i} u'_{1j} u'_{2k} u'_{2l}}\,(\mathbf{x_1}, \boldsymbol{\xi}, \tau) = \mathbf{R}_{ik}\mathbf{R}_{jl}(\mathbf{x_1}, \boldsymbol{\xi}, \tau) + \mathbf{R}_{il}\mathbf{R}_{jk}(\mathbf{x_1}, \boldsymbol{\xi}, \tau)\ , \tag{3.13}$$

where $\mathbf{R}_{ij}(\mathbf{x_1}, \boldsymbol{\xi}, \tau) = \overline{\rho}\,\overline{u'_{1i}u'_{2j}}\,(\mathbf{x_1}, \boldsymbol{\xi}, \tau)$. Ribner also assumes that these space-time correlation functions may further be separated into independent functions of space and time and so

$$\mathbf{R}_{ij}(\mathbf{x_1}, \boldsymbol{\xi}, \tau) = \mathbf{R}_{ij}(\mathbf{x_1}, \boldsymbol{\xi})\, g(\mathbf{x_1}, \tau)\ . \tag{3.14}$$

Homogeneous Isotropic Spatial Model

Ribner considered the turbulence to be homogeneous and isotropic and, therefore, a single velocity correlation describes its spatial decay, a single time-scale describes its temporal decay, and a single value of the turbulent kinetic energy to represent the kinetic energy of the flow. These values are also considered to be independent of frequency. For homogeneous isotropic turbulence, where $\mathbf{x_s} = (\mathbf{x_1} + \mathbf{x_2})/2$, the spatial correlation function may be defined as [73]

$$\mathbf{R}_{ij}(\mathbf{x_s}, \boldsymbol{\xi}) = \overline{\rho}\,\overline{u_t^2}\left[\left(f + \frac{\xi}{2}\frac{\partial f}{\partial \xi}\right)\delta_{ij} - \frac{1}{2}\frac{\partial f}{\partial \xi}\frac{\xi_i \xi_j}{\xi}\right] \tag{3.15}$$

where $\overline{u_t^2}$ is the turbulent kinetic energy and f is the longitudinal correlation coefficient function. f is some universal function of ξ, which is generally assumed to be

$$f(\xi) = \exp\left(\frac{-\pi\xi^2}{l_t^2}\right). \tag{3.16}$$

where l_t is the integral length-scale of the turbulence.

Alternatively, as Devenport *et alia* [33] showed, the homogeneous isotropic spatial correlation function in an incompressible flow can be expressed as the double curl of the vector-potential correlation

$$\mathbf{R}_{ij}(\mathbf{x_s}, \boldsymbol{\xi}) = \varepsilon_{ikl}\varepsilon_{jmn}\frac{\partial^2 q_{ln}}{\partial \xi_m \partial \xi_k}, \tag{3.17}$$

where ε_{jlm} is the Levi-Civita or permutation tensor. For homogeneous turbulence the vector-potential correlation is given by

$$q_{ij}(\mathbf{x_s}, \boldsymbol{\xi}) = -\overline{\rho}\,\frac{\overline{u_t^2}}{2} h(\xi)\,\delta_{ij}, \tag{3.18}$$

and $h(\xi)$ is the first moment of longitudinal correlation coefficient function

$$h(\xi) = \int_0^{\xi} \xi' f(\xi')\, d\xi'. \tag{3.19}$$

Isotropic Temporal Model

The temporal correlation function in this homogeneous isotropic case is usually taken to be either of the form

$$g(\mathbf{x_s}, \tau) = \exp\left(-\pi\frac{|\tau|}{\tau_t}\right), \tag{3.20}$$

or

$$g\left(\mathbf{x_s}, \tau\right) = \exp\left(-\pi \frac{\tau^2}{\tau_t^2}\right), \tag{3.21}$$

where τ_t is the integral time-scale of the turbulence.

Spatial Correlation Function

The mean-flow two-point correlation function $\overline{u}_1\left(\mathbf{x_1}\right)\overline{u}_1\left(\mathbf{x_2}\right)$, which is required for the shear-noise terms, was modelled by Ribner as the Gaussian expression $\overline{u}_{11}\overline{u}_{12} = \overline{u}_1^2\left(\mathbf{x_s}\right)\exp\left(-\sigma\pi\xi_2^2/l_t^2\right)$, where σ is a local coefficient. This expression is not well adapted to real modelling situations as σ is not a constant [8]. To avoid modelling σ, a better approach is to perform a Taylor expansion to the first order of $\overline{u}_1\left(\mathbf{y_1}\right)\overline{u}_1\left(\mathbf{y_2}\right)$ around the midpoint $\mathbf{y}$ such that

$$\overline{u}_1\left(\mathbf{x_1}\right)\overline{u}_1\left(\mathbf{x_2}\right) = \overline{u}_1^{\,2}\left(\mathbf{x_s}\right) - \frac{\xi_2^2}{4}\left(\frac{\partial}{\partial x_{\mathrm{s}2}}\overline{u}_1\left(\mathbf{x_s}\right)\right)^2. \tag{3.22}$$

The mean axial velocity, $\overline{u}_{\mathrm{s}1}$, and its radial gradient, $\partial\overline{u}_{\mathrm{s}1}/\partial x_{\mathrm{s}2}$, may be taken from a RANS solution.

Inhomogeneous Anisotropic Spatial Model

Realistic jet turbulence is neither homogeneous nor isotropic. The inhomogeneity manifests in the Reynold's stress field, with the ratio between the axial component and the radial and lateral components varying over the jet. Additionally, anisotropy is to be found in the length and time scales due to the mean flow. Davies *et alia* [30] note that large-scale eddies become mainly cylindrical structures with a longitudinal scale approximately three times the transverse scale.

Goldstein and Rosenbaum [45] argued that it is more appropriate to assume the turbulence is axisymmetric rather than isotropic and, as such, the space-time correlation can be expressed in terms of two independent scalar functions, therefore

$$\mathbf{R}_{ij}\left(\mathbf{x_s}, \boldsymbol{\xi}, \tau\right) = \epsilon_{jlm}\frac{\partial q_{im}}{\partial \xi_l}, \tag{3.23}$$

where q_{im} is the skew tensor

$$q_{im} = \xi_k\left[\epsilon_{imk}Q_1 + \epsilon_{i1k}\left(\delta_{1m}Q_2 + \xi_m Q_3\right)\right]. \tag{3.24}$$

Kinematically acceptable models for Q_1 and Q_2 are [8, 53]

$$Q_1(\mathbf{x_s}, \boldsymbol{\xi}, \tau) = -\frac{1}{2}\overline{\rho}\,\overline{u_{t1}^2}\, g(\mathbf{x_s}, \tau) \exp\left[-\left(\frac{\xi_2^2 + \xi_3^2}{l_{t2}^2} + \frac{\xi_1^2}{l_{t1}^2}\right)^{1/2}\right], \tag{3.25}$$

and

$$Q_2(\mathbf{x_s}, \boldsymbol{\xi}, \tau) = -\overline{\rho}\left(\overline{u_{t2}^2} - \overline{u_{t1}^2}\right) g(\mathbf{x_s}, \tau) \exp\left[-\left(\frac{\xi_2^2 + \xi_3^2}{l_{t2}^2} + \frac{\xi_1^2}{l_{t1}^2}\right)^{1/2}\right], \tag{3.26}$$

with

$$Q_3 = \left(\frac{\partial}{\partial \xi_1} - \frac{\xi_1}{\xi_3}\frac{\partial}{\partial \xi_3}\right) Q_1, \tag{3.27}$$

where l_{t1} and l_{t2} are the longitudinal and transverse length-scales; and $\overline{u_{t1}^2}$ and $\overline{u_{t2}^2}$ are the longitudinal and transverse turbulent kinetic energy For axisymmetric turbulence

$$\mathbf{x_s} = \left(x_{11}, \frac{x_{12} + x_{22}}{2}, \frac{x_{13} + x_{23}}{2}\right), \tag{3.28}$$

as opposed to the mid-point of $\mathbf{x_1}$ and $\mathbf{x_2}$ used in the isotropic models.

Jordan and Gervais [50] describe a modification of the vector-potential correlation to model the inhomogeneity of a jet flow. The turbulent kinetic energy is replaced by a scaling function, a_{ij}, in equation (3.18), giving

$$q_{ij}(\mathbf{x_s}, \boldsymbol{\xi}) = a_{ij}(\mathbf{x_s}, \boldsymbol{\xi})\, h(\xi)\, \delta_{ij}. \tag{3.29}$$

Jordan and Gervais modelled a_{ij} with an analytical expression to describe the structure of the Reynold's stress field for a simple jet. An analytical expression is not practical for coaxial jet flows of interest. They also note that the assumption of normal joint probability, used in equation (3.13) to rewrite the fourth-order self-noise tensor as second-order tensor, imposes homogeneity.

To account for anisotropy in the turbulence, Jordan and Gervais introduced a anisotropic longitudinal correlation coefficient function

$$f(\xi) = \exp\left(-\pi\left(\frac{\xi_1^2}{l_{t1}^2} + \frac{\xi_2^2}{l_{t2}^2} + \frac{\xi_3^2}{l_{t3}^2}\right)\right). \tag{3.30}$$

The spatial decay of the longitudinal velocity correlation function is thus described by an ellipsoid, the major and minor axes, of which, are defined by the integral length-scales of the turbulence.

3.2.3 Far-Field Spectral Density

As has been shown in the previous section, many approximations exist to model the correlation tensor $\mathbf{R}_{ijkl}$. As an example, if the homogeneous isotropic (Ribner) model is selected, the far-field spectral density due to self-noise from an elemental volume of turbulence may be obtained by substituting equations (3.12) to (3.16) and equation (3.21) into equation (3.10) to give

$$dS\left(\mathbf{x}, \mathbf{x_s}, \omega\right) = \frac{\omega^4 \, l_t^3 \, \tau_t \, \overline{\rho}^{\,2} \, \overline{u_t^2}^2}{128\pi^3 c_0^4 r^2} \exp\left(-\frac{\omega^2}{8\pi}\left(C^2\tau_t^2 + \frac{l_t^2}{c_0^2}\right)\right) dV \,, \tag{3.31}$$

where dV is the volume of the element. The total spectral density from the jet is obtained by integrating this equation over the jet volume.

For this set of approximations, set out by Ribner for homogeneous isotropic turbulence, statistically describing the turbulence has been reduced to evaluating $\overline{u_t^2}$, l_t and τ_t – the isotropic turbulent kinetic energy, integral length-scale and integral time-scale. These values may be obtained from a RANS solution with a $\kappa - \epsilon$ turbulence model of the jet flow.

3.3 The Tam-Auriault Method

Tam and Auriault [81] developed a jet noise prediction method for small-scale turbulence, in which the sound sources are modelled explicitly. The method is based on the heuristic argument that the small-scale turbulence generates local pressure fluctuations that are proportional to the local turbulent kinetic energy per unit volume.

In the kinetic theory of gases, the pressure is given by

$$p = \frac{1}{3} mn \left\langle \mathbf{u}.\mathbf{u} \right\rangle = \frac{1}{3} \rho \left\langle \mathbf{u}^2 \right\rangle \,, \tag{3.32}$$

where m is the mass of a molecule, n is the number density, $\mathbf{u}$ is the random molecular velocity, ρ is the density of the gas, and $\langle\,\rangle$ is the ensemble average. Considering the small-scale turbulence as small blobs of fluid moving randomly, a direct analogy is made with the gas molecules, such that the fine-scale turbulence effectively exerts a

pressure, p_{turb}, on its surroundings given by

$$p_{turb} = q_t \equiv \frac{1}{3}\rho\left\langle \mathbf{u}^2 \right\rangle = \frac{2}{3}\rho k_t \,, \tag{3.33}$$

where $k_t = \left\langle \mathbf{u}^2 \right\rangle /2$ is the kinetic energy of the fine-scale turbulence per unit mass.

Once sound has been generated by these pressure fluctuations, its propagation is described by the linearised Euler equations. With a locally parallel approximation, the mean flow properties are

$$\overline{p} = p_0 \,; \quad \overline{\rho} = \overline{\rho}\,(r) \,; \quad \overline{u}_1 = \overline{u}_1\,(r) \quad \text{and} \quad \overline{u}_2 = \overline{u}_3 = 0 \,, \tag{3.34}$$

where $\overline{p}$ is the mean pressure, $\overline{\rho}$ is the mean density and $(\overline{u}_1,\, \overline{u}_2,\, \overline{u}_3)$ are the mean velocity components in cylindrical coordinates, $(x,\, r,\, \phi)$, aligned with the jet axis. With this approximation, the governing equations can be written in the linearised form [81]

$$\overline{\rho}\left[\frac{\partial u_1'}{\partial t} + \overline{u}_1\frac{\partial u_1'}{\partial x} + u_2'\frac{\partial \overline{u}_1}{\partial r}\right] + \frac{\partial p'}{\partial x} = -\frac{\partial q_t}{\partial x} \,, \tag{3.35a}$$

$$\overline{\rho}\left[\frac{\partial u_2'}{\partial t} + \overline{u}_1\frac{\partial u_2'}{\partial x}\right] + \frac{\partial p'}{\partial r} = -\frac{\partial q_t}{\partial r} \,, \tag{3.35b}$$

$$\overline{\rho}\left[\frac{\partial u_3'}{\partial t} + \overline{u}_1\frac{\partial u_3'}{\partial x}\right] + \frac{1}{r}\frac{\partial p'}{\partial \phi} = -\frac{1}{r}\frac{\partial q_t}{\partial \phi} \,, \tag{3.35c}$$

$$\frac{\partial p'}{\partial t} + \overline{u}_1\frac{\partial p'}{\partial x} + \gamma\overline{p}\left[\frac{1}{r}\frac{\partial\,(u_2' r)}{\partial r} + \frac{1}{r}\frac{\partial u_3'}{\partial \phi} + \frac{\partial u_1'}{\partial x}\right] = 0 \,, \tag{3.35d}$$

with $q_t = 2\,\overline{\rho}\,\hat{k}_t/3$ and where $(p',\, u_1',\, u_2',\, u_3')$ are the acoustic fluctuations. Molecular and eddy viscosity terms are ignored as they have only a relatively small effect on the acoustic disturbances. The variable $\hat{k}_t$ is the time dependent part of the kinetic energy of the small-scale turbulence. Equations (3.35) imply that $\hat{k}_t$ acts as a source of noise in the three components of the momentum equation.

3.3.1 Solving the Adjoint Formulation

Rather than converting the operators on the left-hand-side of equations (3.35) into Lilley's equation, Tam and Auriault make use of the adjoint equations [42]. They show that the periodic Green's function for the linearised Euler equations is related

to the solution of the adjoint Euler equations by

$$\hat{p}_1(\mathbf{x}, \mathbf{x_s}, \omega) = u_{1a}(\mathbf{x_s}, \mathbf{x}, \omega) , \tag{3.36a}$$

$$\hat{p}_2(\mathbf{x}, \mathbf{x_s}, \omega) = u_{2a}(\mathbf{x_s}, \mathbf{x}, \omega) , \tag{3.36b}$$

$$\hat{p}_3(\mathbf{x}, \mathbf{x_s}, \omega) = u_{3a}(\mathbf{x_s}, \mathbf{x}, \omega) , \tag{3.36c}$$

where $\hat{p}_n$, for $n = 1, 2, 3$, are the Green's functions for the sources in the x, r and ϕ components of the linearised momentum equations, respectively, and u_{1a}, u_{2a} and u_{3a} are the solutions to the adjoint equations. Note the reciprocal dependence between the observer, $\mathbf{x}$, and the source, $\mathbf{x_s}$. The adjoint equations are given by

$$-\overline{\rho}\left[i\omega u_{1a} + \overline{u}_1 \frac{\partial u_{1a}}{\partial x}\right] - \gamma\overline{p}\frac{\partial p_a}{\partial x} = 0 \tag{3.37a}$$

$$-\overline{\rho}\left[i\omega u_{2a} + \overline{u}_1 \frac{\partial u_{2a}}{\partial x} - u_{1a}\frac{\partial \overline{u}_1}{\partial r}\right] - \gamma\overline{p}\frac{\partial p_a}{\partial r} = 0 \tag{3.37b}$$

$$-\overline{\rho}\left[i\omega u_{3a} + \overline{u}_1 \frac{\partial u_{3a}}{\partial x}\right] - \frac{\gamma\overline{p}}{r}\frac{\partial p_a}{\partial \phi} = 0 \tag{3.37c}$$

$$-i\omega p_a - \overline{u}_1\frac{\partial p_a}{\partial x} - \left[\frac{1}{r}\frac{\partial (u_{2a} r)}{\partial r} + \frac{1}{r}\frac{\partial u_{3a}}{\partial \phi} + \frac{\partial u_{1a}}{\partial x}\right] = \frac{1}{2\pi}\delta(\mathbf{x_s} - \mathbf{x}) \tag{3.37d}$$

In the adjoint problem, the observer is located inside the jet at $\mathbf{x_s}$, and the source is in the far-field at $\mathbf{x}$. Using the adjoint Green's function, the pressure field is given by

$$p'(\mathbf{x}, t) = \int\int\left[\int_{-\infty}^{\infty} p_a(\mathbf{x_s}, \mathbf{x}, \omega)\exp\left(-i\omega(t - t_s)\right) d\omega\right]\frac{Dq_t(\mathbf{x_s}, t_s)}{Dt_s}\, dt_s\, d\mathbf{x_s} , \tag{3.38}$$

where $D/Dt_s = \partial/\partial t_s + \overline{u}_1\,\partial/\partial x_s$ is the convective derivative following the mean flow. With this adjoint formulation, only one calculation of a Green's function is required, instead of three with the direct formulation, therefore providing computational savings. Additionally, if the number of receiver points in far-field is less than the number of points in the jet flow, it may be computationally cheaper to evaluate the Green's function for a source at each receiver point rather than a source at each point in the flow [80]. However, for a shielding problem, where each point on the shield is effectively a receiver, this may not be the case.

3.3.2 Modelling the Source Term

The spectral density of the radiated sound is expressed as

$$S(\mathbf{x},\omega) = \int \dots \int p_a(\mathbf{x_1},\mathbf{x},\omega_1)\, p_a(\mathbf{x_2},\mathbf{x},\omega_2) \left\langle \frac{Dq_t(\mathbf{x_1},t_1)}{Dt_1} \frac{Dq_t(\mathbf{x_2},t_2)}{Dt_2} \right\rangle \times \exp\left(-i(\omega_1+\omega_2)t + i\omega_1 t_1 + i\omega_2 t_2\right) \delta(\omega-\omega_2)\, d\omega_1\, d\omega_2\, dt_1\, dt_2\, d\mathbf{x_1}\, d\mathbf{x_2}\,. \tag{3.39}$$

As the Tam-Auriault model is based on an acoustic analogy, it is necessary to make some some assumptions about the correlation function for the source term. It is assumed that the two-point cross-correlation of the axial velocity fluctuations in a fixed reference frame is

$$\left\langle \frac{Dq_t(\mathbf{x_1},t_1)}{Dt_1} \frac{Dq_t(\mathbf{x_2},t_2)}{Dt_2} \right\rangle = \frac{\hat{q}_t^2}{\tau_t^2} \exp\left(-\frac{|\eta_1|}{\overline{u}_1\tau_t} - \frac{\ln 2}{l_t^2}\left((\eta_1-\overline{u}_1\tau)^2+\eta_2^2+\eta_3^2\right)\right), \tag{3.40}$$

where $\boldsymbol{\eta} = \mathbf{x_1} - \mathbf{x_2}$; $\tau = t_1 - t_2$; l_t is the characteristic length-scale of the turbulence, τ_t is the characteristic time-scale and $\hat{q}_t$ is the root-mean-square value of the fluctuating kinetic energy of the small-scale turbulence.

Upon inserting equation (3.40) into equation (3.39), (and following the manipulation described in reference [81]) the spectral density of the sound radiated from an elemental volume is given by

$$dS(\mathbf{x},\mathbf{x_s},\omega) = 4\pi \left(\frac{\pi}{\ln 2}\right)^{3/2} \frac{\hat{q}_t^2 l_t^3}{\tau_t} |p_a(\mathbf{x_s},\mathbf{x},\omega)|^2 \frac{\exp\left(\frac{-\omega^2 l_t^2}{\overline{u}_1^2(4\ln 2)}\right)}{1+\omega^2\tau_t^2\left(1-\frac{\overline{u}_1}{c_0}\cos\theta\right)^2}\, dV\,. \tag{3.41}$$

3.3.3 Adjoint Green's Function

Evaluating the radiated sound requires the calculation of the adjoint Green's function, which can take into account the propagation effects between the source and the receiver. These effects can be divided in two contributions – firstly, the scattering of the acoustic wave due to a solid boundary, such as an acoustic shield; and secondly, mean flow effects on the propagation [80].

If the flow effects are neglected – it is assumed that $\overline{u}_1 = 0$ and that the mean desnsity, $\overline{\rho}$, is constant – then the adjoint equations (equations 3.37)) reduce to the

Helmholtz equation

$$\nabla^2 p_a + \frac{\omega^2}{c_0^2} p_a = \frac{i\omega}{2\pi c_0^2} \delta\left(\mathbf{x} - \mathbf{x_s}\right) . \tag{3.42}$$

In this case, the Green's function may be evaluated using known free-space Green's functions or through numerical propagation methods, for example, using a Boundary Element Method (BEM). In the free-space case

$$|p_a\left(\mathbf{x_s}, \mathbf{x}, \omega\right)|^2 = \frac{\omega^2}{64\pi^4 c_0^4 r^2} . \tag{3.43}$$

where $r = |\mathbf{x_s} - \mathbf{x}|$ and so the spectral density from an elemental volume is

$$dS\left(\mathbf{x}, \mathbf{x_s}, \omega\right) = \frac{\omega^2}{16\pi^3 c_0^4 r^2} \left(\frac{\pi}{\ln 2}\right)^{3/2} \frac{\hat{q}_t^2 l_t^3}{\tau_t} \frac{\exp\left(\frac{-\omega^2 l_t^2}{\overline{u}_1^2 (4 \ln 2)}\right)}{1 + \omega^2 \tau_t^2 \left(1 - \frac{\overline{u}_1}{c_0} \cos\theta\right)^2} dV . \tag{3.44}$$

For the Tam-Auriault method, it is necessary to evaluate parameters $\hat{q}_t^2$, l_t and τ_t. As with Lighthill's analogy, these values may be obtained from a RANS solution with a $\kappa - \epsilon$ turbulence model of the jet flow.

3.4 RANS Input

A RANS solution with $\kappa - \epsilon$ model provides only two pieces of information about the turbulence of the jet flow. These are the averaged turbulence kinetic energy κ and dissipation rate ϵ. From these quantities it is possible to form a length l, characterising the size of the turbulence, and a time τ, characterising the decay time of the turbulence [81, 65]. The model parameters l_t and τ_t are proportional to these values and may be given as

$$l_t = c_l \left(\kappa^{3/2}/\epsilon\right) ; \qquad \tau_t = c_\tau \left(\kappa/\epsilon\right) . \tag{3.45}$$

For the Lighthill-Ribner model, the isotropic turbulent kinetic energy may be given as

$$\overline{u_t^2} = c_A \left(2\kappa/3\right) , \tag{3.46}$$

while for the Tam-Auriault model the source strength is taken to be

$$\hat{q}_t^2 = c_A^2 \left(2\overline{\rho}\,\kappa/3\right)^2 . \tag{3.47}$$

It is clear that the source strength in the two models are related.

3.5 Discussion

The main differences between the Lighthill-Ribner, and the Tam-Auriault jet noise models may be summarised [65] as:

- Lighthill equation is a re-expression of the full equations of motion with the acoustic propagation described by the wave equation. It is inherent that a change in the propagation medium changes the source term. The Tam-Auriault model contains a heuristic argument to create a noise source term and uses the linearised Euler equations to describe the propagation of sound generated by this model source. The source is the same regardless of approximations made about the propagation medium.

- It is assumed in Lighthill's analogy that the source is compact, and that the Green's function is simply the free-space Green's function for the wave equation. In the Tam-Auriault method, there is no explicit assumption concerning the compactness of the source (though it is implied), and the Green's function is obtained from the adjoint solution of the linearized Euler equations.

- In Lighthill's analogy, the cross-correlation function is of the Lighthill stress tensor, whereas, in the Tam-Auriault model it is of the convective derivative of the source term.

As noted by Morris [66], this final point is very important as the convective derivative only appears on the source term in the Tam-Auriault model following an integration-by-parts to move it there from the adjoint Green's function. This arbitrary transfer would appear to be the crucial difference, that leads to the apparent improvement of predictions by this model, over those by Lighthill's analogy based models.

Chapter 4

A Jet Source Localisation Strategy

As far-field noise predictions have focused on isolated free jets, the jet has traditionally been considered as a single volume. Indeed, the entire jet is often considered to be located, in effect, at the origin of the coordinates (the centre of the jet exit plane is usually selected as the origin), with the distance separating the entire source region and the receiver reduced from $r = |\mathbf{x} - \mathbf{x_s}|$ to $r \approx |\mathbf{x}|$. In the modelling of jet noise shielding, the spatial extent of the jet can not be neglected, as it is desirable to position the shield near the jet, both, in order to achieve maximum shielding and to meet realistic aircraft design requirements. In this chapter, a strategy to replace the total jet volume with a number of sub-volumes is described. These sub-volumes are then used to weight point sources for use in shielding prediction methods. The jet noise is modelled using a new form of Lighthill's acoustic analogy.

4.1 A Jet Noise Model for Shielding Applications

A solution to Lighthill's equation may be derived using the same strategy as Tam and Auriault's. The Green's function, $\mathrm{G}(\mathbf{x}, \mathbf{x_s}, t, t_\mathbf{s})$, is given by the solution of

$$\frac{\partial^2 \mathrm{G}}{\partial t^2} - c_0^2 \nabla^2 \mathrm{G} = c_0^2 \, \delta(\mathbf{x} - \mathbf{x_s}) \, \delta(t - t_s) \, . \tag{4.1}$$

The Fourier transform of this equation is

$$\left(\nabla^2 + k^2\right) \hat{\mathrm{G}}\left(\mathbf{x}, \mathbf{x_s}, \omega\right) = -\frac{\delta\left(\mathbf{x} - \mathbf{x_s}\right)}{2\pi}, \tag{4.2}$$

which has a free-space solution of

$$\hat{\mathrm{G}}\left(\mathbf{x}, \mathbf{x_s}, \omega\right) = \frac{1}{8\pi^2} \frac{\exp\left(ik|\mathbf{x} - \mathbf{x_s}|\right)}{|\mathbf{x} - \mathbf{x_s}|} \tag{4.3}$$

From Lighthill's equation (equation (3.1)), the far-field density fluctuations may written as

$$\rho'\left(\mathbf{x}, t\right) = \frac{1}{c_0^2} \int\int\int \hat{\mathrm{G}}\left(\mathbf{x}, \mathbf{x_s}, \omega\right) \frac{\partial^2 T_{ij}}{\partial x_{si} \partial x_{sj}} \left(\mathbf{x_s}, t_s\right) \exp\left(-i\omega\left(t - t_s\right)\right) \, d\omega \, dt_s \, d\mathbf{x_s}, \tag{4.4}$$

where

$$\mathrm{G}\left(\mathbf{x}, \mathbf{x_s}, t, t_s\right) = \int_{-\infty}^{\infty} \hat{\mathrm{G}}\left(\mathbf{x}, \mathbf{x_s}, \omega\right) \exp\left(-i\omega\left(t - t_s\right)\right) \, d\omega \, . \tag{4.5}$$

Instead of evaluating the frequency and time integrals at this point, as is usually done in traditional Lighthill based methods, the Tam and Auriault approach is adopted in order to retain an explicit Green's function term in the spectral density expression. This Green's function may subsequently be modelled to include a scattering object.

The Tam-Auriault method has been shown to agree well with a wide set of jet noise data [81]. This apparent improvement over traditional Lighthill based predictions may possibly be attributed to the fact that it is a derivative of the source, which is modelled in the cross-correlation, as opposed to the source itself in traditional Lighthill models [65]. The Lighthill model may be derived to use the same type of correlation model as the Tam and Auriault model, if one derivative is transferred to the Green's function through integration-by-parts, while the other is retained on the source. Although this transfer is arbitrary, it may possibly improve jet noise predictions. Therefore, equation (4.4) becomes

$$\rho'\left(\mathbf{x}, t\right) = -\frac{1}{c_0^2} \int\int\int \frac{\partial \hat{\mathrm{G}}}{\partial x_{si}} \left(\mathbf{x}, \mathbf{x_s}, \omega\right) \frac{\partial T_{ij}}{\partial x_{sj}} \left(\mathbf{x_s}, t_s\right) \exp\left(-i\omega\left(t - t_s\right)\right) \, d\omega \, dt_s \, d\mathbf{x_s} \, . \tag{4.6}$$

To simplify the analyses, the shear-noise terms in the correlation are neglected and the various i and j components of this equation are replaced by a single component in the direction of the receiver, as shown by Proudman [71]. The spectral density of the radiated sound may be expressed as

$$S(\mathbf{x},\omega) = \int \cdots \int \frac{\partial \hat{\mathrm{G}}(\mathbf{x},\mathbf{x_1},\omega)}{\partial x_{1r}} \frac{\partial \hat{\mathrm{G}}(\mathbf{x},\mathbf{x_2},\omega)}{\partial x_{2r}} \left\langle \frac{\partial T_{rr}(\mathbf{x_1},t_1)}{\partial x_{1r}} \frac{\partial T_{rr}(\mathbf{x_2},t_2)}{\partial x_{2r}} \right\rangle \times \exp\left(-i(\omega_1+\omega_2)t + i\omega_1 t_1 + i\omega_2 t_2\right) \delta(\omega-\omega_2)\, d\omega_1\, d\omega_2\, dt_1\, dt_2\, d\mathbf{x_1}\, d\mathbf{x_2}\,. \tag{4.7}$$

The shape of the spatial correlation functions in the Lighthill-Ribner (equation (3.15)), and Tam-Auriault (equation (3.40)) models are essentially the same. The difference is that the Lighthill-Ribner version is in a moving reference frame, whereas the Tam-Auriault one is given in a fixed reference frame, and so, the time and space separations are related by the convection velocity as $\tau = \eta/U_c$. Additionally, the temporal function in the Lighthill-Ribner model is from equation 3.21, whereas the Tam-Aurialt temporal function takes the order of equation 3.20.

A correlation function selected for the present model, which retains the shape of the Lighthill-Ribner function, in a fixed reference frame is

$$\left\langle \frac{\partial T_{rr}(\mathbf{x_1},t_1)}{\partial x_{1r}} \frac{\partial T_{rr}(\mathbf{x_2},t_2)}{\partial x_{2r}} \right\rangle = \frac{\overline{\rho}^2\, \overline{u_t^2}^2}{l_t^2} \exp\left(-\frac{\pi\eta_1^2}{U_c^2\tau_t^2} - \frac{\pi}{l_t^2}\left((\eta_1 - U_c\tau)^2 + \eta_2^2 + \eta_3^2\right)\right), \tag{4.8}$$

where $\boldsymbol{\eta} = \mathbf{x_2} - \mathbf{x_1}$; $\tau = t_2 - t_1$; l_t is the characteristic length-scale of the turbulence; τ_t is the characteristic time-scale and $\overline{u_t^2}$ is the isotropic turbulent kinetic energy. U_c is the convection velocity in the axial direction. It should be recalled that realistic jet turbulence is neither homogeneous nor isotropic. However, the present selection of a homogeneous isotropic turbulence correlation function is made as it simplifies the following analyses, and the introduction of additional complexity at this point would not enhance the present investigation (see chapter 5 and 6). A more realistic turbulence model could be introduced at a later stage.

Inserting this correlation model back into equation into equation (4.7) and evaluating the frequency and time integrals (following the manipulation shown in

Tam and Auriault's paper [81]) leads to

$$S(\mathbf{x},\omega) = 2\pi \int\int \frac{\partial \hat{\mathrm{G}}}{\partial x_{1r}}(\mathbf{x},\mathbf{x_1},-\omega)\,\frac{\partial \hat{\mathrm{G}}}{\partial x_{2r}}(\mathbf{x},\mathbf{x_2},\omega)\,\frac{\overline{\rho}^2\,\overline{u_t^2}^2}{l_t^2}\,\frac{l_t}{U_c} \times \exp\left(-\frac{\omega^2 l_s^2}{4\pi U_c^2} + \frac{i\omega\eta_1}{U_c}\right)\exp\left(-\frac{\pi\eta_1^2}{U_c^2\tau_t^2} - \frac{\pi}{l_t^2}\left(\eta_2^2+\eta_3^2\right)\right)\,d\mathbf{x_1}\,d\mathbf{x_2}\,. \quad (4.9)$$

The derivatives of the Green's functions in the direction of the receiver may be approximated as

$$\frac{\partial \hat{\mathrm{G}}}{\partial x_{1r}}(\mathbf{x},\mathbf{x_1},-\omega)\,\frac{\partial \hat{\mathrm{G}}}{\partial x_{2r}}(\mathbf{x},\mathbf{x_2},\omega) \approx \frac{\omega^2}{c_0^2}\,\hat{\mathrm{G}}(\mathbf{x},\mathbf{x_1},-\omega)\,\hat{\mathrm{G}}(\mathbf{x},\mathbf{x_2},\omega)\,. \quad (4.10)$$

For compact sources $\hat{\mathrm{G}}(\mathbf{x},\mathbf{x_1},\omega)$ may be related to $\hat{\mathrm{G}}(\mathbf{x},\mathbf{x_2},\omega)$ by a simple phase shift, as in the Tam-Auriault method [81], such that

$$\hat{\mathrm{G}}(\mathbf{x},\mathbf{x_2},\omega) \approx \hat{\mathrm{G}}(\mathbf{x},\mathbf{x_1},\omega)\exp\left(-i\frac{\omega}{c_0}\eta_1\cos\theta\right)\,, \quad (4.11)$$

where θ is the angle between the receiver and the downstream jet axis. Upon evaluating the spatial integrals over all spatial separations, and noting that $\hat{\mathrm{G}}(\mathbf{x},\mathbf{x_1},-\omega)$ is the complex conjugate of $\hat{\mathrm{G}}(\mathbf{x},\mathbf{x_1},\omega)$, the far-field spectral density from an elemental volume may finally be expressed as

$$dS(\mathbf{x},\mathbf{x_s},\omega) = \frac{\omega^2\,l_t\tau_t\,2\pi\,\overline{\rho}^2\,\overline{u_t^2}^2}{c_0^2}\,|\,\hat{\mathrm{G}}(\mathbf{x},\mathbf{x_s},\omega)\,|^2\,\exp\left(-\frac{\omega^2}{4\pi}\left(C^2\tau_t^2 + \frac{l_t^2}{U_c^2}\right)\right)\,dV\,, \quad (4.12)$$

where $C = 1 - M_c\cos\theta$ is the convection factor and the volume of the element is dV.

A RANS solution provides the necessary local mean values, τ_t, l_t and $\overline{u_t^2}$ (see section 3.4), and so each element is taken to be a discrete cell in the RANS mesh. This form has the benefit that the Green's function is explicit and may be evaluated to include the scattering by a shielding surface.

In the absence of a shielding surface, inserting equation (4.3) into equation (4.12) gives

$$dS(\mathbf{x},\mathbf{x_s},\omega) = \frac{\omega^2\,l_t\tau_t\,\overline{\rho}^2\,\overline{u_t^2}^2}{32\pi^3 c_0^2 r^2}\,\exp\left(-\frac{\omega^2}{4\pi}\left(C^2\tau_t^2 + \frac{l_t^2}{U_c^2}\right)\right)\,dV\,. \quad (4.13)$$

This equation is clearly very similar to equation (3.31), which was derived using Ribner's approximations. The difference is that the frequency weighting is now of the same order as that in the Tam-Auriault method. The far-field spectral density from the total jet is

$$S(\mathbf{x}, \omega) = \int_V dS\,, \tag{4.14}$$

where V is the total jet volume.

4.2 Point Source Distribution for Shielding Applications

Equation (4.12) may be rewritten as

$$dS(\mathbf{x}, \mathbf{x_s}, \omega) = A^2(\mathbf{x}, \mathbf{x_s}, \omega)\; dV\, |\, \hat{\mathrm{G}}(\mathbf{x}, \mathbf{x_s}, \omega)\, |^2\,, \tag{4.15}$$

where

$$A^2(\mathbf{x}, \mathbf{x_s}, \omega) = \frac{2\pi\, \overline{\rho}^2\, \overline{u_t^2}^2}{c_0^2} \omega^2\, l_t \tau_t\, \exp\left(-\frac{\omega^2}{4\pi}\left(C^2\tau_t^2 + \frac{l_t^2}{U_c^2}\right)\right)\,, \tag{4.16}$$

is a local directional amplitude term.

For jet noise shielding computations, it is desirable to model the jet as a distribution of point sources. To this end, equation (4.15) is rewritten as

$$|\, \hat{p}(\mathbf{x}, \mathbf{x_s}, \omega)\, |^2 = A^2(\mathbf{x}, \mathbf{x_s}, \omega)\; dV\, |\, \hat{\mathrm{G}}(\mathbf{x}, \mathbf{x_s}, \omega)\, |^2\,, \tag{4.17}$$

which represents a point source concentrated at the centroid of the element, $\mathbf{x_s}$. As this source is resultant from the integration over all space-time separations, all interaction effects between the source and surrounding elements in the jet have been included in the amplitude. The sound fields produced by a distribution of such sources, located at the centroid of each element in the RANS mesh, may also be considered incoherent, and so will sum as

$$|\, \hat{p}(\mathbf{x}, \omega)\, |^2 = \sum_{i=1}^{N_S} |\, \hat{p}_i(\mathbf{x}, \mathbf{x_s}, \omega)\, |^2\,, \tag{4.18}$$

where N_S is the elements that comprise the total jet. Importantly, as the phase relationship between the sources is not important, any phase may assumed for the

purposes of computing the diffraction about a shielding object for an individual source.

The amplitude term acts as a directional spatial frequency filter. Observe that over an arc of far-field receivers, for a fixed receiver angular frequency, ω, the term A amplifies source frequencies lower than ω at downstream angles, and source frequencies higher than ω at upstream angles, due to the convection term C. This is expected with sources that are convected downstream relative to the receiver. For jet noise, it implies that at downstream receiver angles, the sound originates from a turbulent region that is located further downstream than is the case at upstream receiver angles (as it is known that the characteristic frequency of the turbulence decreases with axial distance from the nozzle exit). In other words, the source location is not fixed for a given frequency but is dependent on the receiver location.

4.3 Reducing the Number of Sources

For an axisymmetric RANS simulation of a jet flow, it is normally the case that $N_S > 10^4$. For a 3D jet this number is even greater. It is prohibitive to retain a large number of point sources to represent the jet noise source for a number of reasons:

- If a source is located at each cell in the mesh used for the RANS computation, then inevitably there will be redundant or *zero* amplitude sources. These increase the computational demands and may be located in unrealistic locations (for example, inside the shielding surface or upstream in the nozzle duct).

- As the sources do not sum coherently, local interference effects between the sources are not important, and only the overall power from a local region is relevant to the sound field. It is, therefore, unnecessary to have a dense distribution of sources, as the contribution to the total acoustic pressure from sources located within a small distance of each other, can be achieved from a single stronger source located at an averaged location.

- It can become computationally very expensive to compute and store the sound

field from a large number of sources by numerical propagation, or at a large number of receivers, as required at a shielding surface.

As this is intended to be a practical approach to modelling jet noise for shielding applications some pragmatic steps are now taken to minimise the number of sources.

4.3.1 Defining the Jet Volume

Although the jet volume, V, has been introduced earlier, it has yet to been defined. RANS domains for jet computations often contain nozzle ducts and numerical *buffer-zones*. These regions, along with the *silent* potential-core, do not contribute to the jet noise, and should be removed.

The most simple approach to removing redundant source regions is to use a *cut-off* criteria, where only elements, which meet the criteria value, are included in V. The jet volume is thus defined by

$$\mathbf{x_s} \in V \qquad \text{if} \qquad F_W(\mathbf{x_s}) \geq \alpha \left(F_W(\mathbf{x_s})\right)_{max} , \tag{4.19}$$

where F_W is a weight distribution across the domain and $0 \leq \alpha \leq 1$ is an appropriately selected cut-off factor.

For example, if the turbulent kinetic energy is used as F_W, with $\alpha = 0.1$, then only elements with a turbulent kinetic energy of at least 10% of the maximum value are considered to be in the jet. The turbulent kinetic energy is, however, an unsatisfactory variable, as it is difficult to define a cut-off value, which both retains enough sources to define the source region over a range of frequencies, and limits the number of redundant sources.

A more appropriate choice for F_W is the frequency dependant amplitude of equation (4.16). As the amplitude term is also dependent on the angle between the receiver and the jet axis, direct use of this term would result in a set of sources for each receiver position. To avoid this undesirable jet volume definition, the amplitude is averaged over a sphere of receiver positions, to give

$$F_W(\mathbf{x_s}, \omega) = \frac{1}{2} \int_0^{\pi} A(\mathbf{x}, \mathbf{x_s}, \omega) \sin\theta \, d\theta \, . \tag{4.20}$$

This equation, along with equation (4.19), may be used to define a frequency dependent jet source volume, V.

4.3.2 Localisation of Jet Sources

The jet domain, V, (defined in previous section) will still contain a large number of elements. If each element is replaced by a point source, there is still an excessively large number of sources for use in a shielding computation. The jet volume may be divided into a number of sub-volumes or *blocks*, in which, the contribution from individual elements is combined into a single source block. The total jet volume is decomposed into

$$V = \sum_{i=1}^{N_B} \Delta V_i \,, \tag{4.21}$$

where N_B is the number of blocks that comprise the total jet. The far-field spectral density is therefore

$$S\left(\mathbf{x}, \omega\right) = \sum_{i=1}^{N_B} \left(\int_{\Delta V_i} dS \right) = \sum_{i=1}^{N_B} \Delta S_i \left(\mathbf{x}, \mathbf{x_b}, \omega\right) \,, \tag{4.22}$$

and the spectral density from an individual block is

$$\Delta S\left(\mathbf{x}, \mathbf{x_b}, \omega\right) = \int_{\Delta V} A^2 \left(\mathbf{x}, \mathbf{x_s}, \omega\right) \mid \hat{\mathrm{G}}\left(\mathbf{x}, \mathbf{x_s}, \omega\right) \mid^2 d\mathbf{x_s} \,, \tag{4.23}$$

and $\mathbf{x_b}$ is the centroid of the block. In order to define directional point sources with the same form as equation (4.17), *averaged* values of τ_t, l_t, and U_c are evaluated, using F_W to weight the elements within the block.

Splitting the amplitude term into components so that

$$A\left(\mathbf{x}, \mathbf{x_s}, \omega\right) = A_{\mathbf{s}}\left(\mathbf{x_s}\right) A_\omega \left(\mathbf{x}, \mathbf{x_s}, \omega\right) \,, \tag{4.24}$$

with

$$A_{\mathbf{s}}^2 \left(\mathbf{x_s}\right) = \frac{2\pi\, \overline{\rho}^2\, \overline{u_t^2}^2}{c_0^2} \,, \tag{4.25}$$

is a local amplitude (independent of receiver position), and

$$A_\omega^2 \left(\mathbf{x}, \mathbf{x_s}, \omega\right) = \omega^2\, l_t \tau_t \, \exp\left(-\frac{\omega^2}{4\pi} \left(C^2 \tau_t^2 + \frac{l_t^2}{U_c^2} \right) \right) \,, \tag{4.26}$$

is a directional frequency filter. The spectral density from a block can, therefore, be expressed as

$$\Delta S\left(\mathbf{x},\mathbf{x_b},\omega\right)=\left\langle A_\omega^2\left(\mathbf{x},\mathbf{x_s},\omega\right)\right\rangle\,|\,\hat{\mathrm{G}}\left(\mathbf{x},\mathbf{x_b},\omega\right)|^2\int_{\Delta V}A_{\mathbf{s}}^2\left(\mathbf{x_s}\right)\,d\mathbf{x_s}\,, \tag{4.27}$$

and so

$$|\hat{p}\left(\mathbf{x},\mathbf{x_b},\omega\right)|^2=A_{\mathbf{b}}^2\left(\mathbf{x_b}\right)\,A_\omega^2\left(\mathbf{x},\mathbf{x_b},\omega\right)\,|\,\hat{\mathrm{G}}\left(\mathbf{x},\mathbf{x_b},\omega\right)|^2\,, \tag{4.28}$$

where

$$A_\omega^2\left(\mathbf{x},\mathbf{x_b},\omega\right)=\left\langle A_\omega^2\left(\mathbf{x},\mathbf{x_s},\omega\right)\right\rangle=\omega^2\,\left\langle l_t\right\rangle\left\langle\tau_t\right\rangle\,\exp\left(-\frac{\omega^2}{4\pi}\left(\left\langle C\right\rangle^2\left\langle\tau_t\right\rangle^2+\frac{\left\langle l_t\right\rangle^2}{\left\langle U_c\right\rangle^2}\right)\right)\,, \tag{4.29}$$

is the averaged directional amplitude filter; $\langle\,\rangle$ denotes the weighted-average over the block; $\langle C\rangle=1-\langle U_c\rangle\left(x_1-x_{\mathbf{b}1}\right)/c_0\,|\mathbf{x}-\mathbf{x_b}|$, and

$$A_{\mathbf{b}}^2\left(\mathbf{x_b}\right)=\int_{\Delta V}A_{\mathbf{s}}^2\left(\mathbf{x_s}\right)\,d\mathbf{x_s}\,, \tag{4.30}$$

is the amplitude of the point source. In this manner, the jet volume may be divided into a number of sub-volumes and each replaced by a directional point source. This *reduced* number of point sources may be used in shielding prediction methods, for which it is assumed that

$$\hat{p}\left(\mathbf{x},\mathbf{x_b},\omega\right)=A\left(\mathbf{x},\mathbf{x_b},\omega\right)\,\hat{\mathrm{G}}\left(\mathbf{x},\mathbf{x_b},\omega\right)=\frac{A\left(\mathbf{x},\mathbf{x_b},\omega\right)}{8\pi^2}\frac{\exp\left(ik|\mathbf{x}-\mathbf{x_b}|\right)}{|\mathbf{x}-\mathbf{x_b}|}\,, \tag{4.31}$$

where $A\left(\mathbf{x},\mathbf{x_b},\omega\right)=A_{\mathbf{b}}\left(\mathbf{x_b}\right)A_\omega\left(\mathbf{x},\mathbf{x_b},\omega\right)$.

4.3.3 Selecting Sub-Volume Dimensions

The quantity of point sources, which the jet may be reduced to, is dependent on the block size selected. However, there is no strict *rule* as to the scale of each block, or as to a minimum number sources, which should be retained. It may be prudent, though, to select a dimension small enough so as to maintain an effective representation of the jet – thus, it should be ensured that there are enough sources retained to adequately define the spatial extent of the jet and that the averaged

values are still somewhat representative of the values within the block, which they have replaced.

Uniformly spaced blocks, all of the same dimension, could be used. This has the appeal that the jet would be decomposed into a predefined number of sources, which may be of interest in determining the total computational requirements for a shielding prediction. The selection of L would, however, be completely arbitrary and, as such, it would be difficult to maintain an effective representation of the jet.

This trade-off, between reducing the number of sources to minimise the computational demand and maintaining enough sources to represent the jet, is best illustrated at its two extremes. Firstly, if the block size is the size of each element, $\Delta V = dV$, no reduction takes place and the number of sources remains large. Secondly, if the block size selected is that of the jet volume, $\Delta V = V$, there would be a single value for τ_t, l_t and U_c and $\mathbf{x_b}$ for the entire jet and a poor prediction of the jet noise shielding would be inevitable for all configurations of interest.

An appropriate scale for the block length, L, may be the integral length-scale, with $L \propto l_t$, as the length-scale is representative of the spatial extent of the turbulence, and it is reasonable to expect that the values of τ_t, l_t and U_c do not vary excessively over l_t.

A value for L must be defined before an averaged value of the length-scale is evaluated within the block. The following scheme is employed to define L, and to divide the jet into sub-volumes:

1. As the spatial extent of jet source region is primarily in the axial direction, L is defined as $L = L_\omega(x_1)$ and is computed by a linear least-squares fit of the l_t values across the jet volume, at the frequency in question, and so L is given by the equation

$$L_\omega(x_1) = a_L x_1 + b_L\,, \tag{4.32}$$

   where a_L and b_L are the linear coefficients resultant from the linear fit.

2. The axial extents of a discrete block i, denoted as $X_\pm \equiv x_{\mathbf{b}1,i} \pm L_{\omega,i}/2$, are

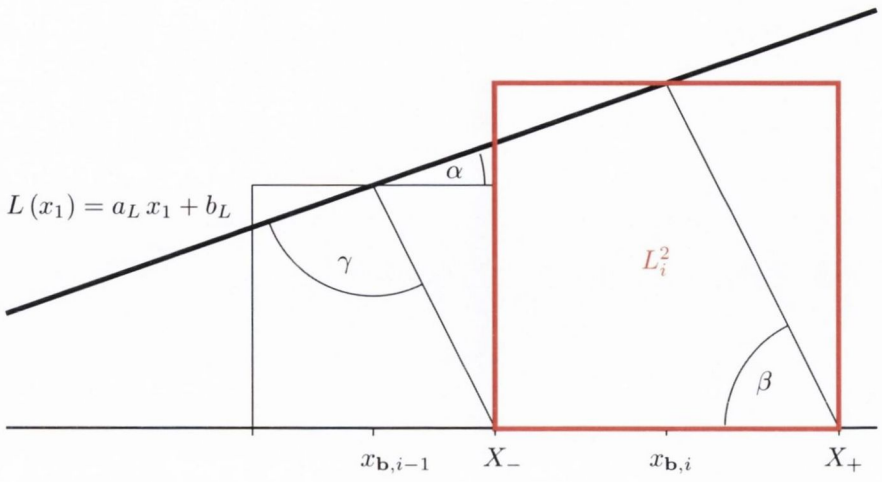

Figure 4.1: Schematic of spacing strategy.

used to locate $x_{\mathbf{b1},i}$ by

$$x_{\mathbf{b1},i} = X_+ - \frac{L_\omega(X_+)\tan(\pi/2-\alpha)\sin(\alpha)\sin(\beta)}{\sin(\gamma)}, \tag{4.33}$$

where $\alpha = \tan^{-1}(a_L)$; $\beta = \tan^{-1}(2)$; $\gamma = \pi - \alpha - \beta$, and

$$X_+ - X_- = L_\omega(x_{\mathbf{b1},i}), \tag{4.34}$$

by definition.

3. Starting by setting $X_+ = (x_{\mathbf{s1}})_{max}$ and iterating upstream, the jet is divided into axial slices.

4. Each slice, i, is further divided using $L_{\omega,i}$ (which is taken to be constant within the slice), thus defining $x_{\mathbf{b2},i}$, and so the volume of a block, for an axisymmetric jet, is given by

$$\Delta V_i = L_{\omega,i}^2 \, x_{\mathbf{b2},i} \, d\phi, \tag{4.35}$$

where ϕ is the azimuthal angle.

Using this strategy to split the jet into sub-volumes or blocks significantly reduces the number of point sources, which represent the jet, and as a result the computational requirements of a jet shielding computation.

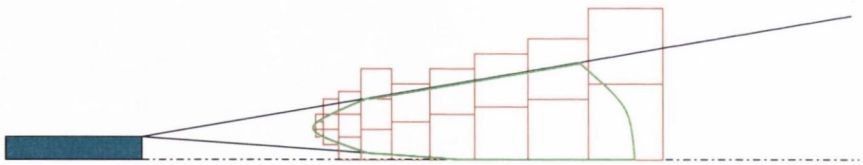

Figure 4.2: Schematic of the jet sub-volumes. The source region is bounded by the green line and the sub-volume are bounded by the red squares.

4.4 Jet Noise Shielding Prediction

The point sources defined in the previous two sections may be used as a jet noise source in shielding prediction methods. In order to investigate the agreement of these *jet* sources with test data, the Fresnel-Kirchhoff shielding method is employed. To predict the shielding factor at a receiver location $\mathbf{x}$ from an acoustic source at $\mathbf{x_s}$, attained by the insertion of a rigid barrier, the Fresnel-Kirchhoff method (FKM) considers the geometric complement of the problem [13], that is, a receiver separated from an acoustic source by a slot in an infinitely long rigid plate. The acoustic pressure at the receiver point may then be obtained using the Helmholtz-Kirchhoff integral equation,

$$\hat{p}\left(\mathbf{x},\mathbf{x_s},\omega\right) = \frac{1}{4\pi}\int_S \left(\hat{p}\left(\mathbf{s},\mathbf{x_s},\omega\right)\frac{\partial\lambda}{\partial\mathbf{n}}\left(\mathbf{s},\mathbf{x},\omega\right) - \lambda\left(\mathbf{s},\mathbf{x},\omega\right)\frac{\partial\hat{p}}{\partial\mathbf{n}}\left(\mathbf{s},\mathbf{x_s},\omega\right)\right) dS\,, \quad (4.36)$$

where $\mathbf{s}$ is a point on the surface S, $\mathbf{n}$ is a unit vector normal to the slot and $\lambda = \exp\left(jk|\mathbf{r}_\lambda|\right)/|\mathbf{r}_\lambda|$.

Assuming that the acoustic pressure on the shielded side of the infinitely long plate is zero and that the acoustic pressure field in the aperture is the same as it would be in a completely free-field, the Kirchhoff surface reduces to the area of the slot. These assumptions place significant limitations on the geometries and the Helmholtz numbers, to which the Fresnel-Kirchhoff method may be applied to.

If the limits of the slot are large, then Helmholtz-Kirchhoff equation can be approximated as

$$\hat{p}\left(\mathbf{x},\mathbf{x_s},\omega\right) = \frac{1}{2\pi}\int_S \hat{p}\left(\mathbf{s},\mathbf{x_s},\omega\right)\frac{\partial\lambda}{\partial\mathbf{n}}\left(\mathbf{s},\mathbf{x},\omega\right) dS\,, \quad (4.37)$$

through integration-by-parts.

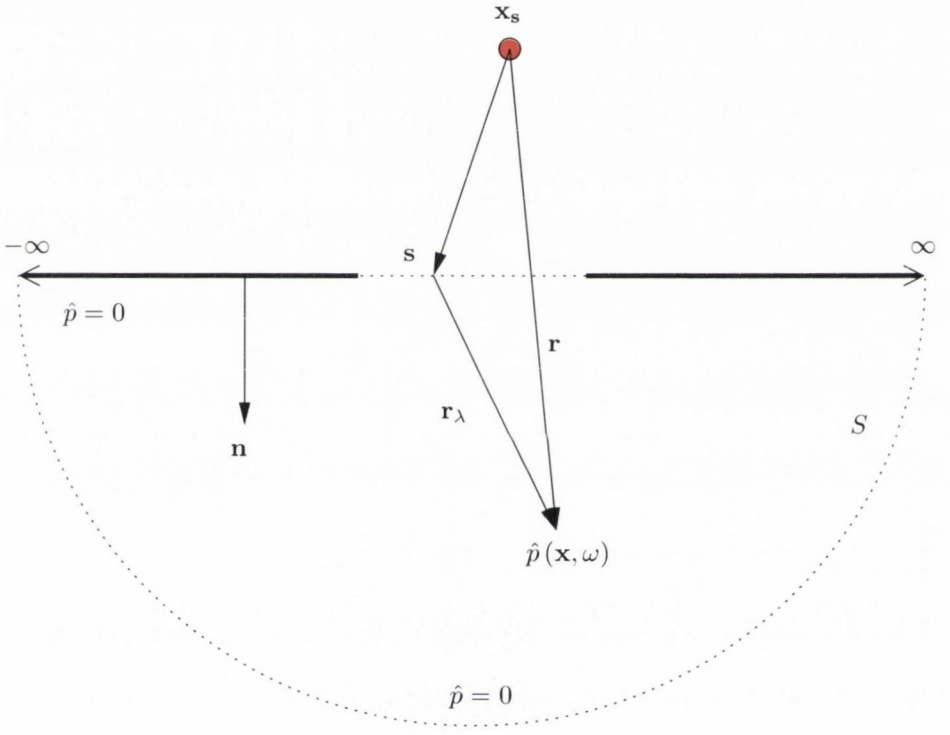

Figure 4.3: Schematic of the Fresnel-Kirchhoff shielding method.

Applying Babinet's principle, that complementary diffracting objects have complementary diffraction patterns, reverts the analysis back to the original shielding problem of interest, and so the *shielded* pressure at a receiver separated by a plate (with the dimensions of the slot) is given by

$$\hat{p}_{shield}\left(\mathbf{x}, \mathbf{x_s}, \omega\right) = \hat{p}_{ref}\left(\mathbf{x}, \mathbf{x_s}, \omega\right) - \hat{p}_{slot}\left(\mathbf{x}, \mathbf{x_s}, \omega\right) , \tag{4.38}$$

where $\hat{p}_{ref}$ is the free-space *isolated* pressure and $\hat{p}_{slot}$ is given by (4.37).

4.5 Mean Flow Refraction Effect

An implication of Lighthill's equation is that a homogeneous and non-moving propagation medium is imposed outside the local jet source region. Any change from this state would alter the source term, leading to Lilley's analogy for example. In a real jet, these conditions are not met. One aspect of the acoustic propagation of jet sources, which is neglected under these assumptions, is the refraction of the sound by the mean jet flow.

In order to take some account of this effect on jet noise shielding predictions, the assumption is made that the source can be assumed to be held fixed, despite the introduction of a mean flow. In some regards, this is similar to the approach of Tam and Auriault, who derived their source term heuristically and so assume it to be fixed for different flow conditions. The refraction of a point source by the mean jet flow is used to define a refraction correction factor,

$$F_R\left(\mathbf{x}, \mathbf{x_s}, \omega\right) = \frac{\left|\hat{p}_{flow}\left(\mathbf{x}, \mathbf{x_s}, \omega\right)\right|}{\left|\hat{p}_{ref}\left(\mathbf{x}, \mathbf{x_s}, \omega\right)\right|} , \tag{4.39}$$

which are to be included in the amplitude of the jet point sources in equation (4.31).

If the mean flow is assumed to be irrotational and inhomogeneous then it can be modelled as a potential flow, and the governing field equation for the velocity potential, ϕ, as shown by Pierce [69], is given by

$$\frac{1}{\overline{\rho}} \nabla . \left(\overline{\rho}\, \nabla \phi\right) - L\left(\frac{1}{\overline{c}^{\,2}} L\phi\right) = 0 , \tag{4.40}$$

where L is the complex linear operator $(i\omega + \overline{\mathbf{u}}.\nabla)$ and $\overline{\mathbf{u}}$, $\overline{\rho}$, $\overline{c}$, are the local mean velocity, density, and speed of sound respectively. The acoustic parts of the velocity

potential and pressure are related by

$$\hat{p} = -j\,\overline{\rho}\,\omega\phi - \overline{\rho}\,\overline{\mathbf{u}}.\nabla\phi\,. \tag{4.41}$$

Equation (A.1) may be solved efficiently, for example, using a wave expansion method (WEM) [22]. This method is described at length in Appendix A.

4.5.1 Wave Expansion Discretisation

The velocity potential at a discrete point, $\phi_{\mathbf{0}}$, (and so the acoustic pressure) may be computed from the amplitude and phase of M neighbouring points. The potential at each point in a domain may be approximated by the superposition of the field generated by N hypothetical plane waves of strength γ_n and with unit propagation in direction $\mathbf{d}_n$, as described by Caruthers [22], such that

$$\phi_{\mathbf{0}} = \sum_{n=1}^{N} \gamma_n \exp\left[-iq\left(\mathbf{d}.\mathbf{x_0}\right)\right] = \mathbf{h}\boldsymbol{\gamma}\,, \tag{4.42}$$

where $h_n = \exp\left[-iq\left(\mathbf{d}.\mathbf{x_0}\right)\right]$ (the subscript $\mathbf{0}$ denotes the value at the point in question and should not be confused with an ambient value),

$$q = \frac{i\mathbf{B_0}.\mathbf{d} \pm \sqrt{4K_{\mathbf{0}}^2\left(1-\left(\mathbf{M_0}.\mathbf{d}\right)^2\right) - \left(\mathbf{B_0}.\mathbf{d}\right)^2}}{2\left(1-\left(\mathbf{M_0}.\mathbf{d}\right)^2\right)}\,, \tag{4.43}$$

with

$$\mathbf{B_0} = 2ik\mathbf{M_0} + \overline{\mathbf{u}}_{\mathbf{0}}.\nabla\left(\frac{1}{\overline{c}_{\mathbf{0}}^{\,2}}\right)\overline{\mathbf{u}}_{\mathbf{0}} + \frac{1}{\overline{c}_{\mathbf{0}}^{\,2}}\overline{\mathbf{u}}_{\mathbf{0}}.\nabla\,\overline{\mathbf{u}}_{\mathbf{0}} - \frac{1}{\overline{\rho}_{\mathbf{0}}}\nabla\,\overline{\rho}_{\mathbf{0}}\,, \tag{4.44}$$

$$K_{\mathbf{0}}^2 = \frac{\omega^2}{\overline{c}_{\mathbf{0}}^{\,2}} - i\omega\overline{\mathbf{u}}_{\mathbf{0}}.\nabla\frac{1}{\overline{c}_{\mathbf{0}}^{\,2}}\,, \tag{4.45}$$

and where $\mathbf{M_0} = \overline{\mathbf{u}}_{\mathbf{0}}/\,\overline{c}_{\mathbf{0}}$.

Similarly, the velocity potential at a neighbouring point, $\mathbf{m}$, in the computational lattice, where $\mathbf{m} = 1, 2, .., M$, is given as

$$\boldsymbol{\phi}_{\mathbf{m}} = \sum_{n=1}^{N} \gamma_n \exp\left[-iq\left(\mathbf{d}.\mathbf{x_m}\right)\right] = \mathbf{H}\boldsymbol{\gamma}\,. \tag{4.46}$$

If $\mathbf{H}^+$ is the pseudo-inverse of $\mathbf{H}$ then

$$\boldsymbol{\gamma} = \mathbf{H}^+\boldsymbol{\phi}_{\mathbf{m}}\,, \tag{4.47}$$

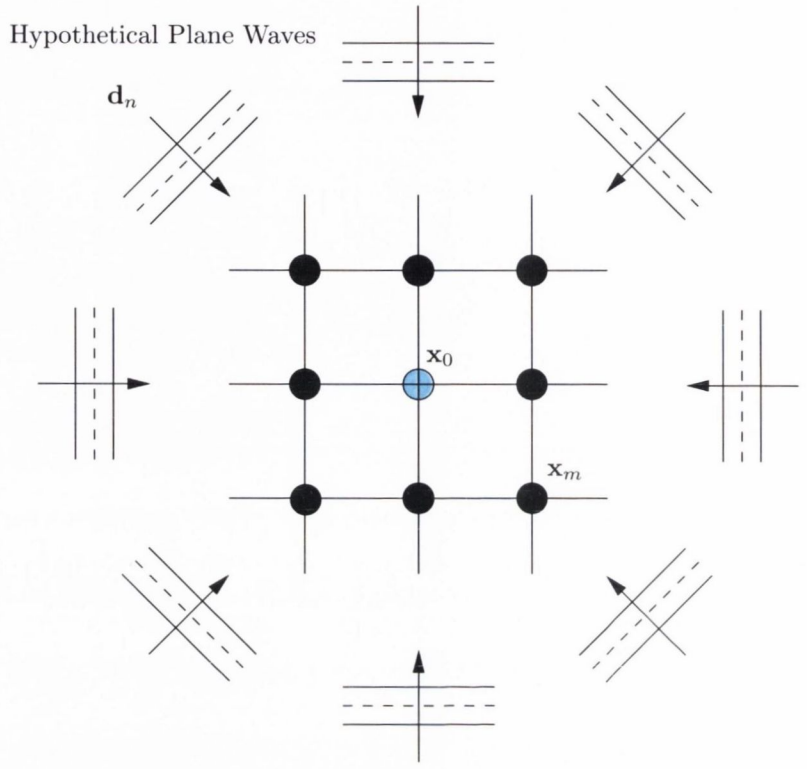

Figure 4.4: Wave expansion discretisation stencil.

and substituting this back into equation (A.12) leads to

$$\phi_{\mathbf{0}} - \mathbf{h}\mathbf{H}^{+}\boldsymbol{\phi}_{\mathbf{m}} = 0\,. \tag{4.48}$$

If the he local stiffness vector for a computational lattice is $\kappa_{\mathbf{0}} = -\mathbf{h}\mathbf{H}^{+}$, then

$$\phi_{\mathbf{0}} + \kappa_{\mathbf{0}}\boldsymbol{\phi}_{\mathbf{m}} = 0\,, \tag{4.49}$$

which may be rewritten as

$$\left\{ \begin{array}{cc} 1 & \kappa_{\mathbf{0}} \end{array} \right\} \left\{ \begin{array}{c} \phi_{\mathbf{0}} \\ \boldsymbol{\phi}_{\mathbf{m}} \end{array} \right\} = 0\,. \tag{4.50}$$

For the total computational domain, with a source vector, $\mathbf{f}$, added to the right-hand-side and where $\boldsymbol{\kappa}$ is the overall stiffness matrix, a linear system of equations may be defined of the form

$$\boldsymbol{\kappa}\boldsymbol{\phi} = \mathbf{f}\,. \tag{4.51}$$

This may, with the addition of appropriate boundary conditions, be solved for $\boldsymbol{\phi}$, a vector containing the velocity potential at each point in the overall computational lattice. Once the velocity potential field has been determined, the acoustics pressure field may be determined through equation (4.41).

4.5.2 Implementation of WEM Boundary Conditions

The implementation of boundary conditions for this numerical method may implemented, as shown by Ruiz [74], as follows

Dirichlet

Dirichlet boundary conditions may be implemented in the WEM by simply constraining the appropriate entries in the overall stiffness matrix.

Natural Radiation

Natural radiation boundary conditions can be imposed by only selecting the plane waves travelling out of the domain when assembling the stiffness matrix for points on the boundary. Equation (A.16) for natural radiation boundary points becomes

$$\phi_{\mathbf{0}} + \kappa_{\mathbf{0},natrad}\, \boldsymbol{\phi}_{\mathbf{m}} = 0\,. \tag{4.52}$$

Neumann

To impose the normal velocity of a boundary point as

$$\frac{\partial \phi_B}{\partial \mathbf{n}} = \mathbf{v}_B\,, \tag{4.53}$$

where $\mathbf{n}$ is a unit vector normal to the boundary, equation (A.13) is augmented by each Neumann boundary point, so that

$$\begin{Bmatrix} \boldsymbol{\phi}_{\mathbf{m}} \\ \mathbf{v}_B \\ \vdots \end{Bmatrix} = \begin{bmatrix} \mathbf{H} \\ \partial \mathbf{h}_B / \partial \mathbf{n}_m \\ \vdots \end{bmatrix} \{\boldsymbol{\gamma}\} = \mathbf{H}_{aug} \boldsymbol{\gamma}\,. \tag{4.54}$$

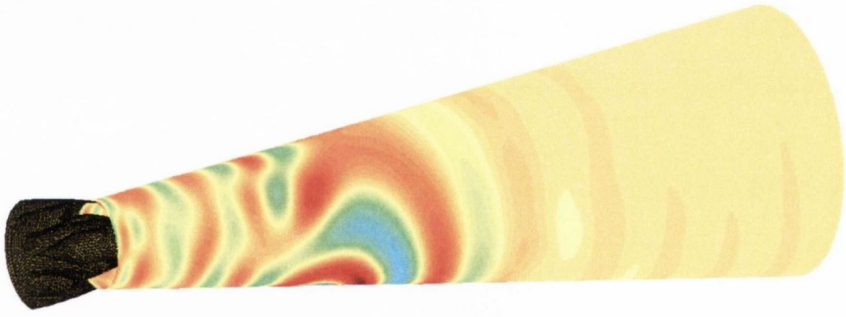

Figure 4.5: A Kirchhoff surface external to the jet flow.

Taking the pseudo-inverse of $\mathbf{H}_{aug}$

$$\gamma = \left[\mathbf{H}^{+}_{aug}\right] \left\{ \begin{array}{c} \phi_{\mathbf{m}} \\ \mathbf{v}_B \end{array} \right\}, \tag{4.55}$$

equation (A.15) may be partitioned, and so becomes

$$\phi_{\mathbf{0}} = \mathbf{h}H^{+}_{aug,L}\,\phi_{\mathbf{m}} + \mathbf{h}H^{+}_{aug,R}\,\mathbf{v}_B\,. \tag{4.56}$$

Using the WEM, a monopole source may be propagated through the jet flow. It is only necessary to numerically propagate the sound to beyond the inhomogeneous flow of the jet, as a Kirchhoff surface may then be defined outside the jet and the sound propagated to the far-field using the Helmholtz-Kirchhoff integral equation.

A comparison was made using this wave expansion method for the benchmark case presented by Bailly and Juvé [6] for the radiation of a point source in a sheared mean flow and was found agree very well as can seen in figure 4.6.

4.6 Discussion

It is intended that the source distribution may be easily integrated into alternative propagation codes, such as a BEM. Adaptation of such codes to include directional sources is not always desirable. This can this overcome, though, by replacing each directional source with a multipole, centred on the same location, which has been fitted to give the same directivity.

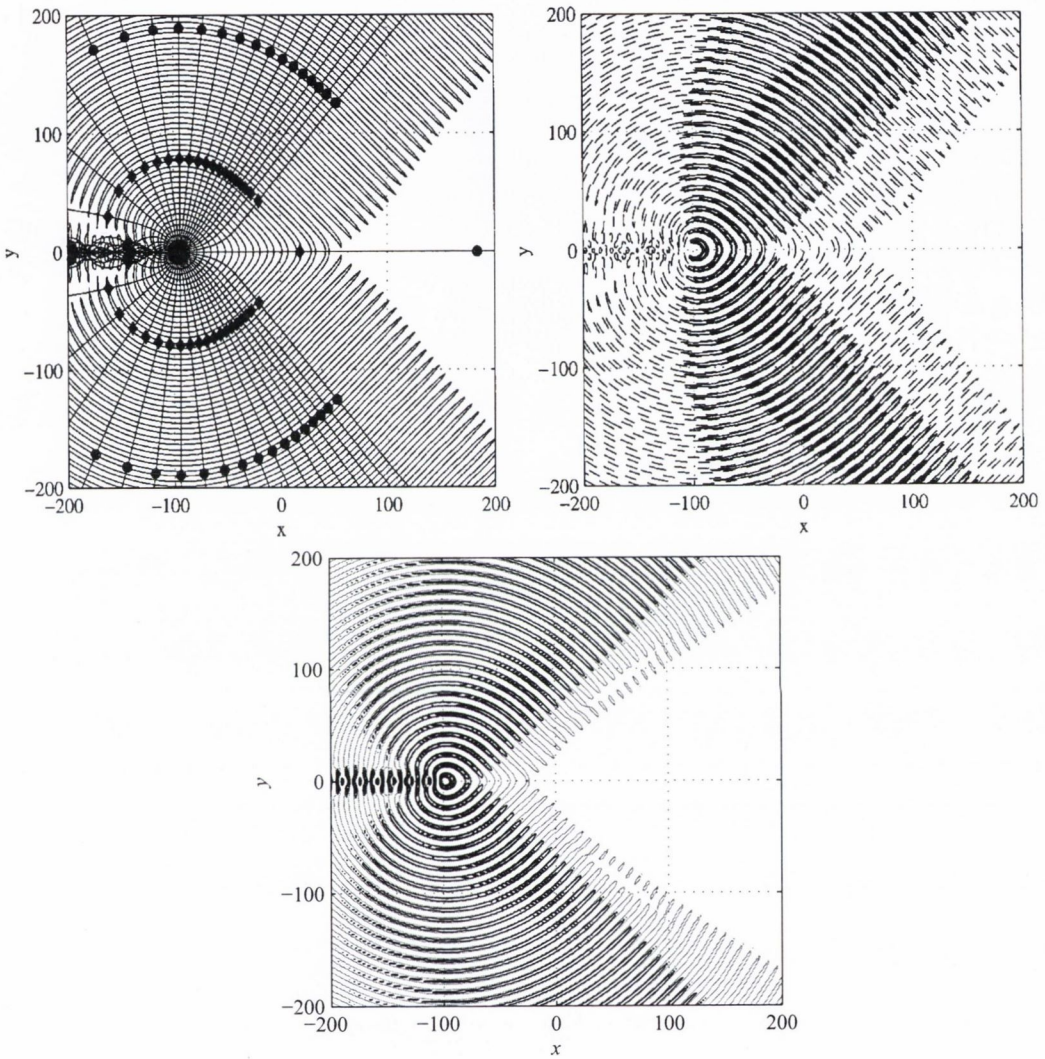

Figure 4.6: Benchmark comparison of the radiation of a point source in a sheared flow for the configuration described in reference [6]: Bailly and Juvé's ray-tracing solution (top-left) and LEE computation (top-right), and the wave expansion method, WEM, computation (bottom).

In order to use this modelling methodology, it has to be assumed that the shielding surface is sufficiently far removed from the turbulent source to maintain the validity of the presented jet model. This may not be the case.

Chapter 5

Jet Noise Shielding Assessment

Jet noise predictions for the NACRE jet have been made using the approach outlined in chapter 4 and are presented in this chapter. These predictions are compared with the available test data, the Lighthill-Ribner and Tam-Auriault models, and also, the jet noise predictions of NACRE partners, which were computed using similar jet noise shielding prediction approaches.

5.1 Jet Test Setup

The noise from a scaled coaxial jet, in *isolated* and *shielded* configurations, was measured as part of the NACRE wind-tunnel test programme carried out by ONERA at its CEPRA19 facility in Saclay, France in 2007 [31]. The anechoic wind-tunnel at CEPRA19 has a convergent nozzle of two metres in diameter, as can be seen in figure 5.1, and has maximum velocity of $130m/s$. The nozzle's primary and secondary flow capacities are determined by the compressed air supply, which is limited to a maximum mass flow rate of $12kg/s$, pressure of $8bar$ and temperature of $500K$. The primary flow may be heated by a propane burner to temperatures in the range of $500K < T < 1150K$.

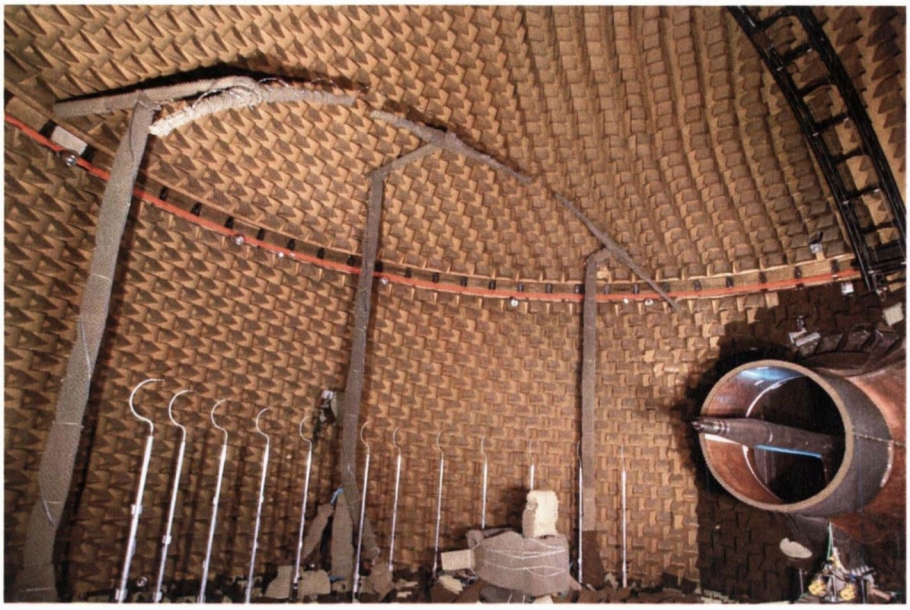

Figure 5.1: View of the isolated BPR9 nozzle in the anechoic wind-tunnel at CEPRA19. The flyover and sideline microphone arrays are visible.

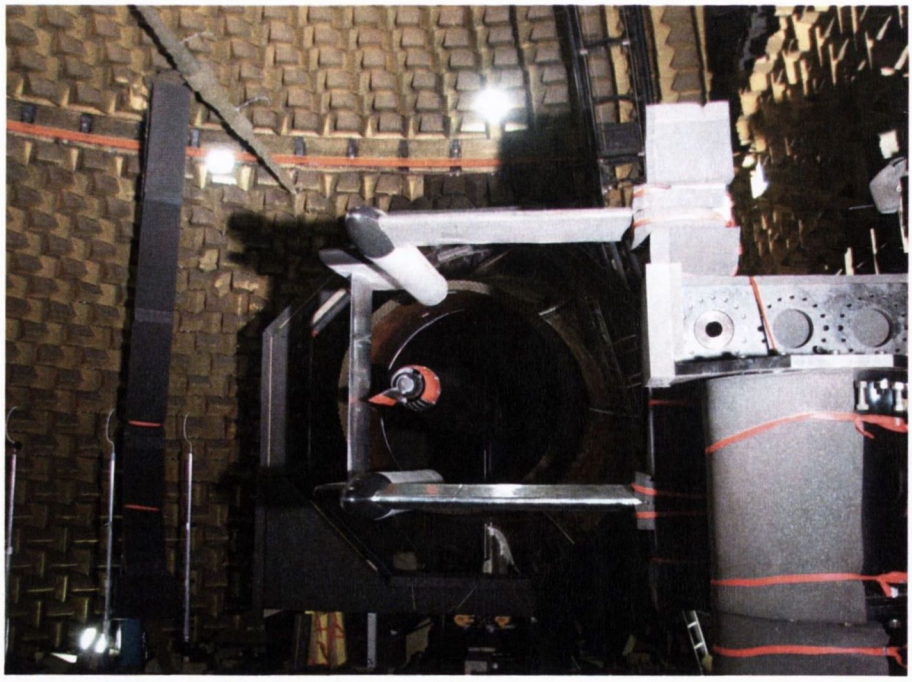

Figure 5.2: View of the BPR9 nozzle installed over the EUROPIV model in the CEPRA19 facility.

The coaxial jet noise simulator is a high bypass ratio ($BPR = 9$) nozzle with a secondary exhaust diameter of $D = 0.264m$ and includes a central plug and part of the aircraft mounting pylon. To assess the shielding of the jet noise, the EUROPIV model was installed in a position representative of a possible airframe shielding configuration, such as NACRE's "Pro-Green" concept. This model is a 2D high-lift wing with a chord of $0.5m$, a span of $1.5m$, and is without a sweep angle. The model also includes side-plates and side-beams as part of its wind-tunnel mounting, as can be seen in figure 5.2.

Acoustic measurements were acquired in the *flyover* and *sideline* azimuthal planes using two arcs of microphones[1], centred on the intersection of the secondary exit plane and the jet axis. The radius of both arcs was $6m$ and microphones were distributed at 10° intervals between 30° and 140° from the downstream jet axis, as illustrated in figure 5.3. The plane of the flyover arc bisected the shield and the sideline arc was at 56° to the flyover plane.

Far-field measurements were taken with the pylon at two different azimuthal angles – in the flyover plane at 0°, as is visible in figure 5.4, and at −45° (101° to the sideline microphone arc), as is visible in figure 5.2. The rotation of the pylon was found to have a very weak effect on the far-field acoustic measurements, for all the test conditions examined.

In order to assess the axial location of the jet noise generation, measurements were also taken (for the isolated case only) using a linear array of 43 microphones mounted parallel to the jet axis. The axial source position was determined by ONERA using a beam-forming method.

[1]Brüel & Kjær 1/4″ type 4139 microphones.

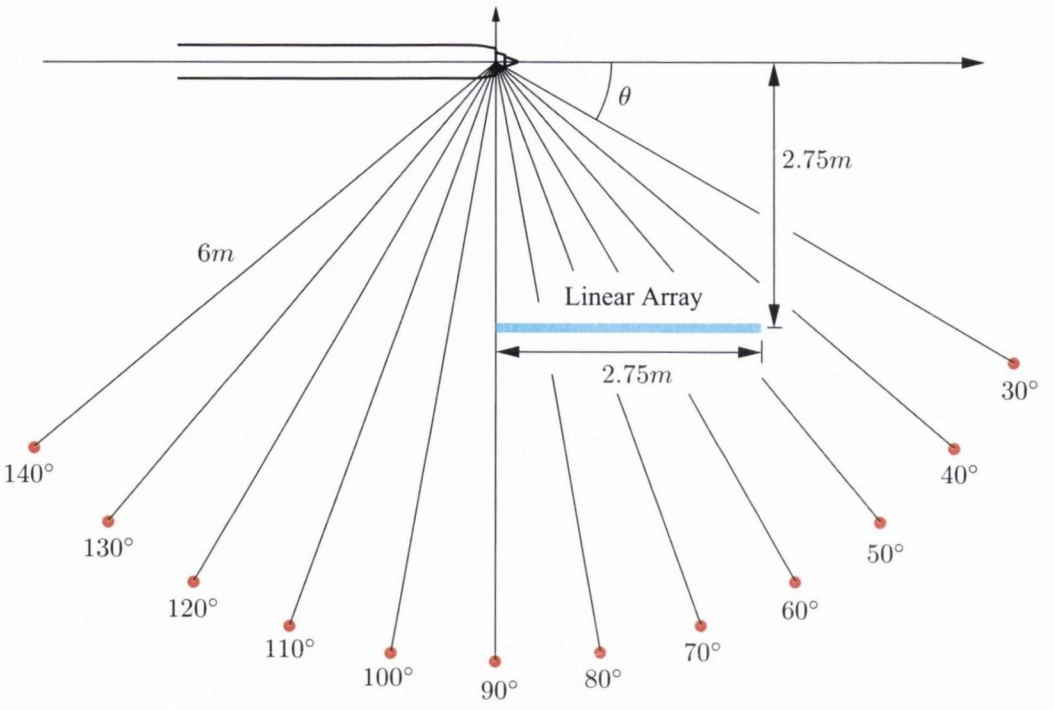

Figure 5.3: Location of far-field microphone arc and linear microphone array.

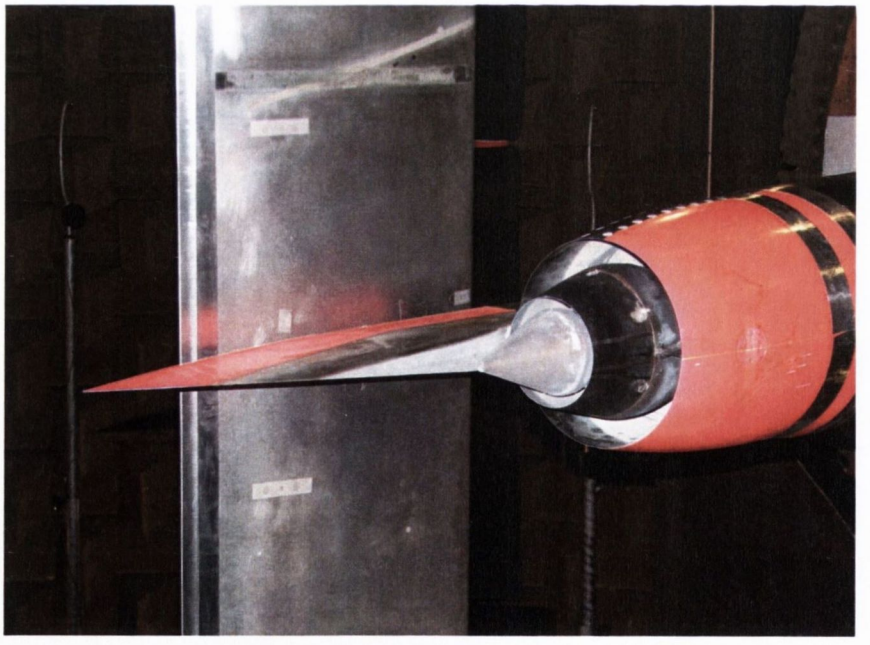

Figure 5.4: View of the BPR9 nozzle installed over the EUROPIV model with the pylon oriented in the flyover plane.

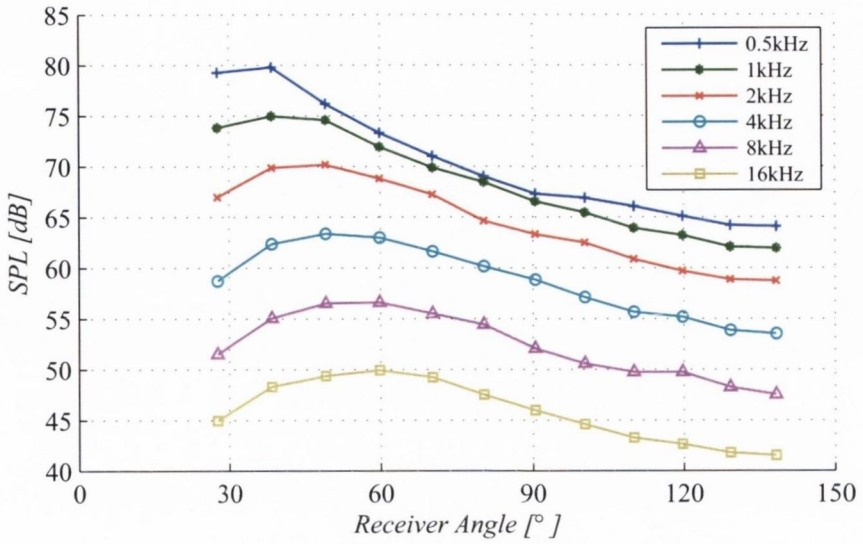

Figure 5.5: Isolated sound pressure levels measured at the flyover arc.

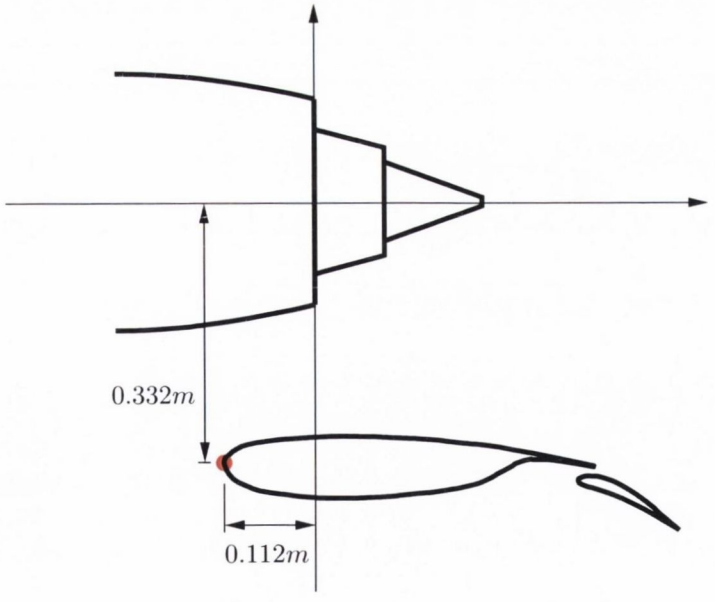

Figure 5.6: Location of EUROPIV shield relative to the jet nozzle.

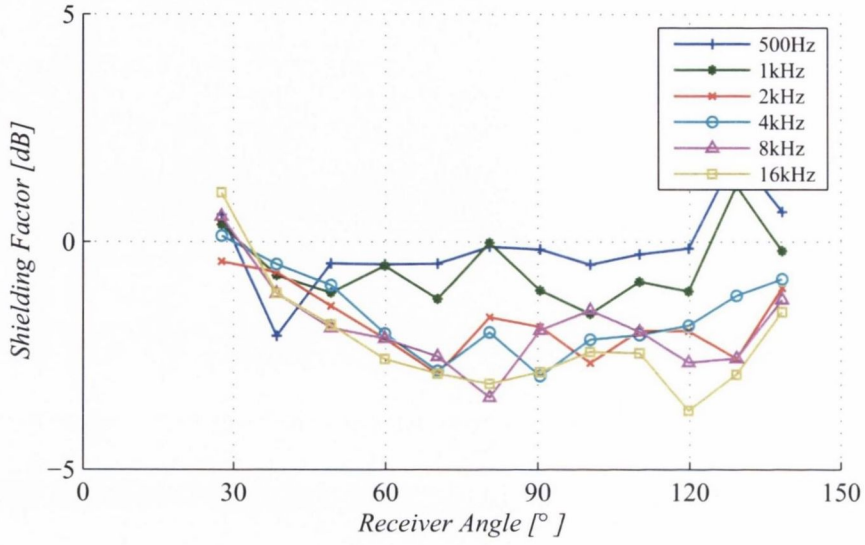

Figure 5.7: Shielding factor measured at the flyover arc.

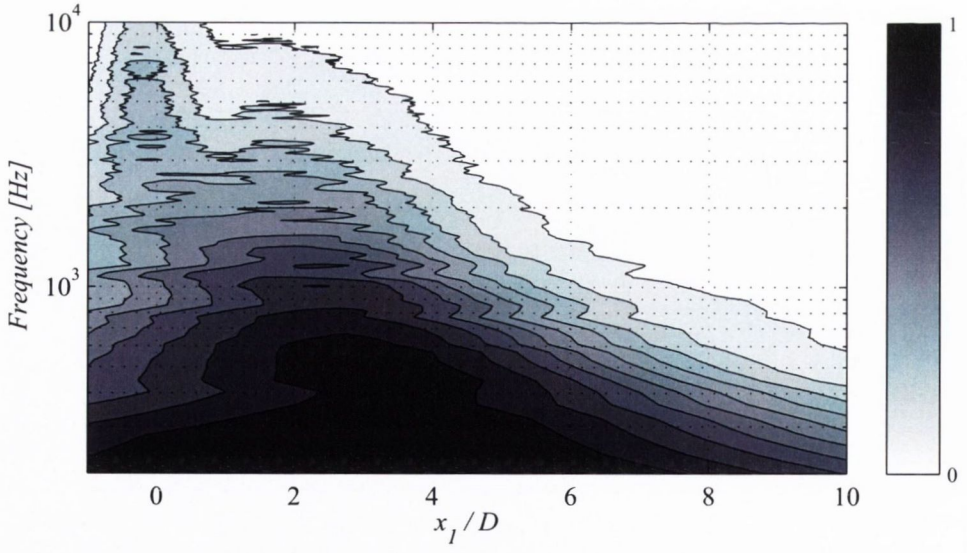

Figure 5.8: Normalised beam-forming axial source localisation from the linear array data.

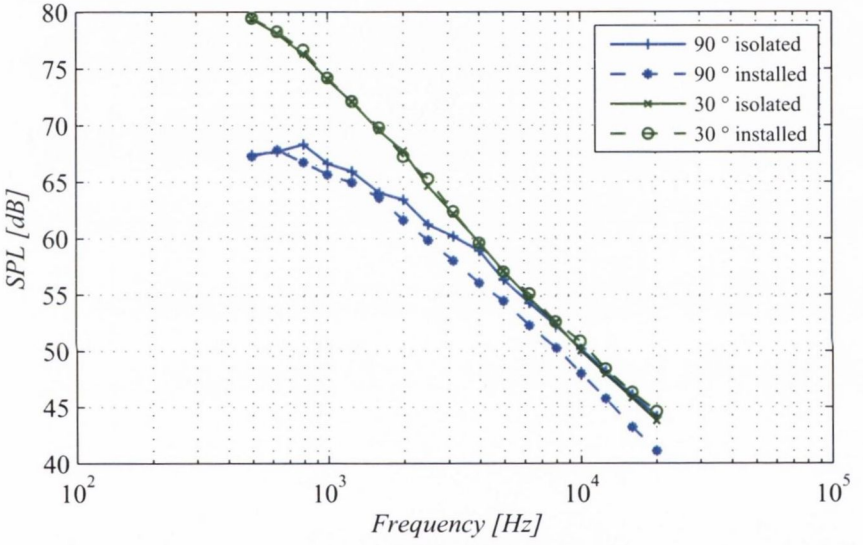

Figure 5.9: Noise spectrum measured at the flyover arc.

5.2 Jet RANS Computations

A number of flow conditions were measured as part of the NACRE wind-tunnel test programme, however, the flow case shown in table 5.1 was selected by the NACRE partners for numerical analyses, and has, therefore, been the focus of this present work.

Velocity external $[m/s]$	16.5
Pressure external $[Pa]$	99136
Temperature external $[^\circ K]$	301.2
Primary pressure ratio	1.237
Primary total temperature $[^\circ K]$	799
Primary exit velocity $[m/s]$	277.82
Primary exit Mach number	0.50
Secondary pressure ratio	1.502
Secondary total temperature $[^\circ K]$	337
Secondary exit velocity $[m/s]$	260.62
Secondary exit Mach number	0.75

Table 5.1: NACRE jet flow conditions.

An axisymmetric $\kappa - \epsilon$ RANS solution was computed for these flow conditions by Dassault Aviation using their in-house code. As the numerical flow simulations are axisymmetric, the pylon, which is present in the test setup, has been neglected from the present numerical computations.

The exit velocities from the two nozzles are quite closely matched at this this set of flow conditions, and so, the shear-layer between the primary and secondary flows does not play a significant role in jet noise production for this present jet. The turbulent kinetic energy, in figure 5.10 indicates that the mixing shear-layer between the secondary jet flow and the surrounding flow is the main region of jet noise production.

Although the surrounding flow in the wind-tunnel was nominally stationary,

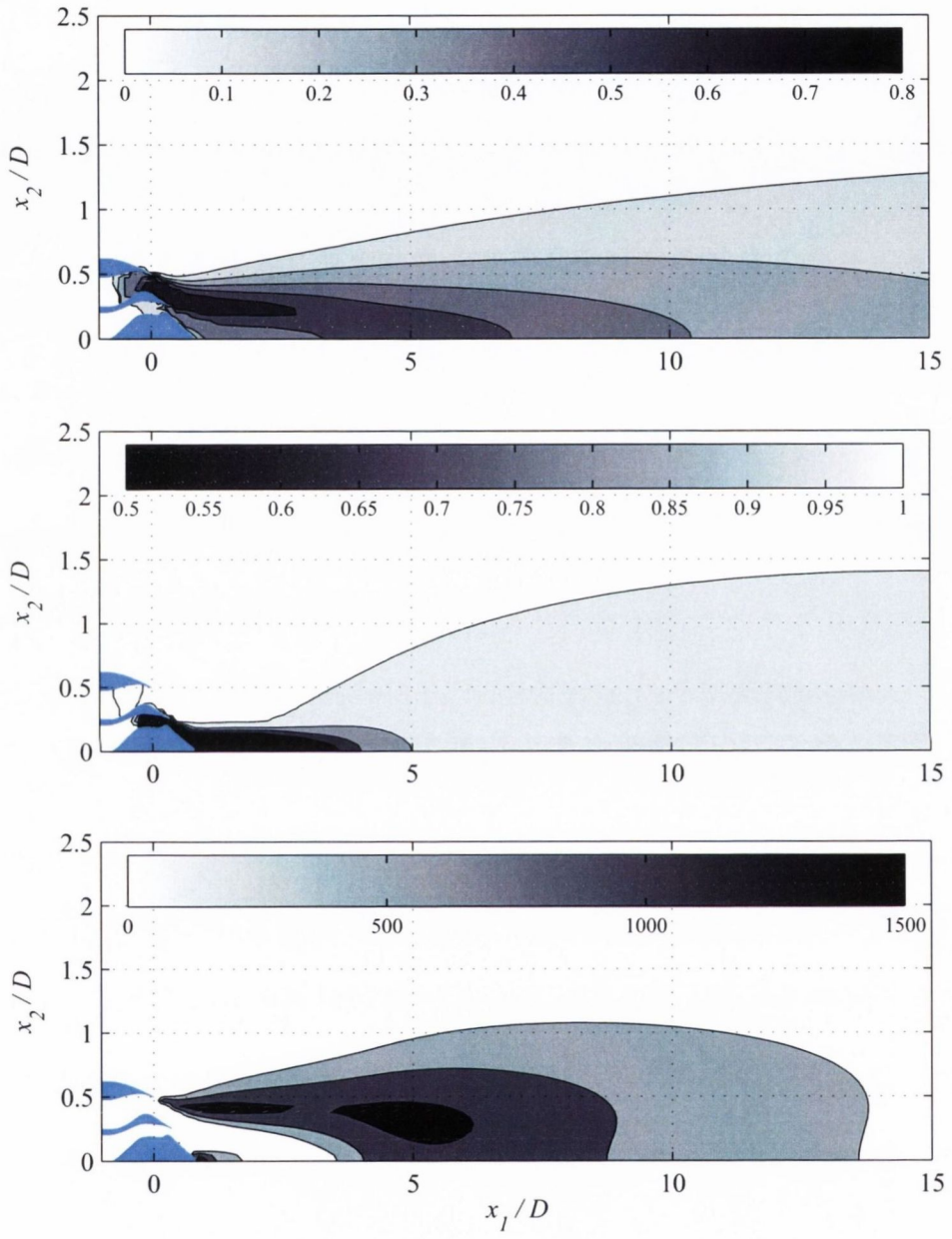

Figure 5.10: Dassault's axisymmetric $\kappa - \epsilon$ RANS solution: Mach number (top), density $[kg/m^3]$ (middle) and turbulent kinetic energy $[m^2/s^2]$ (bottom). Note that the axes scales are not the same.

as can seen in table 5.1, the external flow velocity was in fact $16.5m/s$

5.3 Full Source Model Predictions

The source reduction scheme, described in section 4.3 was not included at this point so as to avoid possible errors being introduced through the reduction procedure (the reduction schemes are examined in section 5.5). The Green's function was computed to consider the full spatial extent of the jet source volume and so $\mathbf{r} = \mathbf{x} - \mathbf{x_s}$. As there is one source at each element of the RANS mesh, this jet noise source distribution is referred to as the *full-3D* source.

5.3.1 Jet Model Calibration

A critical factor in the effectiveness of acoustic shielding is the relative locations of the source, shield, and receiver. Given that the location of the shield and receiver are known in the jet noise shielding problem, it is important to identify the location of the jet noise sources for a given frequency. In the jet noise models presented in this thesis – the Lighthill-Ribner (LR) model (in section 3.2), the Tam-Auriault (TA) model (in section 3.3), and the model presented in chapter 4 (which is refered to as Model$_C$) – the characteristic length scale, l_t, and time scale, τ_t of the turbulence, determine the location of the jet noise source. As these variables must be estimated from the RANS solution, evaluating the model scaling constants, c_l and c_t, is critical to jet noise shielding predictions.

Jet Noise Model	c_l	c_t
Lighthill-Ribner (LR)	0.3	0.8
Tam-Auriault (TA)	0.3	0.3
Model$_C$	0.3	0.3

Table 5.2: Calibrated Model constant values.

The axial source location of the NACRE jet was evaluated using a beam-forming method with the data from the linear microphone array [31]. The beam-

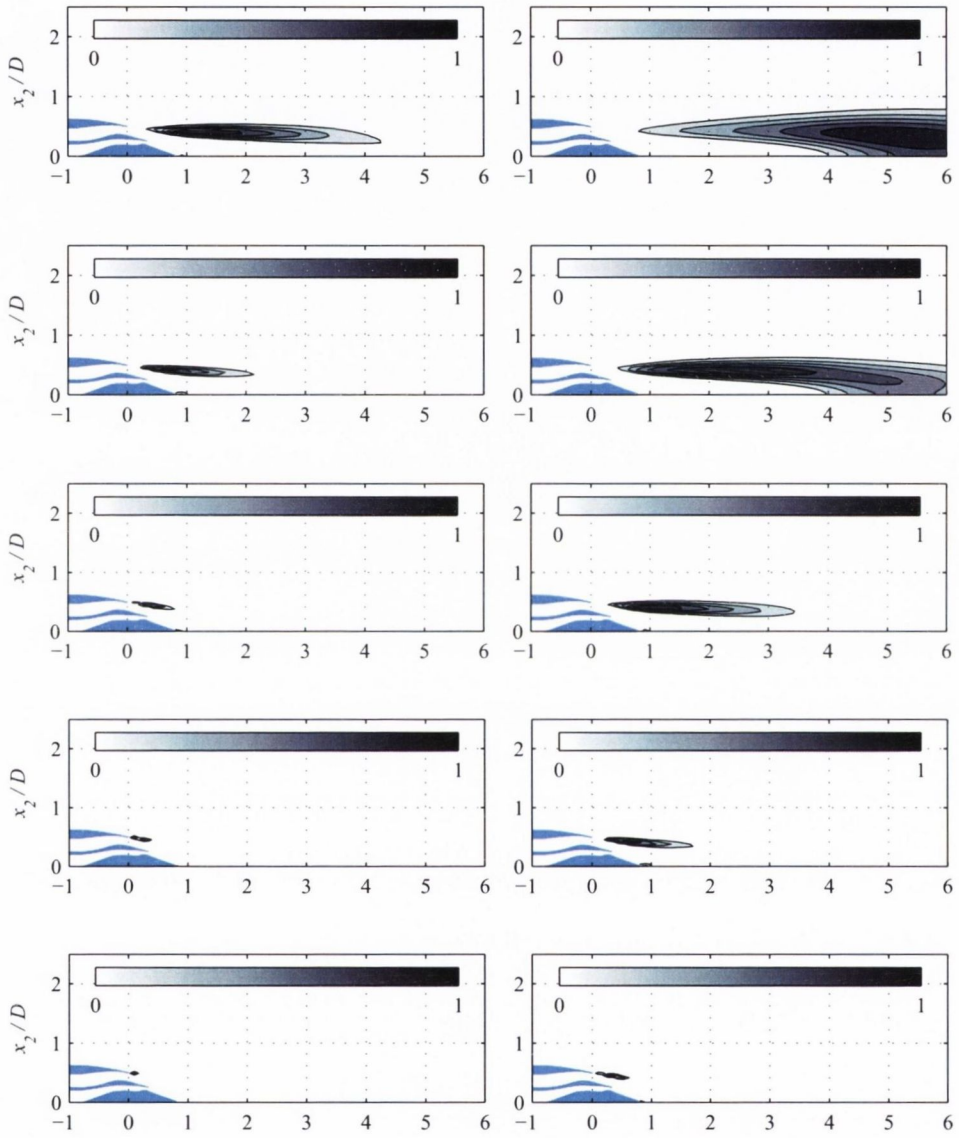

Figure 5.11: Axial calibration: normalised source power distribution from Model$_C$ with uncalibrated (left) and calibrated (right) model constants, at $0.5kHz$, $1kHz$, $2kHz$, $4kHz$ and $8kHz$ (from top to bottom).

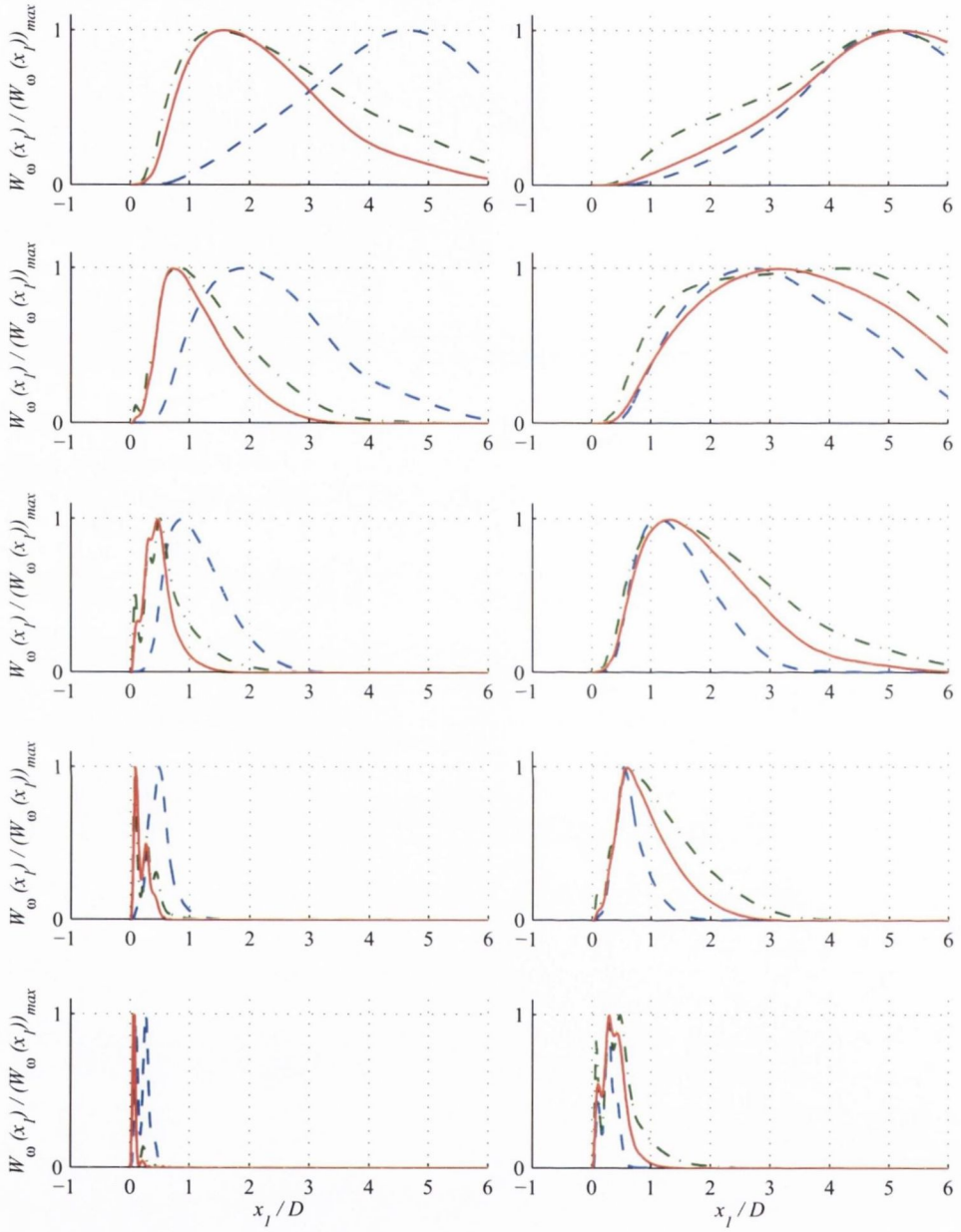

Figure 5.12: Axial calibration: normalised axial source power distribution from the LR model (blue $--$), the TA model (green $-\cdot$) and Model$_C$ (red $-$), with uncalibrated (left) and calibrated (right) model constants, at $0.5kHz$. $1kHz$, $2kHz$, $4kHz$ and $8kHz$ (from top to bottom).

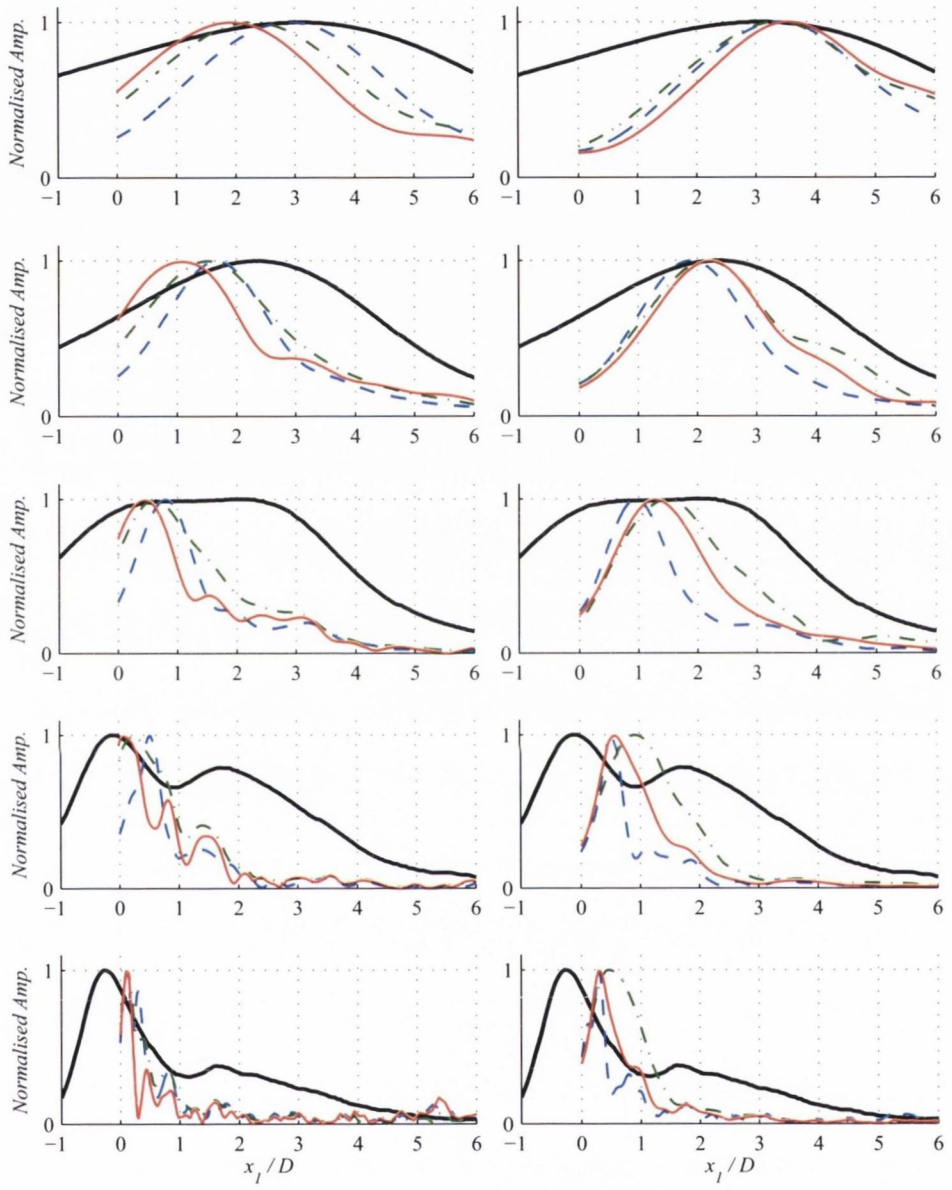

Figure 5.13: Beam-forming axial source location: NACRE test data (bold black $-$), LR model (blue $--$), TA model (green $-\cdot$) and Model$_C$ (red $-$), with uncalibrated (left) and calibrated (right) model constants, at $0.5kHz$. $1kHz$, $2kHz$, $4kHz$ and $8kHz$ (from top to bottom).

forming method is not a very rigorous approach for determining the actual location of an acoustic source as the solution is non-unique. A focus position must be assumed, which in this case was along the jet axis. In reality, the jet noise near the nozzle exit is generated in an annulus about a *cone of silence*. Additionally, the evaluated location is somewhat sensitive to the position of the receiver array. Despite these shortcomings, it is still more appropriate to determine the model constants using this approximate near-field information rather than far-field measurements.

The model constants have, therefore, been determined so as to best-fit the beam-form identified source location, by replicating the beam-forming procedure [77] using model generated values at the linear receiver positions. A fitness criteria was defined as the distance between the weighted average axial locations, which was minimised by searching c_l and c_t values were searched between 0 and 1. Table 5.2 shows the values of these constants determined for the three models.

Figure 5.11 presents the source power distribution for Model$_C$, with uncalibrated ($c_l = c_t = 1$) and calibrated results shown. The source power was evaluated by integrating the elemental spectral density over a sphere of far-field receivers. Integrating again over radial and azimuthal source positions gives the axial source power distribution, shown in figure 5.12 for the three models. A shift downstream of the source location is evident, particularly for the TA model and Model$_C$, and it may be observed that the calibrated locations of the three models agree well, as expected.

Figure 5.13 shows the corresponding beam-forming amplitudes of this calibration. A number of features are noticeable here:

- The actual (figure 5.12) and apparent (figure 5.13) axial locations of the model sources do not agree. This is most likely due to the omnidirectional weighting used in the beam-forming method (as was used in the ONERA's beam-forming of the NACRE data). It remains far from certain that the model source locations match the real location of the jet noise sources.

- The NACRE distribution is much broader than that from the model sources. Although this may be due to a difference between measured and artificial

positioning, it may also be that the models do not capture the actual extent of the source region.

- The NACRE result shows the source location upstream of the nozzle exit at high frequencies. This, again, is probably due to beam-forming inaccuracies, although that said, it can be observed that the peak location remains downstream of the exit for the model sources (which can not be upstream of the exit by definition). This raises the possibility that sources may be present upstream of the nozzle in the NACRE tests.

The presented source location calibration is not intended to be definitive (and, indeed, given the limitations of beam-forming, it can not be). Instead, the model source locations have been calibrated to highlight the influence of source location on shielding predictions and to enable a better comparison between the models and NACRE data. It also illustrates some of the shortcomings of these RANS dependent jet models.

5.3.2 Isolated Model Predictions

Figure 5.14 shows a comparison of the far-field SPL for the isolated configuration predicted by the three models with the model constants set to unity. With the exception of the lowest frequency predicted, Model$_C$ gives the best agreement with the acquired data. The TA model consistently under-predicts the directivity, whilst the opposite is true of the LR model. As all the models do not include refraction in the propagation of the sources, they all fail to predict the drop-off in SPL at receiver angles near the jet axis.

Calibrated model constants have been used in the predictions shown in figure 5.15, and so the sources are now located at (roughly) the same axial point in this comparison – an axial location that, it can be claimed, agrees with the measured jet. This also means that local input values, such as density and Mach number, are the same. The difference in far-field directivity predictions, due to the change in the model constants, is very small, with a slight change at low frequencies.

Figure 5.16 shows how the jet model spectra are altered by the model con-

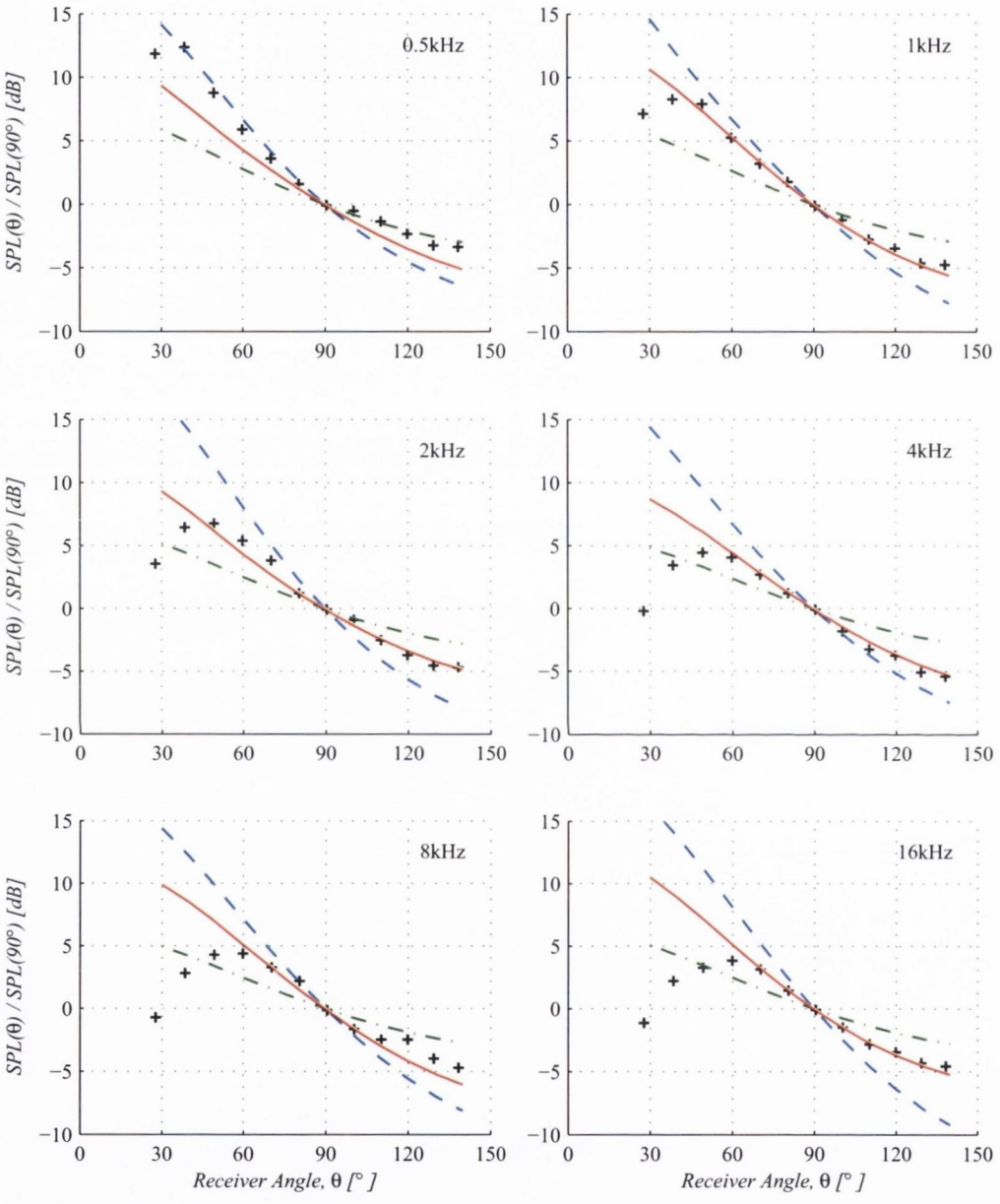

Figure 5.14: Jet models with uncalibrated constants: isolated far-field normalised SPL $[dB]$ directivity from NACRE test data (black +), LR model (blue $--$), TA model (green $-\cdot$) and Model$_C$ (red $-$).

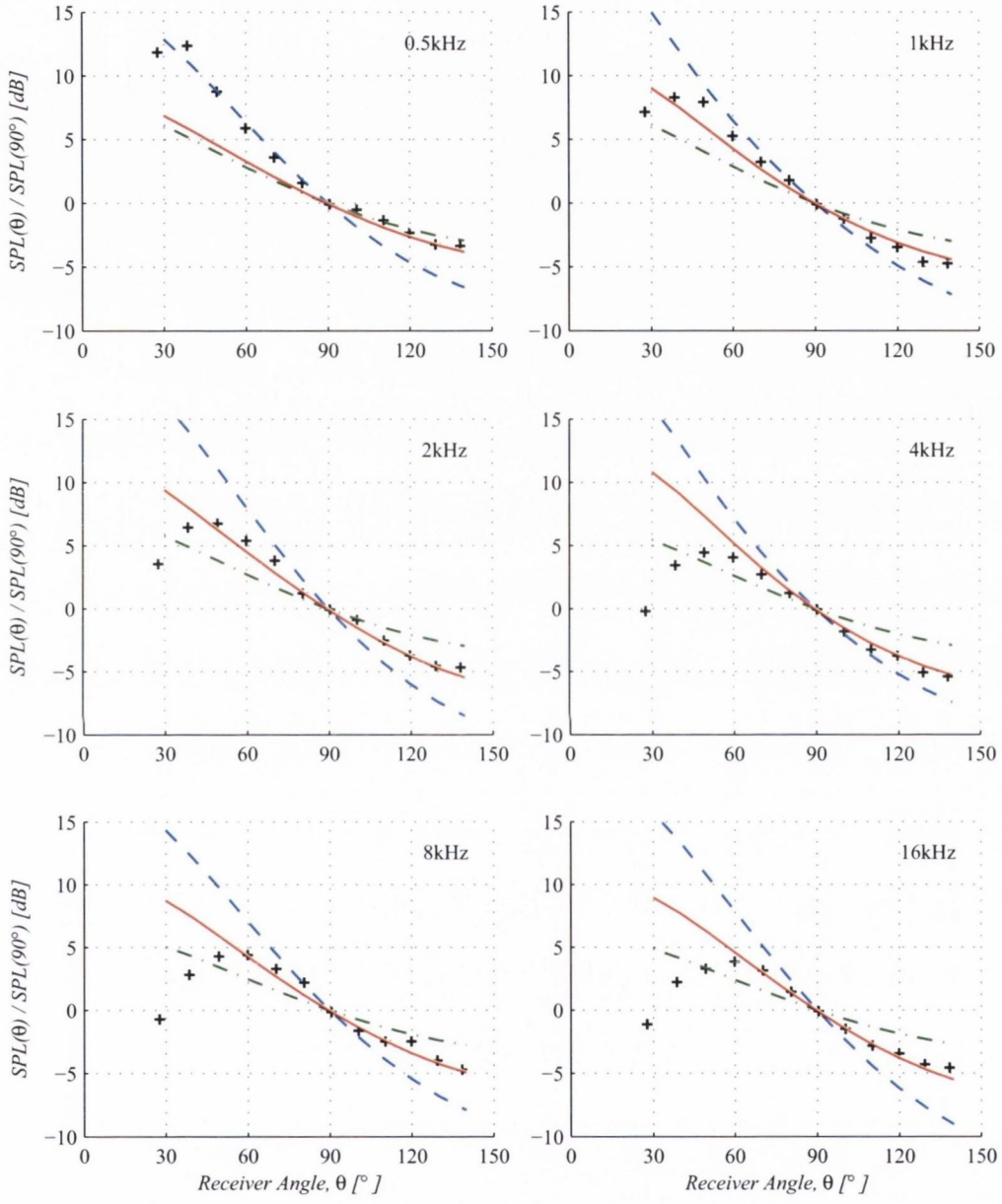

Figure 5.15: Jet models with calibrated constants: isolated far-field normalised SPL $[dB]$ directivity from NACRE test data (black +), LR model (blue $--$), TA model (green $-\cdot$) and Model$_C$ (red $-$).

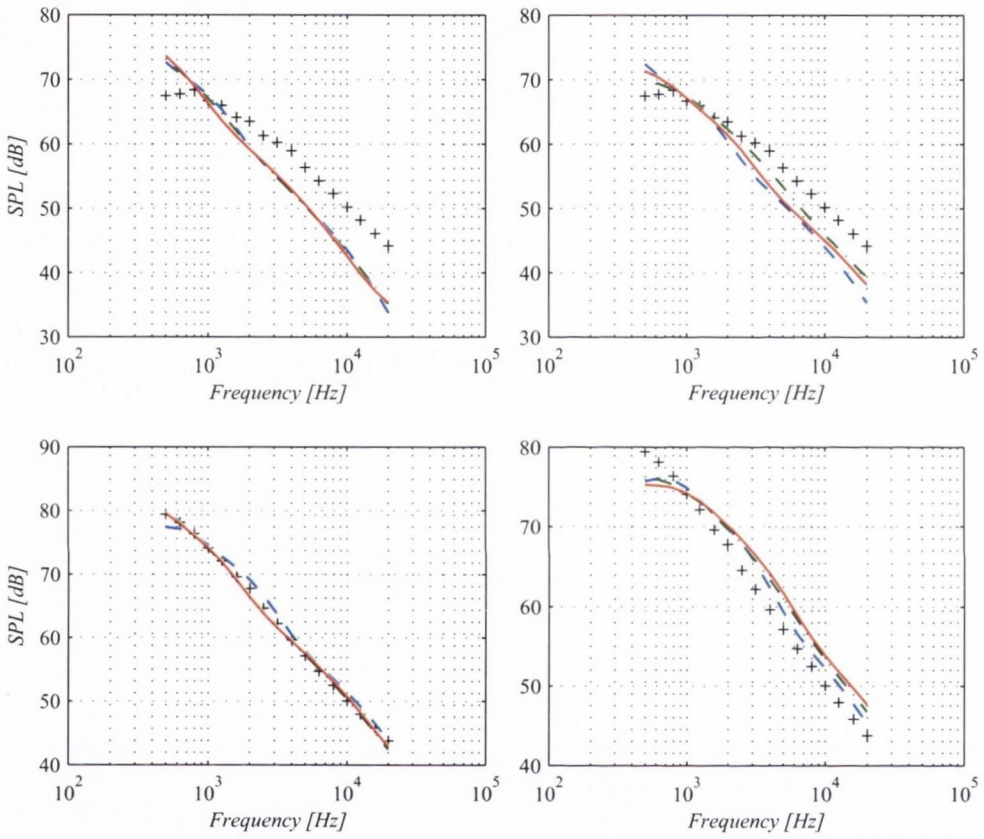

Figure 5.16: Noise spectra: NACRE test data (black +), LR model (blue $--$), TA model (green $-\cdot$) and Model$_C$ (red $-$), with uncalibrated (left) and calibrated (right) model constants, at 90° (top) and 30° (bottom).

stants. At 90° there is a slight improvement. Tam and Auriault's method was originally focused on improving the far-field spectra at 90° and indeed it does appear to be the most responsive here. At 30° the use of the model constants does not improve the predicted spectra. Tam and Auriault argued the use of such constants is justified because they are modelling the small-scale jet noise source – or a proportion of the total jet noise production. As the contribution from the different jet noise components varies with receiver angle, it is questionable to use the same constant irrespective of observation angle. Constants could be evaluated which are frequency, spatially and directionally dependent. However, given their limited physical meaning, it may be more fruitful to direct future development into enhancing the space-time models (for example, frequency dependent length- and time-scales) and flow models (perhaps using LES).

More importantly, the evaluation of the model constants to best-fit the spectra at 90° (as is common practice) is inadvisable, particularly for shielding predictions, as small improvements at 90° may be countered by disimprovements at other angles and significant shifts in the source location. The use of far-field evaluated model constants should, therefore, not be taken lightly.

Although, it may not be concluded that Model$_C$ offers an improved far-field prediction model, as this comparison is very limited, it may be said that, for the present NACRE data and RANS solution, Model$_C$ is the best choice for the present shielding prediction assessment.

5.3.3 Source Location Effect

As the calibration of model constants, c_l and c_t, changes the location of the modelled jet source, a comparison of the predicted (isolated and shielded) far-field values was performed between calibrated ($c_l = c_t = 0.3$) and uncalibrated ($c_l = c_t = 1$) Model$_C$ sources. The sources investigated, in this section, are defined with one source per element of the RANS solution (as described in section 4.2), and the source region has been limited to elements where $F_W(\mathbf{x_s}) \geq$ 1e-3 $(F_W(\mathbf{x_s}))_{max}$. As the RANS mesh is 2D, the sources have been rotated about the jet axis, and so, the element volume is $dV\, x_2\, d\phi$, where ϕ is the azimuthal angle.

Figure 5.17 shows the far-field SPL for the isolated configuration. The differences are relatively small, considering the large shift in axial position (as much as 4 diameters for the low frequency sources) and both sets of results match the data well. It could be claimed that far-field isolated predictions are relatively robust to variations in RANS input or source location, although this may be a little over-optimistic.

A note-worthy feature of the difference in directivity, resultant from the two different source locations, may be observed at $500Hz$. Although the sources have been moved downstream in the calibration, towards the lower angled receivers, this prediction shows a lower directivity than the uncalibrated sources, when the opposite might be expected. This is because at the downstream location, the sources convect at a slower Mach number and are, therefore, less directional – there is a trade-off between the source directionality and position. The implication of this is that, although c_l and c_t may be *tuned* for different jet models or different RANS solutions, jet noise predictions will still be heavily influenced by spatial variations in the RANS variables.

Figure 5.18 presents the shielding factor for the two source locations, predicted using the Fresnel-Kirchhoff method (FKM). The EUROPIV (foil and flap) was approximated as a single flat surface. Unfortunately, there is poor agreement between the predicted shielding factors and the measured NACRE levels. It will be shown in subsequent analyses that this disagreement between the predicted and

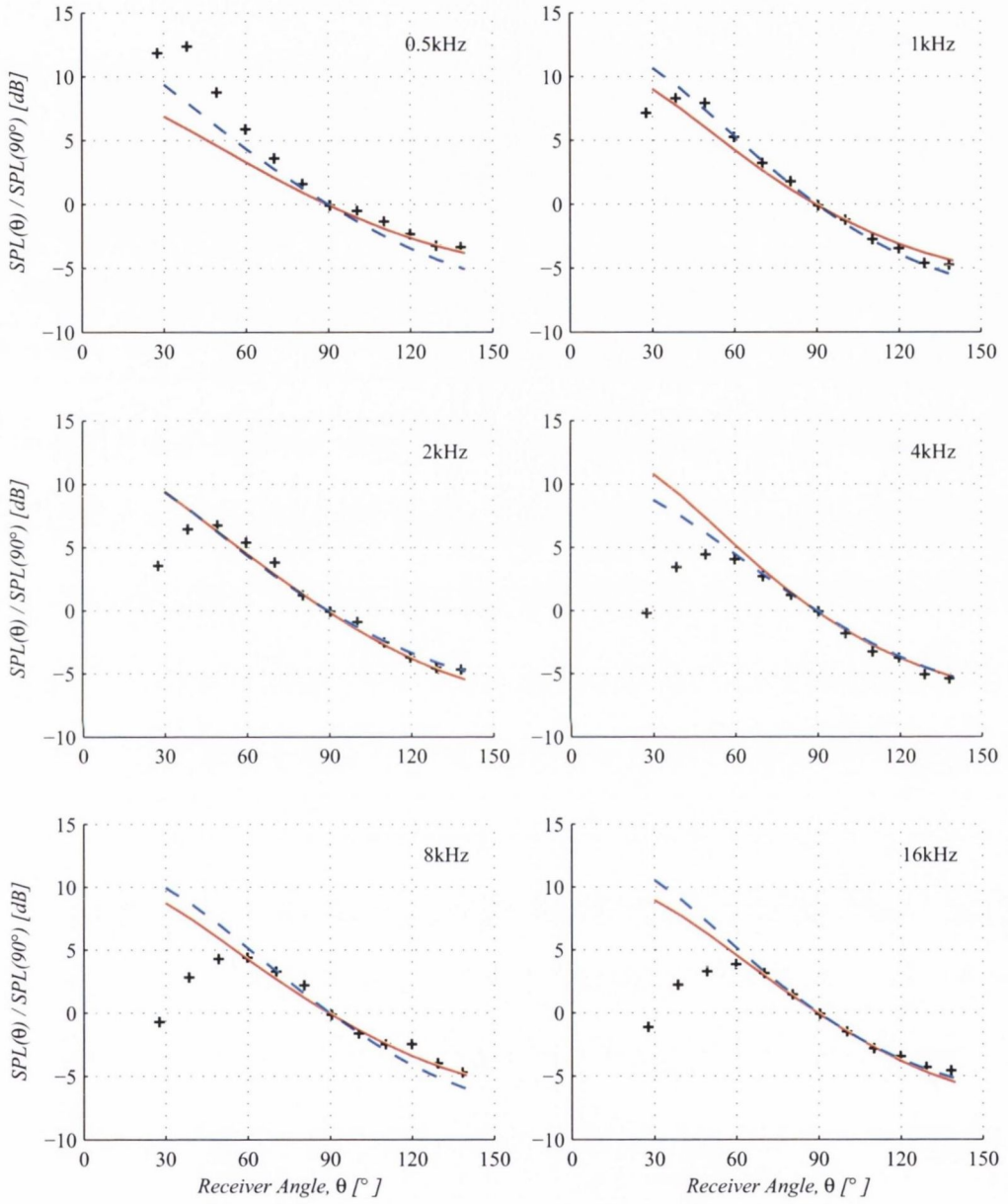

Figure 5.17: Axial source location: isolated normalised far-field SPL $[dB]$ directivity from NACRE test data (black +) and Model_C with uncalibrated (blue $--$) and calibrated (red $-$) model constants.

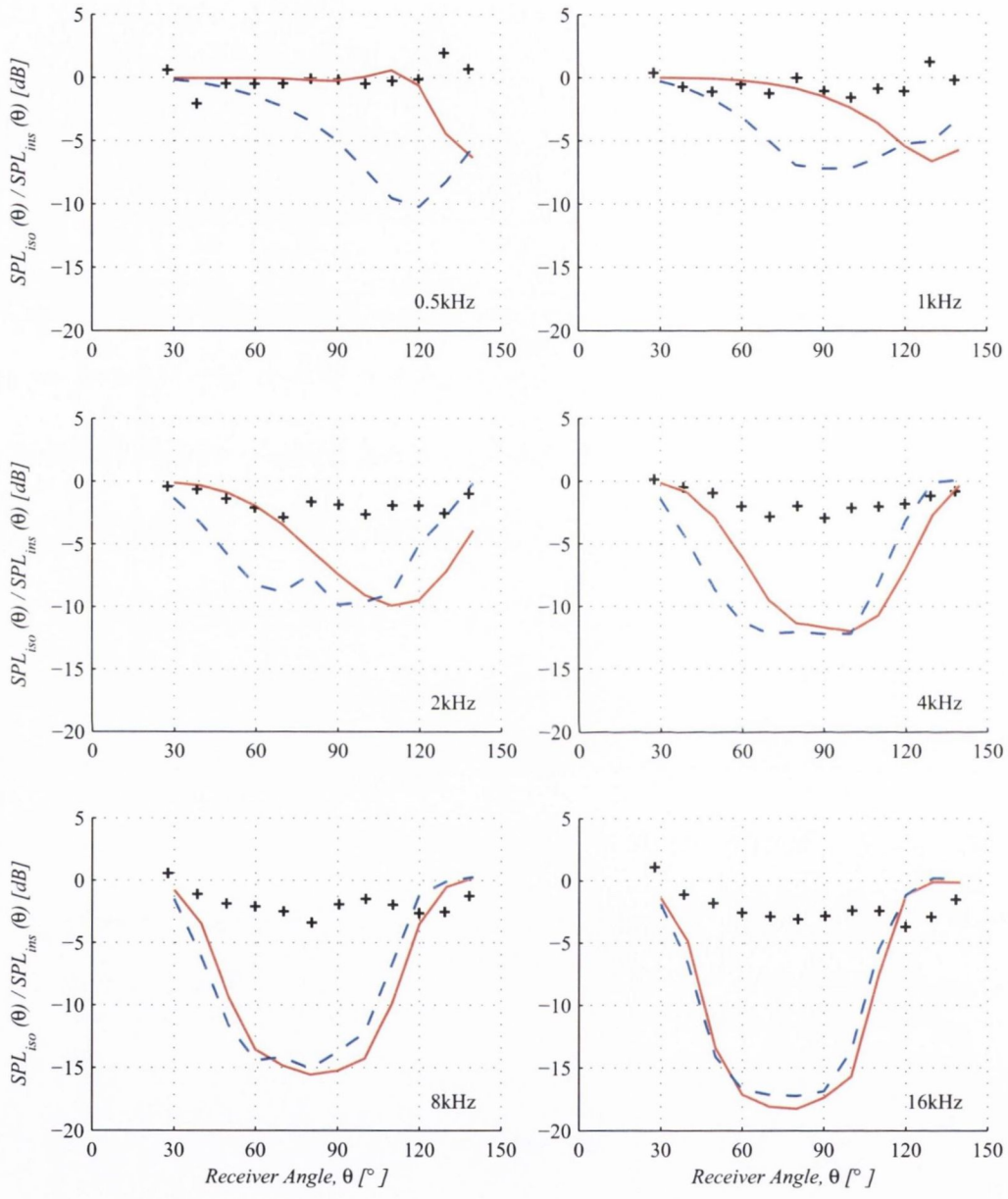

Figure 5.18: Axial source location: far-field shielding factor $[dB]$ directivity from NACRE test data (black +) and Model$_C$ with uncalibrated (blue $--$) and calibrated (red $-$) model constants.

measured shielding levels is observed throughout the prediction comparisons, of this and alternative methods, and a full discussion of the possible causes is reserved for chapter 6. However, some useful traits of the modelling methods may still be noted.

Figure 5.18 shows that the shift in source location has been accompanied by a complementary shift in shielding directivity, with peak levels remaining unchanged. It may also be observed (at $2kHz$ and $4kHz$) that there is a slight narrowing of the shielded region with the calibrated sources, due to the spreading of the source region (see figure 5.11), which accompanies the shift downstream. This result highlights the importance of accurate source positioning to shielding predicition, although, given the lack of agreement with the shielding factor data, it can not be established if the calibration of the axial source location with the beam-forming result was successful (or even appropriate). It is assumed, though, that the calibrated sources are valid, and the continued analyses is confined to this source.

5.4 Jet Spatial Volume

Given that the jet source region is typically longer in the axial dimension than the radial or transverse dimensions, it may be acceptable to approximate the volume distribution of jet noise sources as an axial distribution. This approximation would result in a reduction of the number of jet noise sources. Additionally, as an axisymmetric RANS solution is the input of choice, a 3D distribution must be generated.

Selecting the full-3D source distribution, used in the previous section, as a benchmark, figures 5.19 and 5.20 compare the effect of computing the propagation distance, between the source at $\mathbf{x_s}$ and a receiver at $\mathbf{x}$, as $r = |\mathbf{x} - \mathbf{x_s}|$ and $r \approx |\mathbf{x} - x_{s1}\hat{\mathbf{i}}|$ (to be referred to as the *full-1D* source). Such an approximation is common in far-field isolated jet noise predictions, and indeed, it is often the case that the approximation $r \approx |\mathbf{x}|$ is made. However, for shielding predictions, where the location and spatial extent of the source region are important factors, such approximations must be questioned. As such, it can be observed that both the isolated and shielding factor predictions are almost identical, although there is some small variation in the high-frequency shielded case.

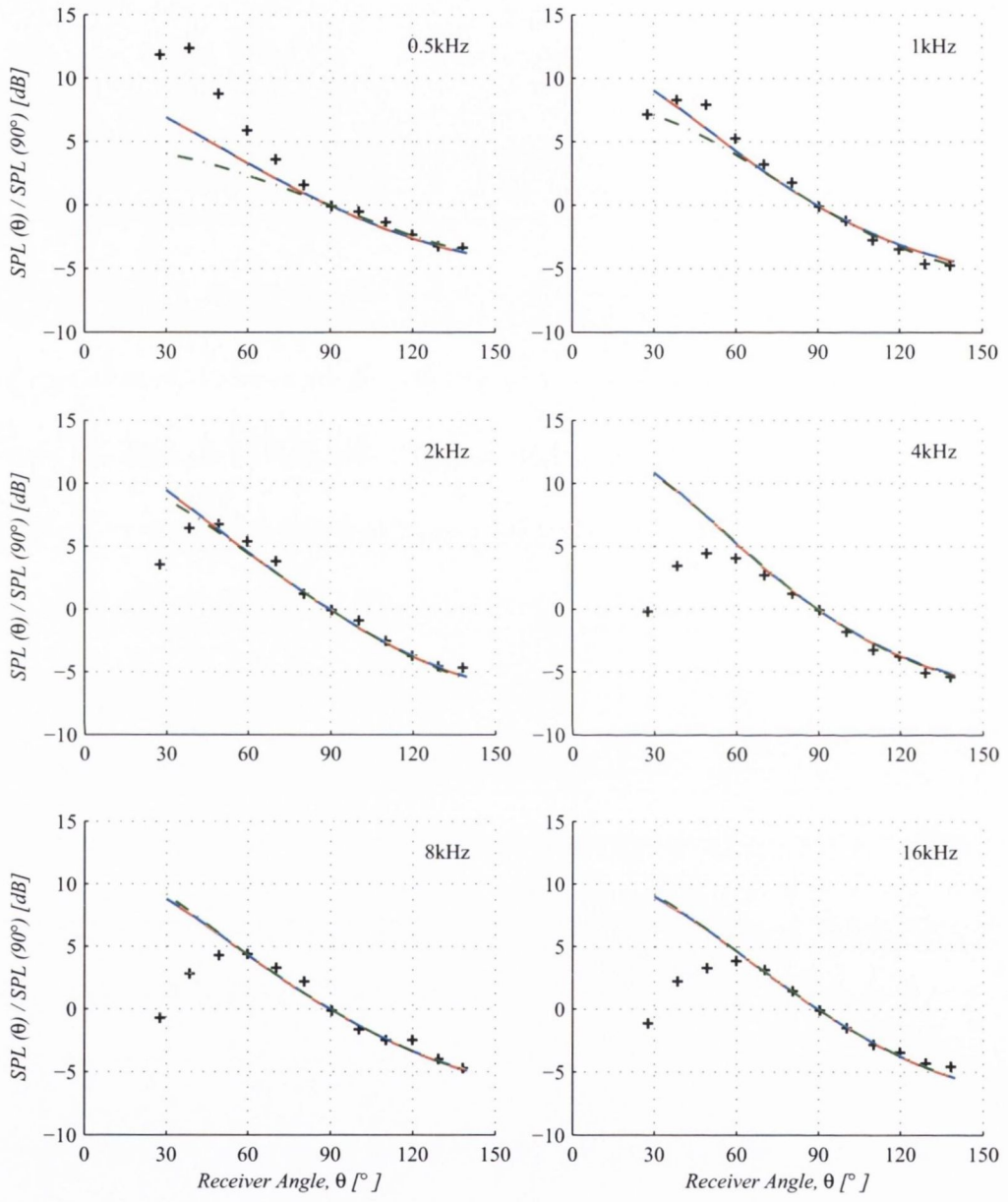

Figure 5.19: Axial model: isolated normalised far-field SPL $[dB]$ directivity from NACRE test data (black $+$) and Model$_C$ with $\mathbf{r} = \mathbf{x} - \mathbf{x_s}$ (red $-$), $\mathbf{r} \approx \mathbf{x} - x_{\mathbf{s}1}\hat{\mathbf{i}}$ (blue $--$) and $\mathbf{r} \approx \mathbf{x}$ (green $-\cdot$).

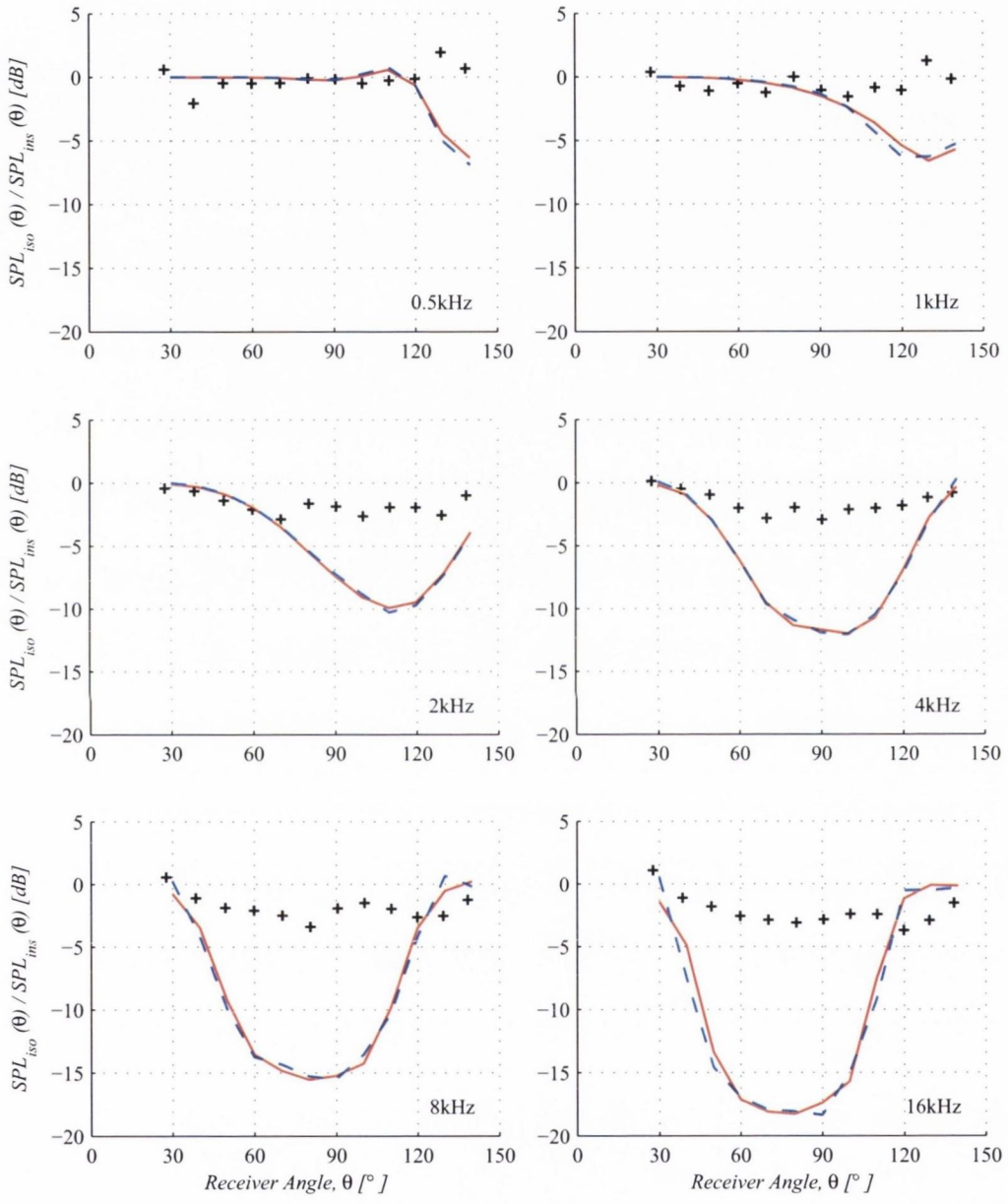

Figure 5.20: Axial model: far-field shielding factor $[dB]$ directivity from NACRE test data (black $+$) and Model$_C$ with $\mathbf{r} = \mathbf{x} - \mathbf{x_s}$ (red $-$) and $\mathbf{r} \approx \mathbf{x} - x_{\mathbf{s}1}\hat{\mathbf{i}}$ (blue $--$).

The case of $r \approx |\mathbf{x}|$ has been included in the isolated predictions. Here it can be seen how the neglected axial position leads to an under-prediction of the far-field directivity at low-frequencies, as would be expected from simple geometric considerations. This is in contrast to the effect of the axial shift imposed through the model constants discussed in section 5.3.3, where the underlying input values were changed.

5.5 Jet Source Reduction Schemes

It was proposed in chapter 4 that the total jet volume could be divided into a small number of sub-volumes blocks, each of which is represented by a directional point sources in shielding computations. Although there are computational benefits to be gained by reducing the number of sources, which represent the jet noise, care should be taken that the reduction scheme employed does not reduce the quality of the prediction to any appreciable extent. In the present case, the predictions from the full-3D source is the benchmark that must be matched.

5.5.1 Uniform Sub-Volumes

As a starting tactic, the jet source volume was divided into square blocks, which were uniform in dimensions throughout the source region. As the selection of the length of each block is arbitrary, a number of different block scales were investigated. If V_1 is the axial dimension of the jet source volume, blocks of length $L = V_1/100$, $V_1/10$ and $V_1/5$ were analysed. Once the local block properties have been defined, they are all considered to lie on the jet axis, and thus, the propagation distance is taken as $r = |\mathbf{x} - x_{s1}\hat{\mathbf{i}}|$.

Figures 5.21 and 5.22 display the far-field results of this reduction scheme. It can be seen that the $V_1/100$ source matches the full-3D source perfectly, and that this agreement deteriorates somewhat with the coarser spacing. Interestingly, even with as few as five axial source locations (in the $V_1/5$ source), predictions are reasonably consistent with the full-3D source distribution, and even manage to match the prediction at some frequencies, such as the $8kHz$ isolated prediction. This

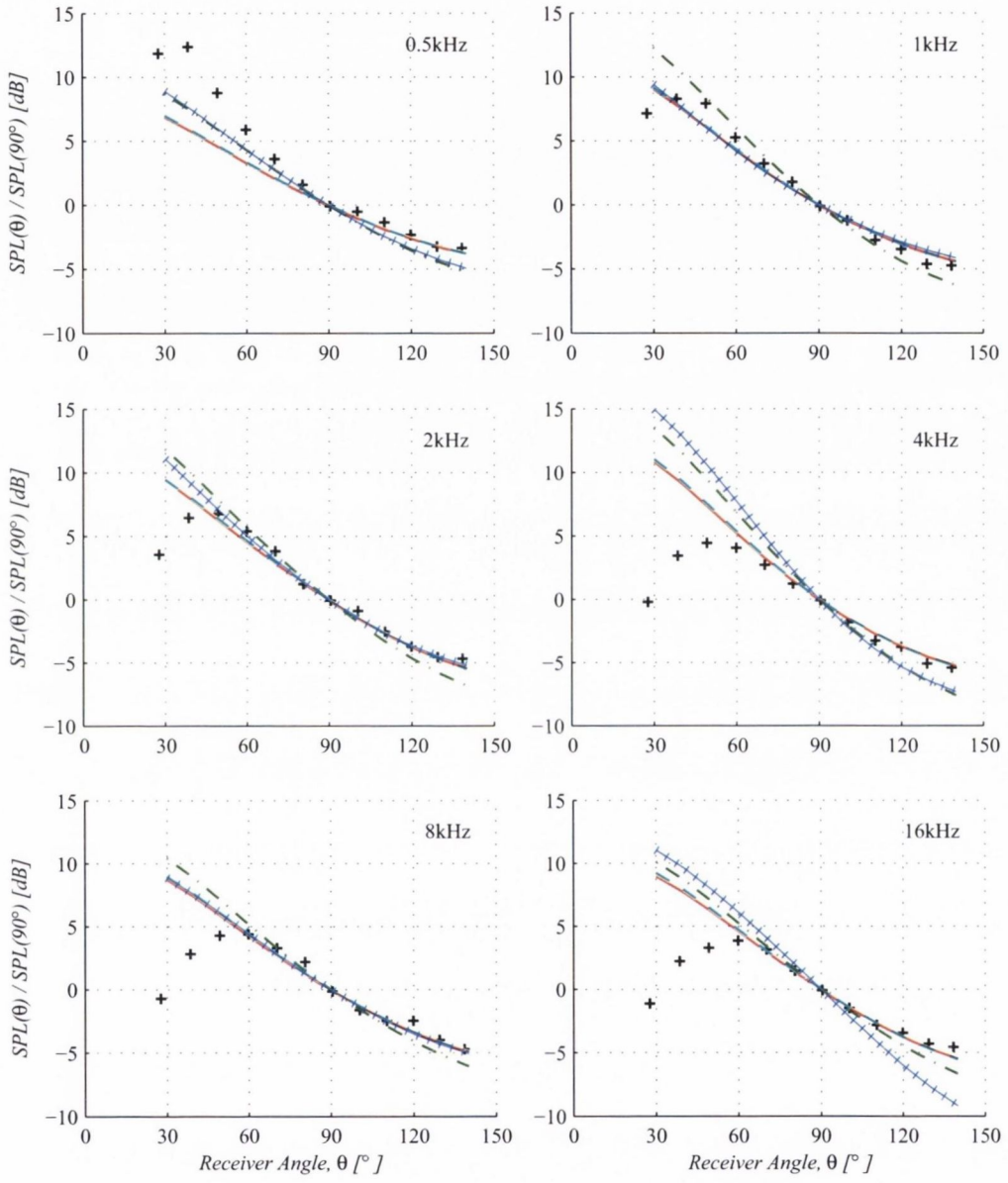

Figure 5.21: Source reduction using a uniform block dimension scheme: normalised isolated far-field SPL $[dB]$ directivity from NACRE test data (black +), and Model$_C$ with full source distribution, $\Delta V = dV$ (red $-$), and reduced source distribution with $\Delta V = (V_1/100)^2$ (cyan $--$), $\Delta V = (V_1/10)^2$ (green $-\cdot$) and $\Delta V = (V_1/5)^2$ (blue $-|-$).

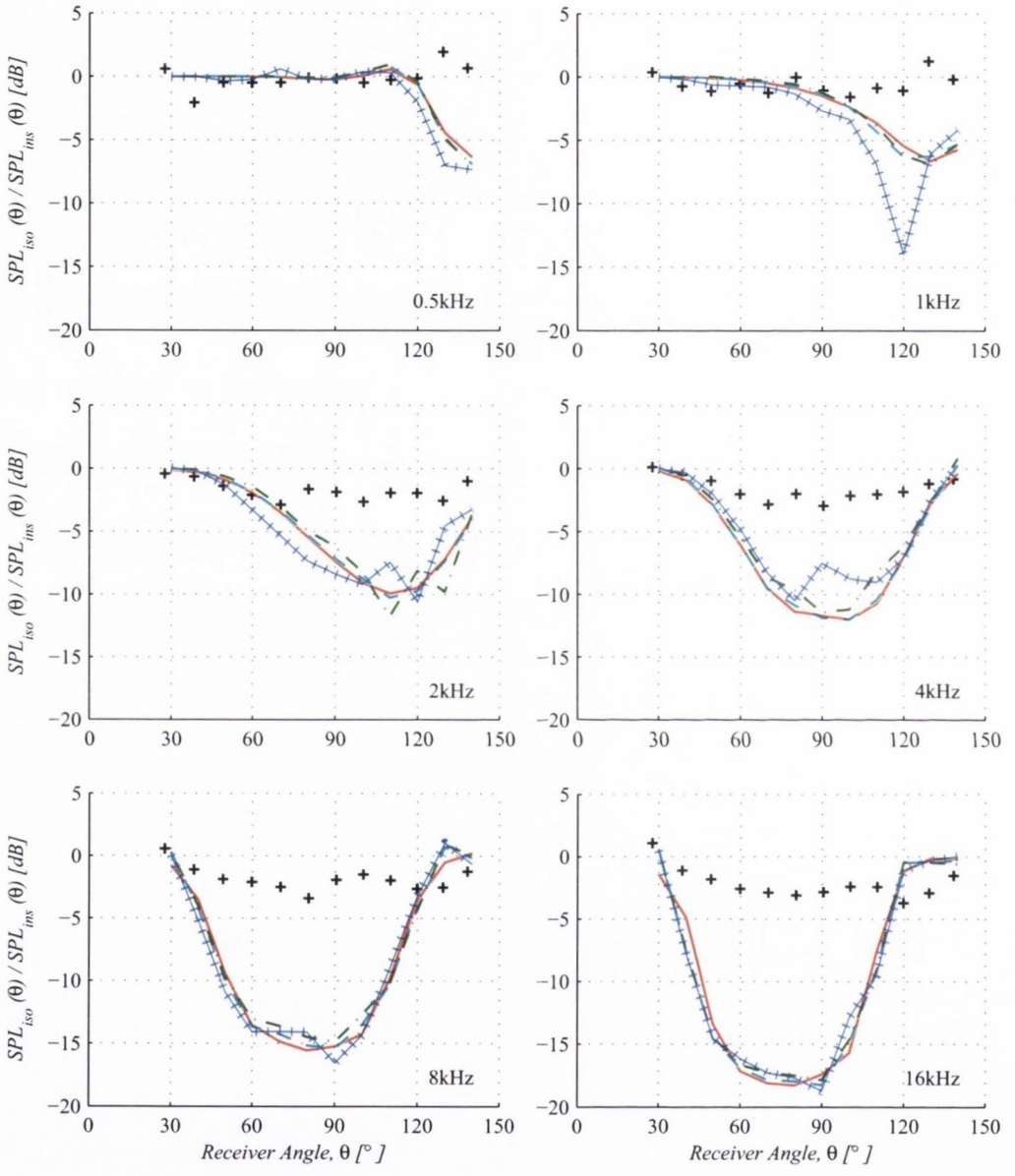

Figure 5.22: Source reduction using a uniform block dimension scheme: far-field shielding factor $[dB]$ directivity from NACRE test data (black +), and Model_C with full source distribution, $\Delta V = dV$ (red $-$), and reduced source distribution with $\Delta V = (V_1/100)^2$ (cyan $--$), $\Delta V = (V_1/10)^2$ (green $-\cdot$) and $\Delta V = (V_1/5)^2$ (blue $-|-$).

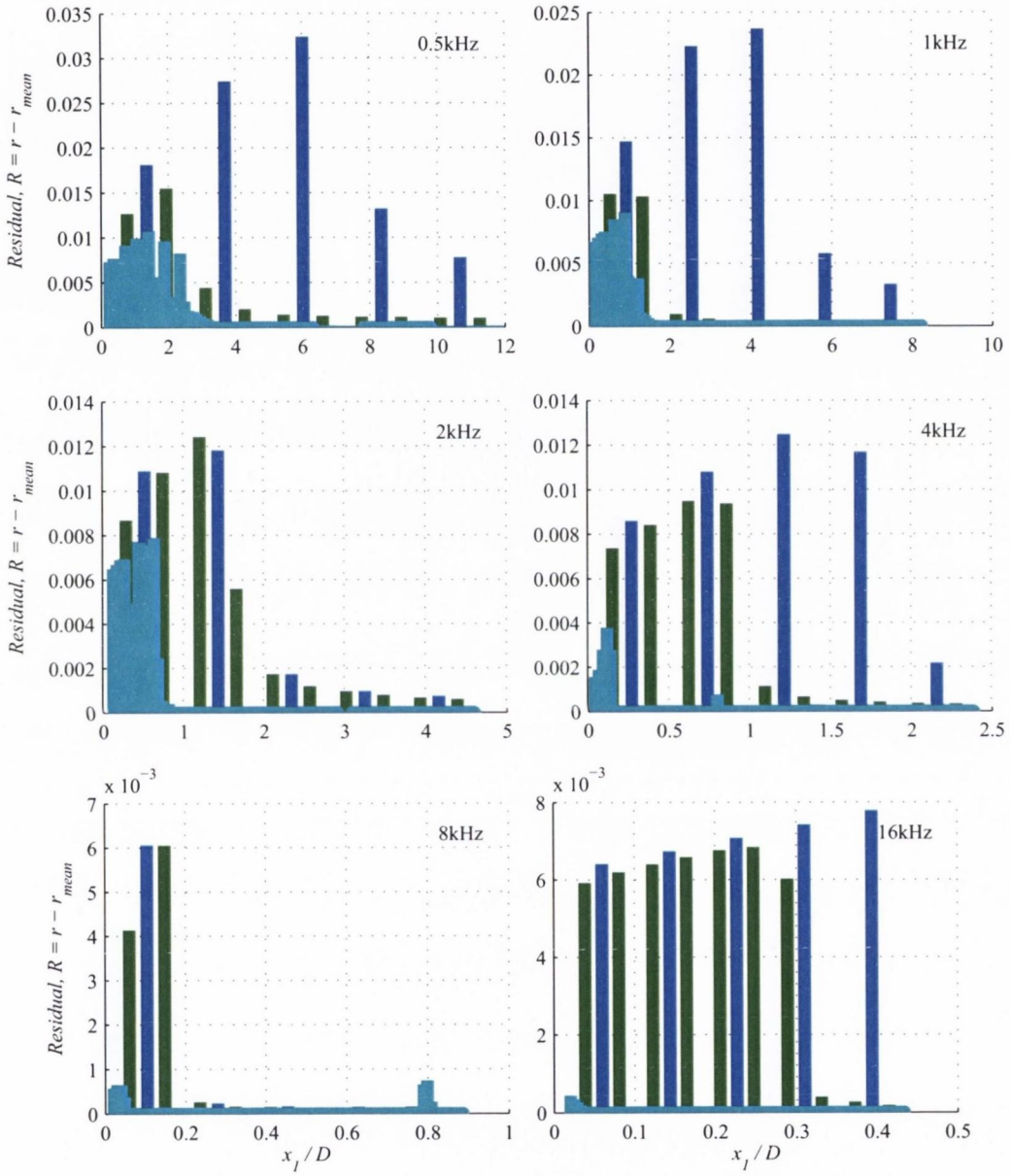

Figure 5.23: Source reduction using a uniform block-dimension scheme: time-scale residual $[s]$ from reduced Model_C source distribution with square blocks $\Delta V = (V_1/100)^2$ (cyan), $\Delta V = (V_1/10)^2$ (green) and $\Delta V = (V_1/5)^2$ (blue).

shows that retaining one source per element of the RANS mesh is indeed excessive for shielding computations.

The reason for the decline in the agreement, with this source reduction scheme, is due to the residual in the evaluation of the block-averaged values of $< \tau_t >$, $< l_t >$ and $< U_c >$, as this essentially is the only difference from the full source. Figure 5.23 shows a plot of the time-scale residuals for these three source distributions (note the axes vary in these plots), and as can be seen, the $V_1/100$ source maintains the lowest residual, although observe that this residual is skewed left (this is best observed in figure 5.26, where the $V_1/100$ residual is re-plotted), suggesting that a more appropriate reduction scheme might be to link the sub-volume block size to the scales of the turbulence, which become finer closer to the nozzle exit.

5.5.2 Scaled Sub-Volumes

In this source reduction scheme the jet volume is divided into sub-volume blocks, whose dimensions scale (roughly) with the length-scale of the turbulence. The far-field acoustic predictions are displayed in figures 5.24 and 5.25 for two variations of this scaled block dimension scheme – one with square sub-volume blocks (as before), referred to as the *scaled-square* source, and the other with (rectangular) blocks that are full axial slices of the jet (and so there is only one source at each axial block location), referred to as the *scaled-axial* source. The axial locations of these two source distributions are identical. The scaled-axial block source distribution shows some deviation from the full-3D source. The scaled-square source does match the benchmark source exactly.

Once again, any deviation is due to the residual of the block-averaged values. Figure 5.26 shows the time-scale residual for these source distributions, and for the uniform-block scheme with $V_1/100$. It can be observed that the residual for the scaled-square source is small for all sources, and there is no longer evidence of the skewness observed in the $V_1/100$ source distribution.

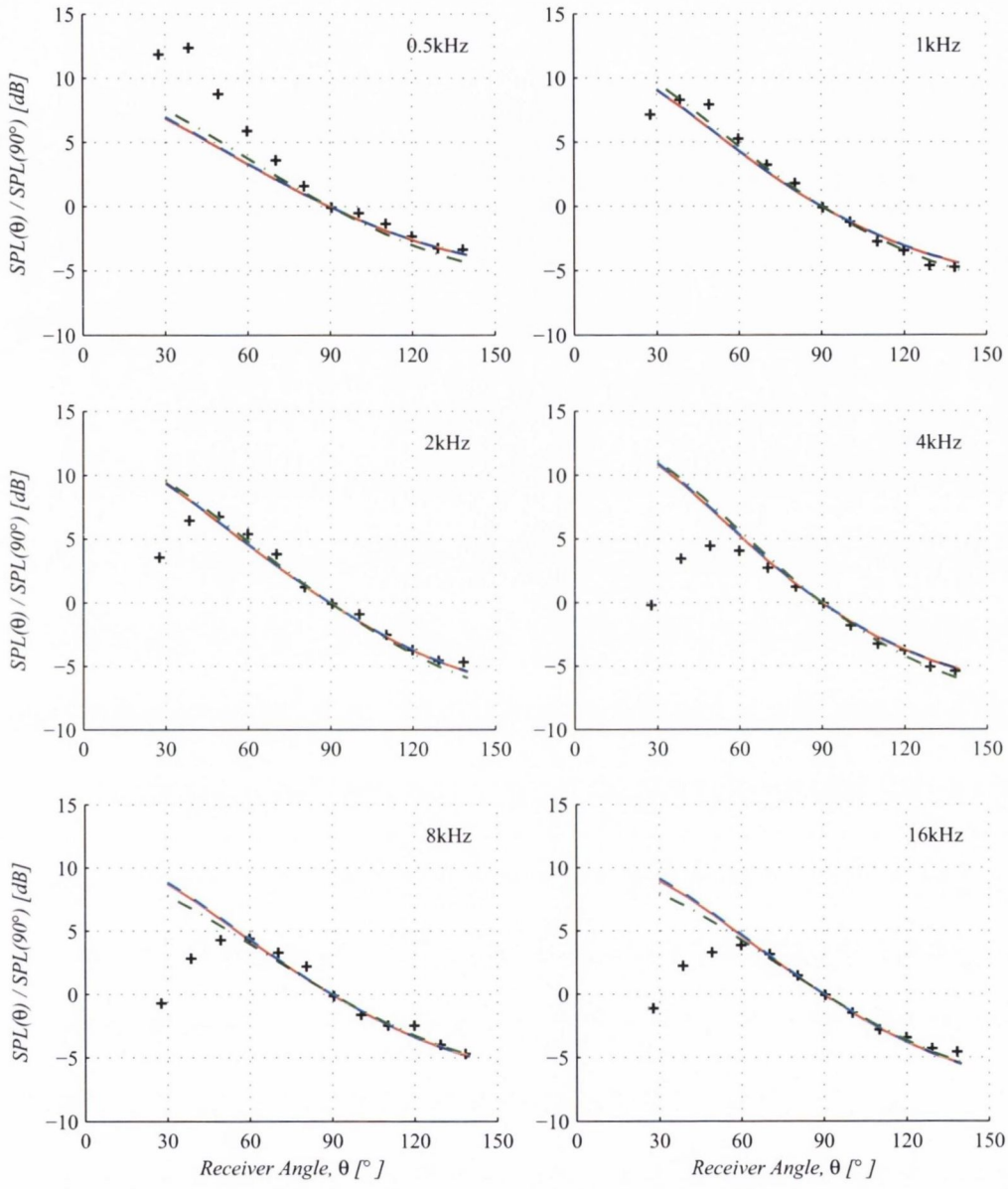

Figure 5.24: Source reduction using a scaled block-dimension scheme: normalised isolated far-field SPL $[dB]$ directivity from NACRE test data (black $+$) and Model$_C$ with full source distribution, $\Delta V = dV$ (red $-$), reduced source distribution with scaled square blocks, $\Delta V = L^2$ (blue $--$) and reduced source distribution with scaled axial slices $\Delta V = L\,V_2$ (green $-\cdot$).

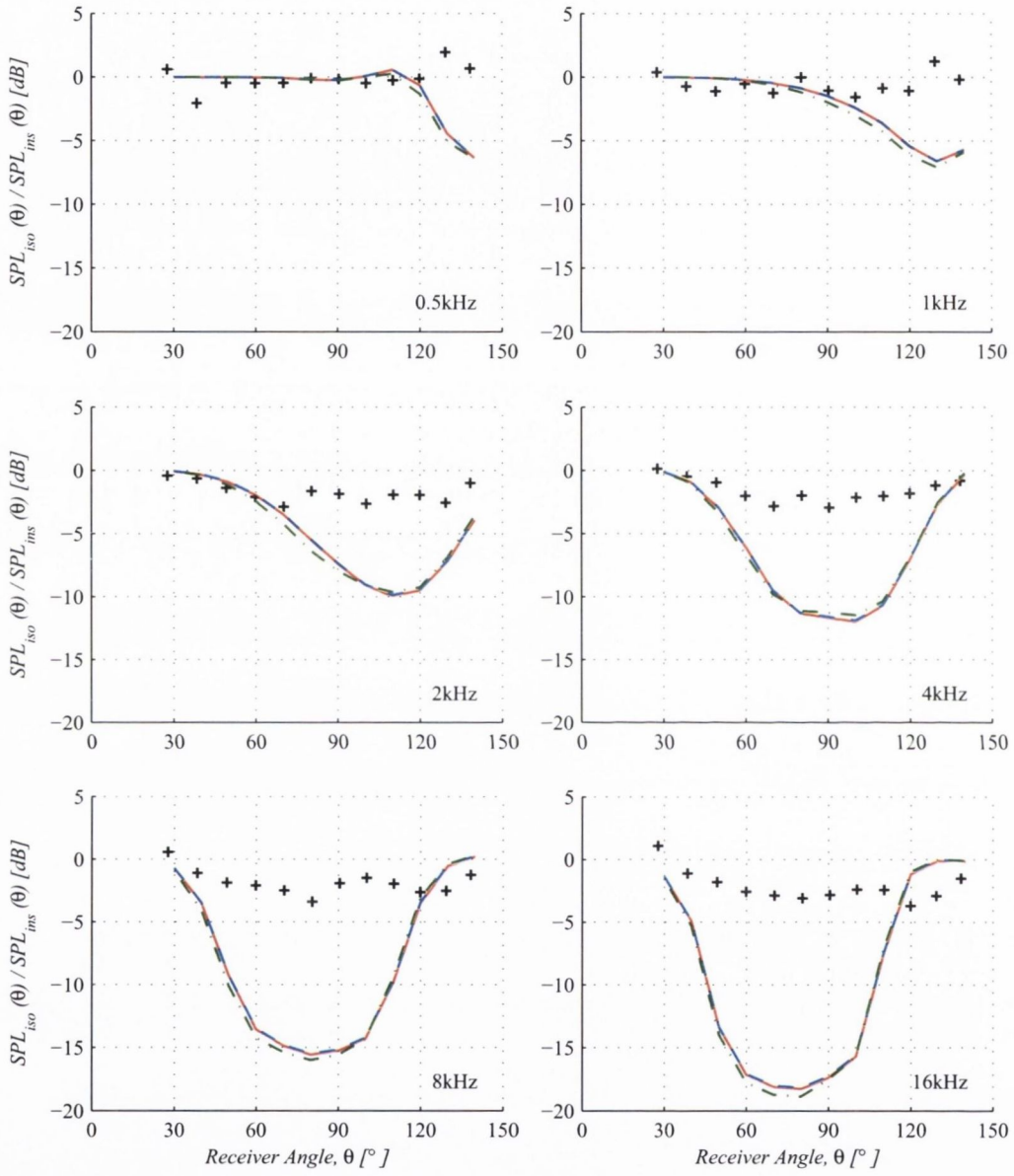

Figure 5.25: Source reduction using a scaled block-dimension scheme: far-field shielding factor $[dB]$ directivity from NACRE test data (black $+$) and Model$_C$ with full source distribution, $\Delta V = dV$ (red $-$), reduced source distribution with scaled square blocks, $\Delta V = L^2$ (blue $--$) and reduced source distribution with scaled axial slices $\Delta V = L\,V_2$ (green $-\cdot$).

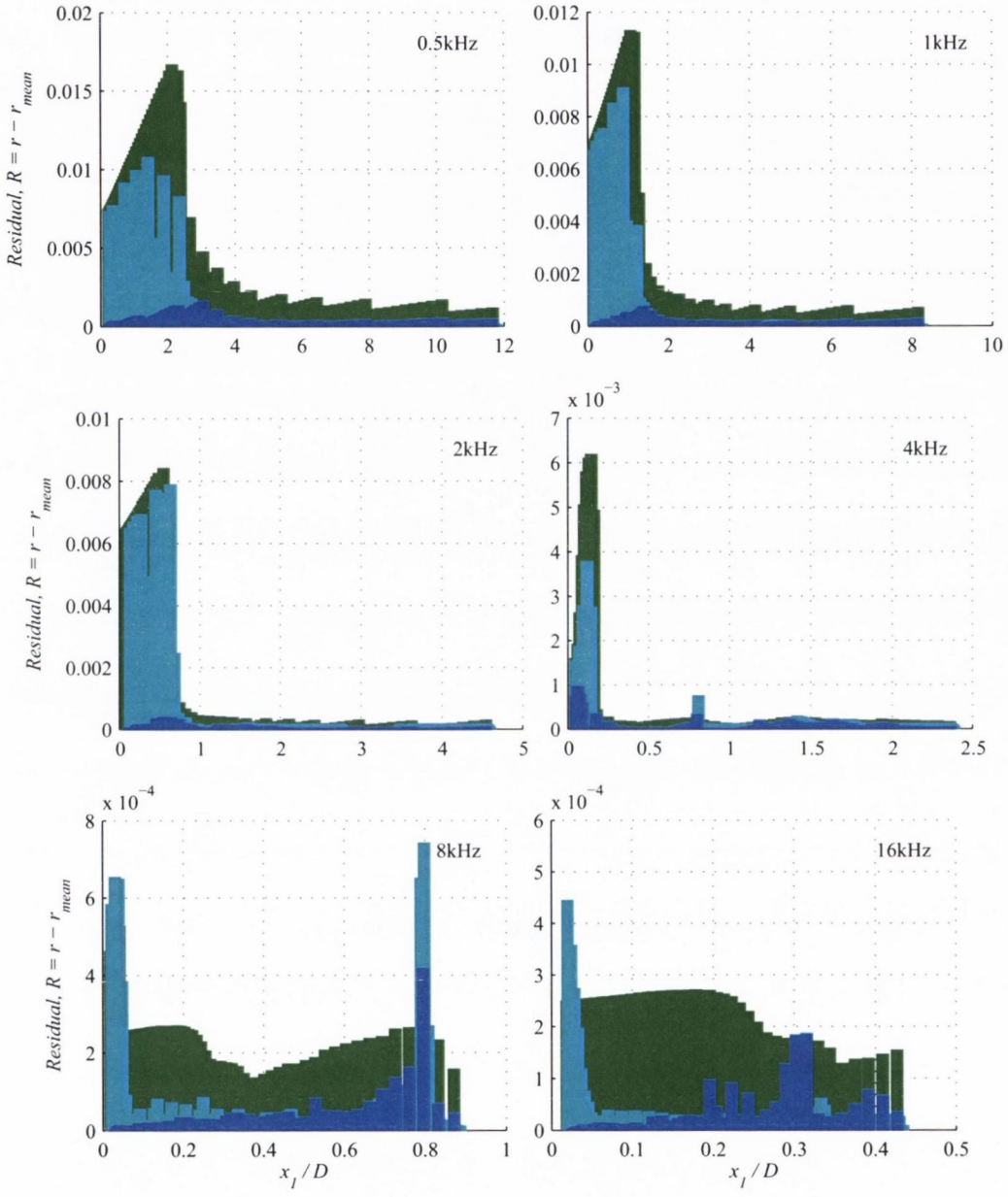

Figure 5.26: Source reduction using a scaled block-dimension scheme: time-scale residual $[s]$ from reduced Model_C source distribution with scaled-square blocks $\Delta V = L^2$ (blue), with scaled-axial slices $\Delta V = L\,V_2$ (green) and with uniform-square blocks $\Delta V = (V_1/100)^2$ (cyan).

5.5.3 Computational Savings

Table 5.3 shows the number of point sources defined for each axial source distribution. Dassault's RANS mesh had 159,322 elements. Another flaw of the uniform block distribution scheme is immediately apparent, as it can be seen that the number of sources increases greatly with frequency. This is a repercussion of indiscriminately dividing a small source region by, what is, an arbitrary number. The scaled-square source, on the other hand, does not show this trait, as the division size is not linked to the dimensions of the source region, and so this scheme is more robust than the uniform block scheme. The scaled block scheme should minimize the number of sources required in a jet noise shielding prediction to satisfactorily represent the jet, whilst maintaining the accuracy of predictions.

Source	$0.5kHz$	$1kHz$	$2kHz$	$4kHz$	$8kHz$	$16kHz$
RANS elements	159,322	159,322	159,322	159,322	159,322	159,322
Full-1D	39,005	32,880	21,733	8,776	2,115	718
$V_1/100$	929	929	1,213	1,562	2,375	2,896
$V_1/10$	10	10	20	28	29	43
$V_1/5$	5	5	5	10	10	14
Scaled-Square	772	686	567	504	622	716
Scaled-Slice	92	89	77	66	83	66

Table 5.3: Number of point sources for each of the source distributions.

Figure 5.27 displays scatter plots for the computational time taken to compute the shielding factor using a FKM code. As might be expected, it is clear that a reduction in the number of sources gives a reduction in computational time. Although, the computational cost will vary greatly with the method used and the efficiency of the code itself, this trend should be typical of all shielding predictions.

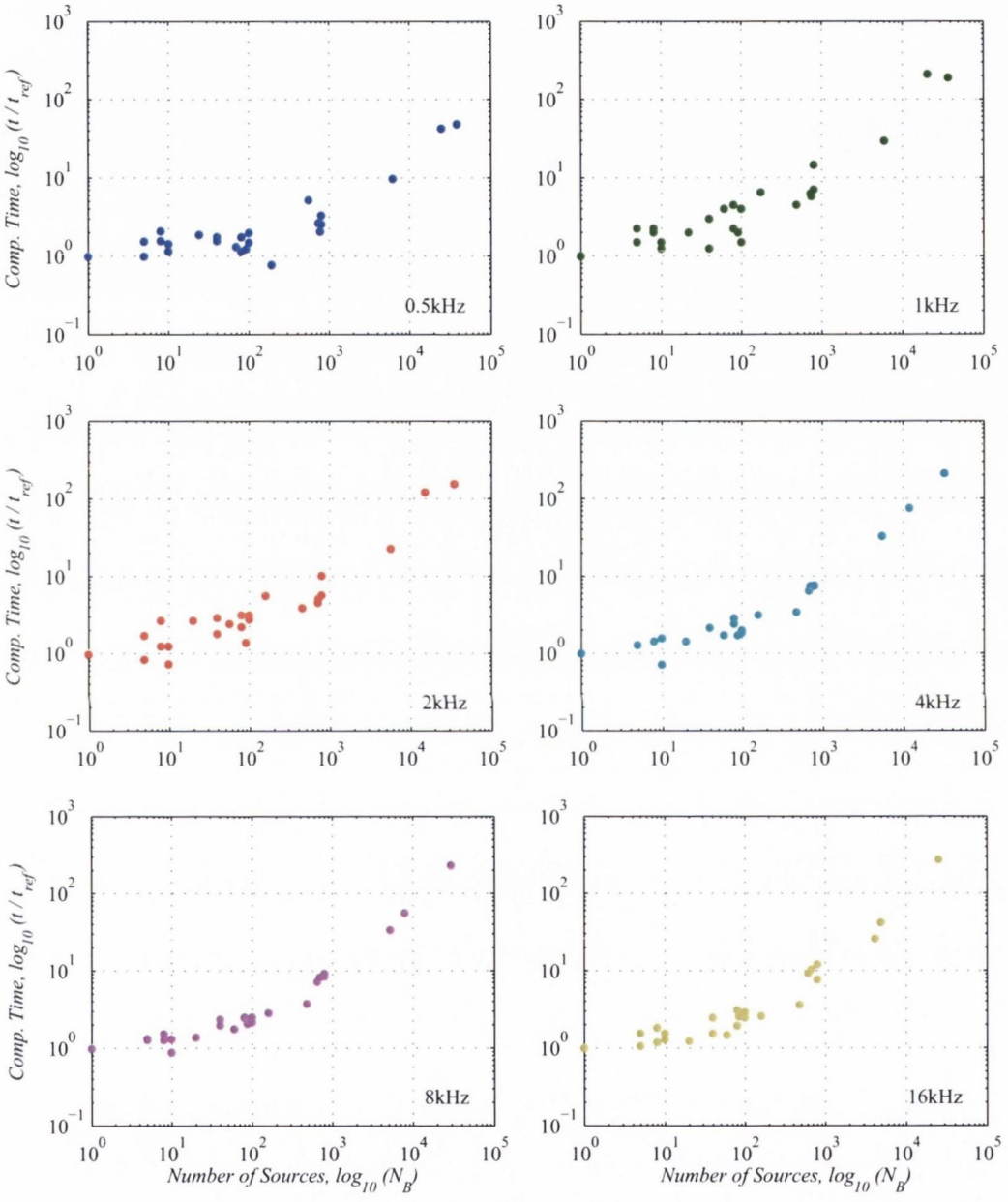

Figure 5.27: Computatinal time of the Fresnel-Kirchhoff shielding prediction method (t_{ref} is the computational time for one source) against the number of sources.

5.6 Mean Flow Propagation Effects

The jet self-noise sources, which have been considered in this work, are in themselves omnidirectional. The directionality of the sound field generated by a jet is due to the mean flow (for the most part), which convects the sources downstream, and also refracts the propagating sound away from the axis. In this section, the impact of these effects on jet shielding predictions is examined.

5.6.1 Source Convection

The convection of the source by the mean-flow acts to amplify the source in the downstream direction and Doppler shifts the frequency of the propagating sound field. This convection effect has been included in the present model, through the correlation function, R, and appears as the convection factor, C. In the evaluation of C, the convection velocity must be estimated, most likely, using a scaled function of space based on the axial velocity from the RANS solution [30, 8]. However, as has been shown, different jet noise models, with varying model constants, can lead to very different jet source locations and, therefore, different underlying mean flow values for the source.

In order to assess the impact of source convection on shielding predictions, two cases were compared, namely, with and without source convection. Figures 5.28 and 5.29 present the far-field acoustic predictions for this comparison. As is expected, the isolated results show little directivity when convection is neglected. The directivity visible at low frequencies is due to the location of the sources closer to the downstream receivers.

For shielded predictions, it can be observed that there is a shift in the angle of peak shielding (certainly at lower frequencies), and also, an increase in the shielding factor when the sources are omnidirectional. It is reasonable to expect that these trends should also be observed at other convection values.

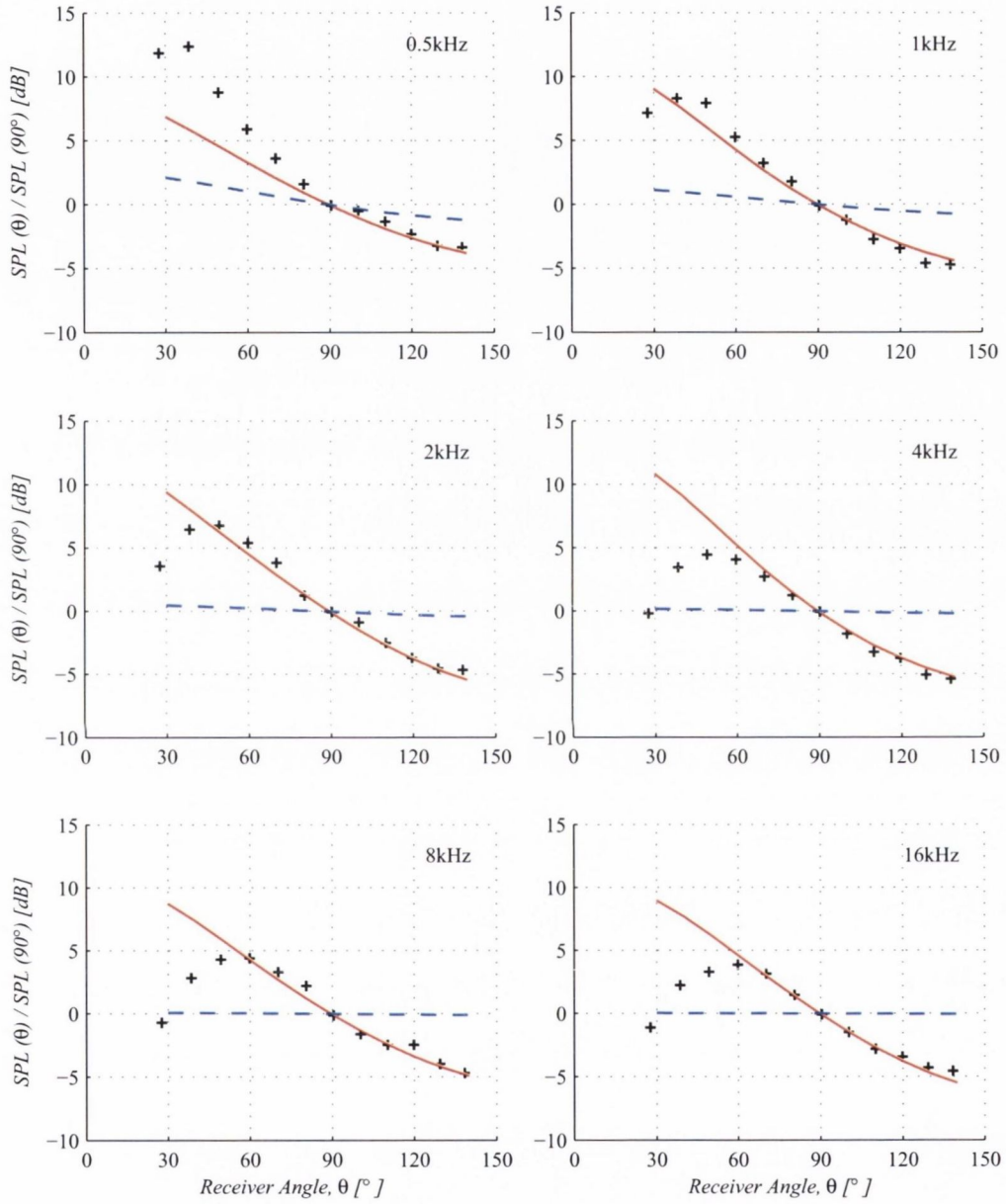

Figure 5.28: Source convection: isolated normalised far-field SPL $[dB]$ directivity from NACRE test data (black +) and Model$_C$ with convection (red $-$) and without convection (blue $--$).

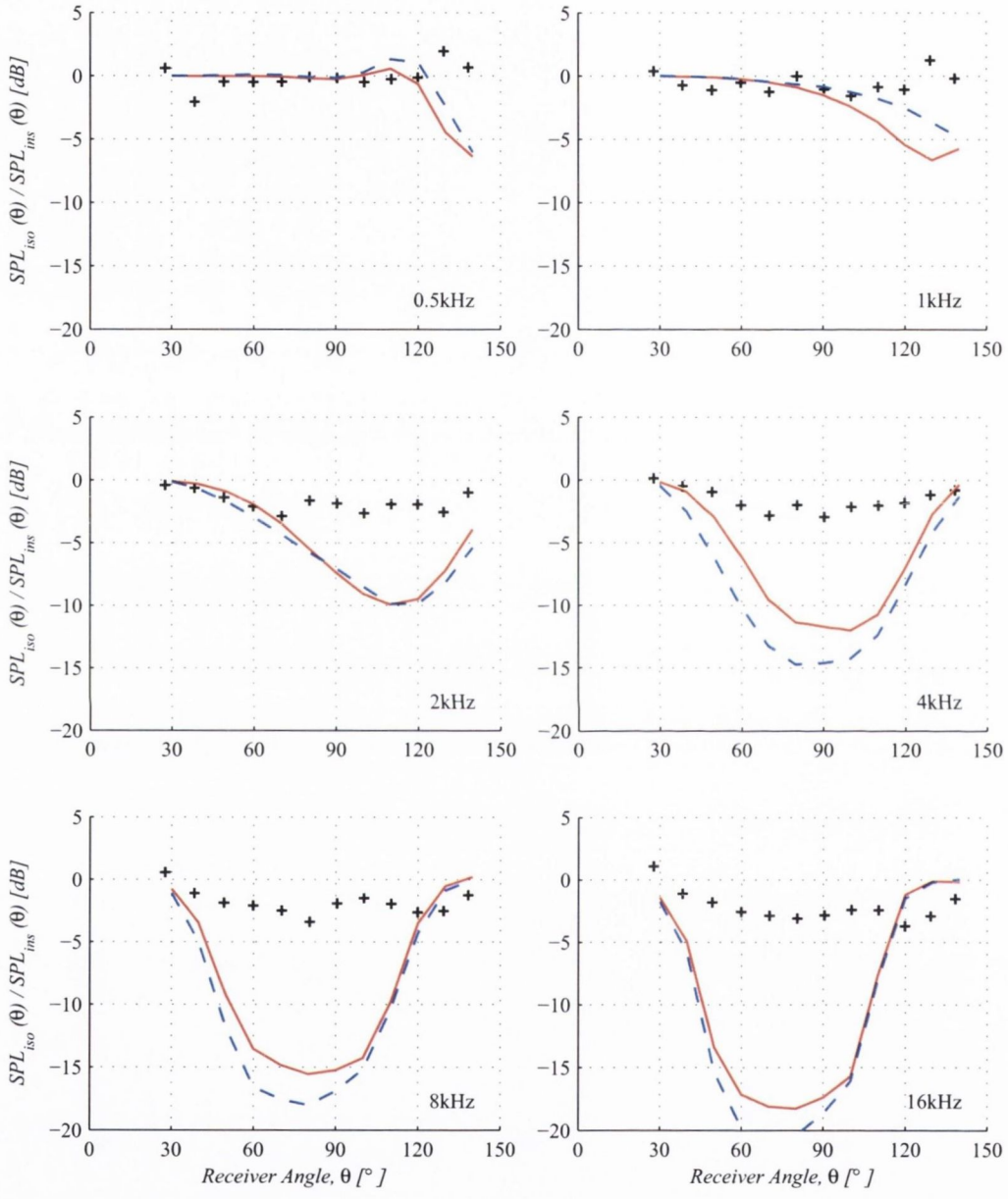

Figure 5.29: Source convection: far-field shielding factor $[dB]$ directivity from NACRE test data (black $+$) and Model$_C$ with convection (red $-$) and without convection (blue $--$).

5.6.2 Flow Refraction

The refractive effect of the mean jet flow on sound propagation has been included through a directivity correction factor (equation (4.39)). This is very much an approximate approach but it should be sufficient to identify whether or not refraction is a likely to be responsible for the large differences between the predicted shielding levels and the data values. As this approach is intended to be a computationally cheap correction for the refraction effect, the WEM propagation was carried out in 2D. This introduces a small error in the propagation values, however, as a ratio value is the result of this computation, and given the approximate nature of the strategy itself, this approximation were considered to be acceptable. The scaled-square reduced source distribution was used to specify the unit volume source locations.

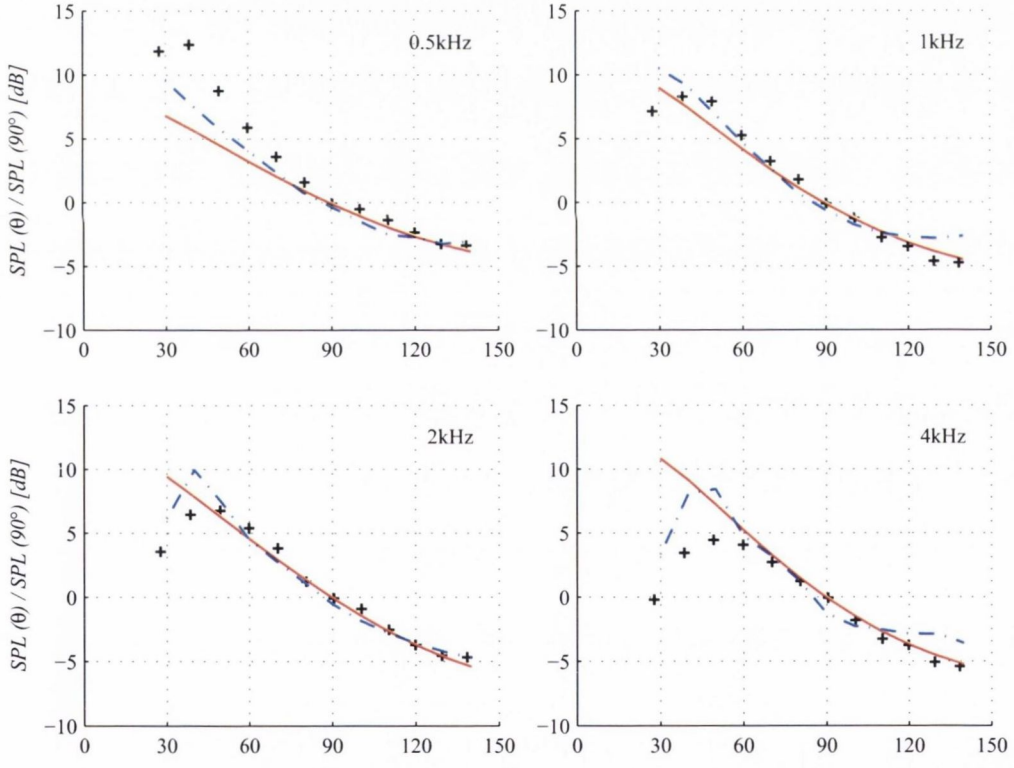

Figure 5.30: Flow refraction: normalised isolated far-field SPL $[dB]$ directivity from NACRE test data (black +) and Model$_C$ without (red $-$) and with (blue $--$) refraction correction factor.

Figure 5.30 displays the isolated far-field predictions. The refracted predictions do show a drop-off in SPL corresponding to the cone of silence, however, it would appear that the predicted angle at which drop-off occurs is closer to the jet axis than the measured values show. This may, again, be due to the location, at which, the sources have been embedded in the RANS flow solution.

Figure 5.31 show the shielded predictions. The results with refraction only show a small deviation from those without refraction. Although it is difficult to draw any clear conclusions, as the margins of difference are quite small, it may be said that refraction of the propagating sound does not appear to be reason for the large differences between predicted shielding factors and the NACRE test data.

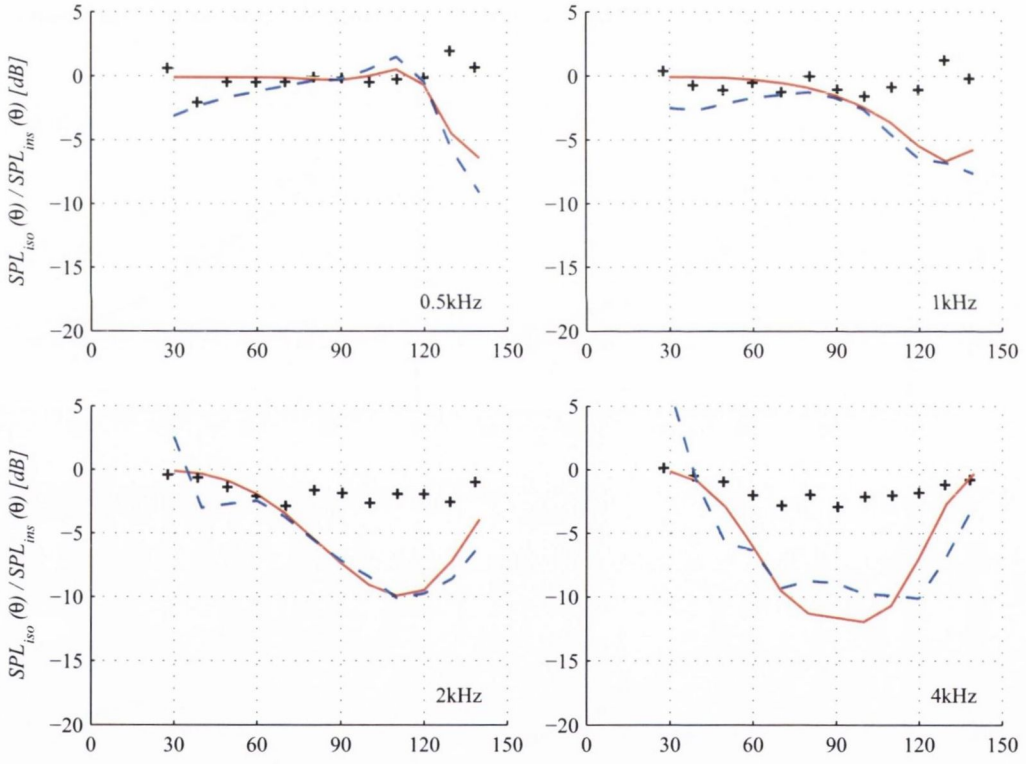

Figure 5.31: Flow refraction: far-field shielding factor $[dB]$ directivity from NACRE test data (black $+$) and Model$_C$ without (red $-$) and with (blue $--$) refraction correction factor.

5.7 NACRE Partner's Predictions

Numerical jet shielding predictions have been computed for the same RANS solution by NACRE partners Snecma and Dassault Aviation. Snecma modelled the jet using a hybrid Tam-Auriault method (that they call the THM), which essentially is the TA model (from section 3.3) at 90° to the jet axis, with a separate directivity correction that is calibrated with Snecma's far-field jet noise database. Shielding predictions were computed using an in-house ray tracing code with a diffraction correction based on Cooke's theory [27]. The EUROPIV is modelled as two semi-infinite planes. This code, however, is limited to omnidirectional sources, and so, the jet source is included in the shielding calculation as a monopole distribution, with one source per element of the RANS mesh.

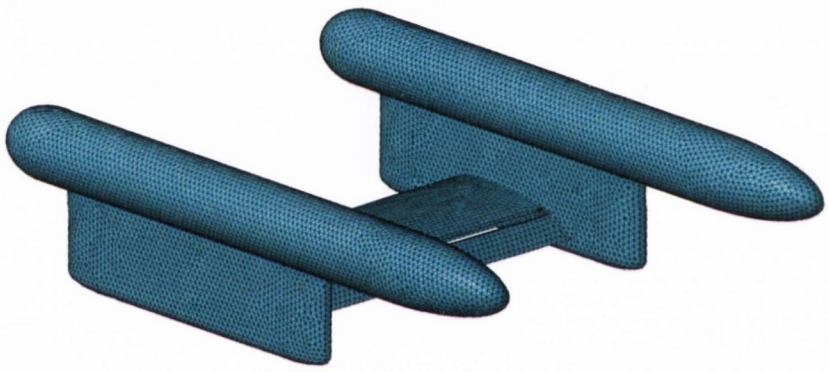

Figure 5.32: EUROPIV model for Dassault's $2kHz$ BEM computation.

Dassault used the TA model with an additional adjustment to the model constants, c_l and c_t, proposed by Tam for hot jets [83]. The shielded Green's functions were computed by a BEM code, which included the full 3D EUROPIV geometry, as shown in figure 5.32. The computational demands for such a calculation are very large – at $8kHz$, a BEM mesh with over $1.6M$ nodes is required. Dassault's predictions were, therefore, limited to $800Hz$ and $2kHz$. A Green's function was computed to each element in the RANS solution.

Figure 5.33 and 5.34 show a comparison of the far-field acoustic predictions using the present modelling methodology with the available predictions from Das-

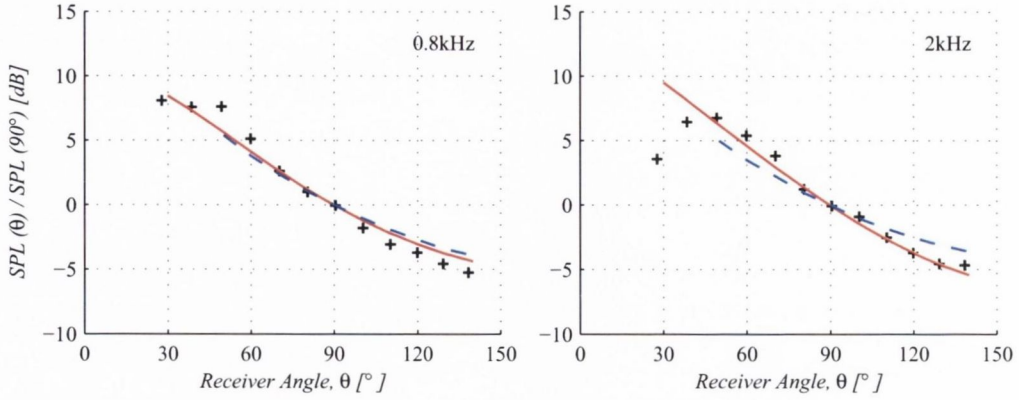

Figure 5.33: NACRE partner's predictions: isolated normalised far-field SPL $[dB]$ directivity from NACRE test data (black +), Model$_C$ (red $-$) and Dassault's TA code (blue $--$).

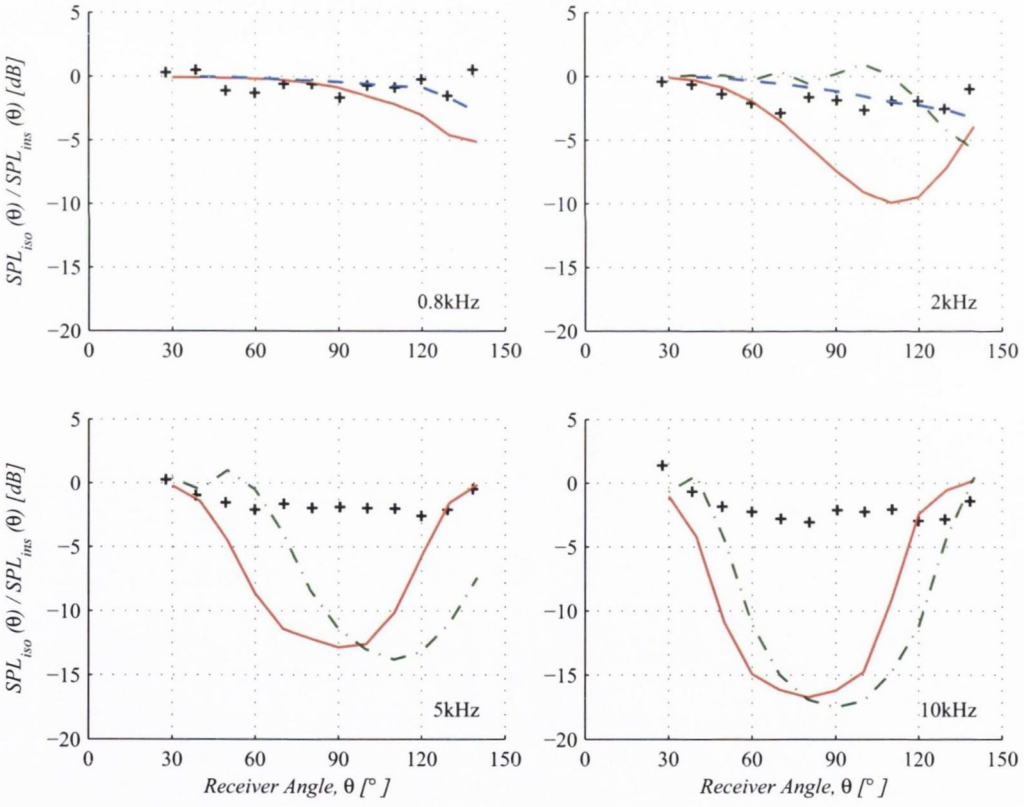

Figure 5.34: NACRE partner's predictions: far-field shielding factor $[dB]$ directivity from NACRE test data (black +), Model$_C$ with FKM (red $-$), Dassault's TA with BEM (blue $--$), and Snecma's THM with Cooke's Diffraction (green $-\cdot$).

sault Aviation's and Snecma's approaches. Although at first, the results may appear quite different, in light of the trends established in section 5.3.3, it is plausible to attribute the differences to an axial shift of the source region. Snecma's predictions would certainly appear to be due to a combination of this reason and the omnidirectional nature of their jet sources (see section 5.6.1). There may also be some small contribution to the difference from the fact that two shielding planes were used.

Dassault's isolated predictions show a stronger directivity than those presented in figures 5.14 or 5.15 from the TA model. As the models used are identical, except for the evaluation of the model constants, this difference, again, ties into the suggestion that their sources are located further downstream. Dassault calibrated their jet model with a far-field database. It is unclear whether or not the full BEM geometry captures any effect, which has been missed in the geometry approximations of the other two shielding prediction methods, as a peak shielding factor is not reached for the two frequencies investigated by Dassault.

5.8 Summary

In this chapter, many trends relevant to acoustic shielding predictions from a jet noise source have been established. The use of the modelling methodology presented in chapter 4 as a sensitivity analysis tool has been demonstrated. It has been shown that RANS based jet noise models are capable of predicting the far-field noise directivity from an isolated jet, if the model scaling constants are *tuned* appropriately.

It has also been shown that the jet may be represented in propagation methods by a relatively small number of axially distributed directional sources, thereby, reducing the computational demands of such calculations. However, for jet shielding predictions, the tuning of model constants may significantly alter the location and the near-field directivity of the jet noise source, and therefore impact largely on predicted shielding factors.

Additionally, despite the calibration of jet noise models, the shielding predictions fail to reproduce the NACRE test data values for the shielding factor. This

raises many questions about the current strategies employed for jet noise shielding assessment, which are addressed in chapter 6.

Chapter 6

Discussion

In chapter 5, it has been shown that semi-empirical jet models, with $\kappa - \epsilon$ RANS generated mean flow values, have the potential to predict the far-field noise directivity from a turbulent jet. However, when an acoustic shield in located between the jet noise source and the far-field receivers, the reduction in SPL values is greatly over-predicted in comparison with those observed in the test data. In this chapter, the possible causes of this disagreement are probed, and some general jet broad considerations are discussed.

6.1 A Lack of Shielding?

Perhaps the most striking feature of the NACRE measurements are the low shielding levels (a $4dB$ reduction at most) even at the highest frequencies. For an incoherent source distribution, positioned near the location of the secondary nozzle lip, shielding factors of up $20dB$ are predicted, as shown in figure 6.1. This magnitude of attenuation is typical of predictions for computational setups of this type (as has been shown in section 5.7, and also in references [2, 62], amongst many others).

Although there may be some uncertainty as to the location of low-frequency jet noise sources (as was shown in sections 5.3 and 5.7), it can be expected that high-frequency jet noise production is concentrated in the shear layer immediately downstream of the nozzle lip. The beam-forming axial source position, computed from the NACRE data, has indicated as much (see figure 5.8). Assuming that the

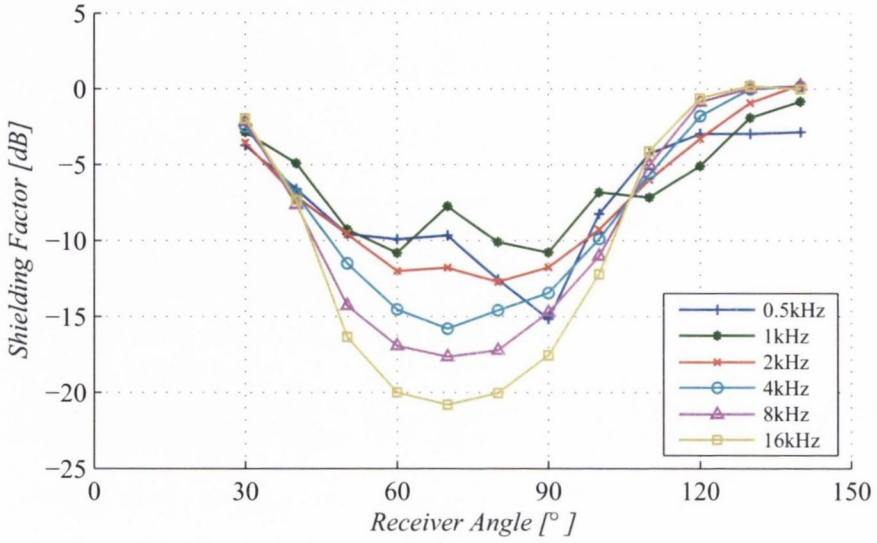

Figure 6.1: Shielding factor from a ring of incoherent monopoles on the secondary exit plane.

NACRE measurements are free from large errors, the poor shielding levels observed are something of a curiosity, if it is assumed that the present jet noise shielding methodologies are valid. There are a number of possible reasons why these methodologies fail to predict the NACRE levels of shielding.

6.1.1 The Role of Jet Noise Models

Lighthill's equation is exact. The problem with acoustic analogies is not so much the analogies themselves, but rather the inexact flow information they rely upon. Models based on acoustic analogy do provide excellent predictions of rotor-craft, propeller and airfoil noise [38], where the sources may be well defined. Steady-state RANS solutions provide limited averaged information about jet flow fields, and are themselves subject to significant variations, which impact the accuracy of acoustic predictions.

Using time-averaged inputs to acoustic analogy type models requires the modelling of space-time correlation functions, which scale over the source region. A great variety of models have been proposed since Lighthill's papers in the early 1950s, which attempt to match the turbulent statistics within the source region, and ul-

timately enhance far-field spectral and directivity predictions. A RANS solution may be used to provide the necessary amplitude values for these functions, however, due to the inaccuracies of RANS solutions, it is also necessary to calibrate the jet noise model inputs, through model constants. As vast databases of local turbulent properties, for a wide range of nozzles and flow conditions, do not exist (and are indeed impractical), calibration is based on far-field spectra or directivity.

As has be shown in chapter 5, such calibration of statical flow properties shifts the jet source region, and therefore, the source location is effectively driven by far-field values in order to compensate for the deficiencies in the RANS solution. The true *predictive* ability of RANS dependent jet models must be questioned. It could be argued that such models are, in a sense, more of an interpolation method for use with far-field databases, and it may be more logical to simply interpolate the databases directly. A comparison of the *true* capabilities of various jet noise models to predict far-field values should only be undertaken with measured local statistical values, which are the same in each model (without calibration constants).

Even if RANS dependent models are acceptable for far-field isolated predictions, their inherent source-location uncertainty (at least at low frequencies) is more of an issue when an acoustic shield, located in the near-field, is of interest. As has been shown in section 5.3.3, for the shielding configuration investigated, the direction of peak shielding is quite sensitive to the location of the equivalent jet noise sources. That said, however, a shift in source location still does not explain the over-prediction in shielding levels, although it is important to consider its influence on predictions, as in case of comparing different shielding predictions from different jet models.

For high-frequency jet noise, the problem is somewhat less ambiguous, as regardless of the jet noise models, it can be expected that the equivalent source region is adjacent to the nozzle exit. Different noise models, may predict different noise directivity patterns, however, it would appear that the directivity of the jet noise is not overly important to shielding predictions – at least not as much as source location.

The disagreement of the model predictions with the NACRE data can not sim-

ply be attributed to the particularities of the jet models. However, the assumption that equivalent jet sources could be evaluated from the isolated mean flow profile may still be erroneous.

6.1.2 Alternative Propagation Paths

It has been assumed in this present work that the shielded noise has not been reflected by other objects present in the NACRE tests back towards the far-field receivers. This assumption neglects the potential of the large nozzle body to influence the acoustic field. Jet noise impinging on the nozzle directly will not have a significant influence on the shielding effect, as the nozzle is present in both the isolated and installed configurations. If anything it should lead to increased shielding levels, as a source will appear to be located directly over the shield. However, sound, which has been scattered back from the upper surface of the shield, may be reflected by the nozzle body towards the far-field receivers once more. It may also be the case that the Fresnel-Kirchhoff method (FKM) shielding predictions over-simplify the EUROPIV shield geometry (as the FKM can only consider flat surfaces as shields). Figure 6.2 shows the nozzle and EUROPIV locations, as they have been included in a 3D wave expansion method (WEM) computation.

Figure 6.3 shows a comparison of the shielding factors obtained from a single $4kHz$ monopole point source located on the jet axis above varying shield geometries. As can be observed the aerofoil and flap does not achieve the levels of shielding predicted for a flat surface, however, this loss in shielding is still not comparable with the NACRE data, and high shielding levels are expected directly below the shield. It must also be remembered that the approximation of the aerofoil as a flat surface is more appropriate at higher frequencies than that computed here, and therefore, the difference observed here is expected to be less at higher frequencies.

Also in figure 6.3, are shielding predictions that include the side-plates and side-beams (the full EUROPIV), and the nozzle body. These have a relatively small impact on the predicted shielding level. It should also be noted that in this present 3D WEM computation the surfaces are modelled as hard walls (a Neumann boundary condition of $d\phi/d\mathbf{n} = 0$), whereas the side-plates were coated in an acoustic

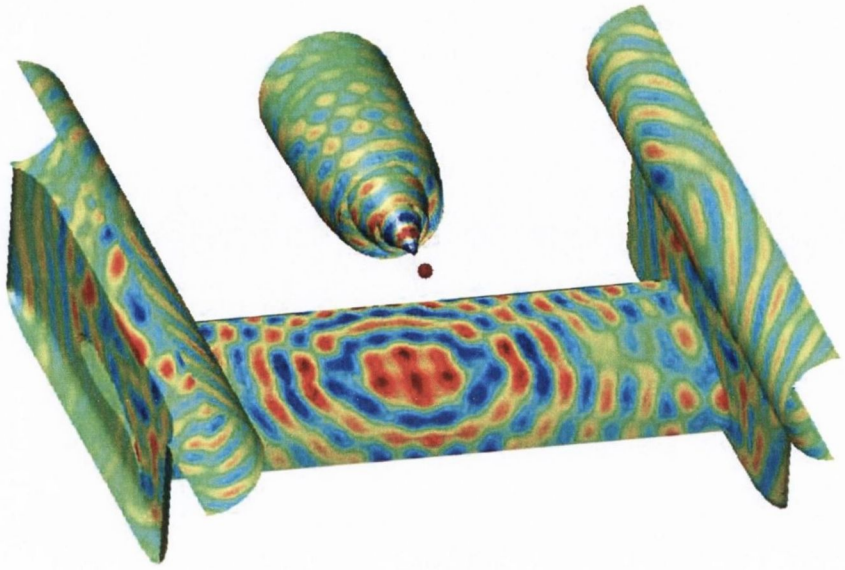

Figure 6.2: 3D WEM solution for a $4kHz$ monopole point source located on the jet axis over the EUROPIV with the nozzle present.

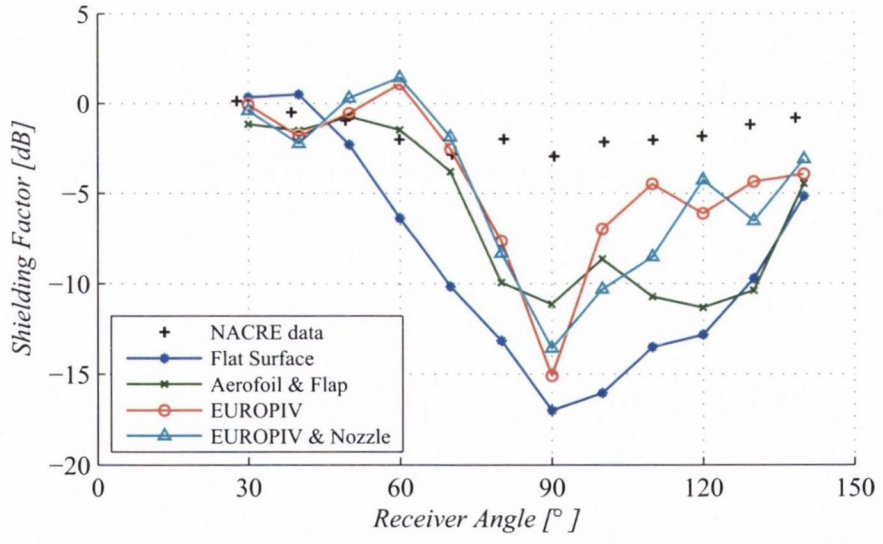

Figure 6.3: Shield approximations: shielding factors from a $4kHz$ monopole point source located on the jet axis above the shield, computed using the 3D WEM. The shielding factor has been averaged over 10° intervals to remove the interference pattern.

absorbing foam in the NACRE tests to reduce reflections. It would, therefore, seem unlikely that the poor shielding levels in NACRE test are due to the sound propagating to the far-field receivers by reflecting from objects not considered in the FKM predictions.

It could also be suggested that the unsteady turbulence itself reflects the sound back towards the receivers in the same manner as the nozzle body. Cerviño *et alia* [25] showed in their numerical perturbation simulations that some back-scatter may be observed from a sound waves impinging on unsteady vortex roll-up. However, given the limited effect on the shielding factor that multiple reflections off the nozzle body had, it would seem extremely unlikely that any reflections off the turbulence would have the amplitude to play a significant role in the NACRE test.

6.1.3 Near-Field Shield Location Effects

The poor shielding levels observed in the NACRE test data are thought to be due to the position of the acoustic shield in the near-field of the jet. This configuration may have had the following unforeseen effects:

Shield Generated Flow Noise

The EUROPIV shield was possibly located close enough to the jet to interfere with its flow entrainment. Figure 6.4 shows a 2D RANS solution for the configuration under investigation. It can clearly be observed that the flow increases in velocity across the top surface of the shield due to entrainment by the jet. A typical entrainment velocity profile, for an isolated nozzle, is still evident at the top lip of the nozzle.

Of greater relevance to present question is that, it is indicated in this figure, from the turbulent kinetic energy, that a source may be generated at the leading-edge of the EUROPIV and also at the trailing-edge of the main foil. It is acknowledged that the 2D nature of this computation may exaggerate such an effect, and it is difficult to estimate the relative amplitude of a leading-edge source. As an initial indication of the impact that a source in this location may have on the shielding factor, figure 6.5 shows the shielding predictions of the NACRE jet, using Model$_C$ and the

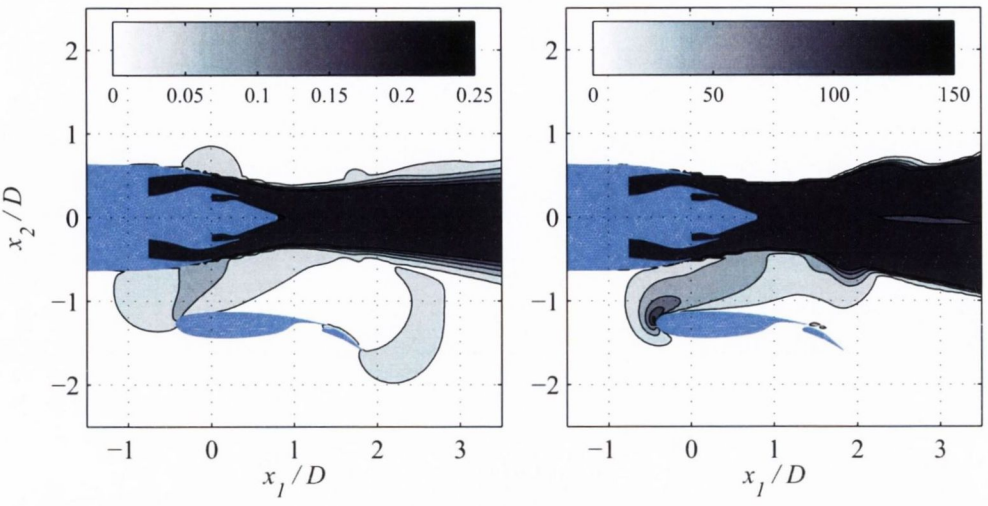

Figure 6.4: Shield generated noise: 2d $\kappa - \epsilon$ RANS solution of the installed NACRE configuration with Mach number (left) and turbulent kinetic energy $[m^2/s^2]$ (right).

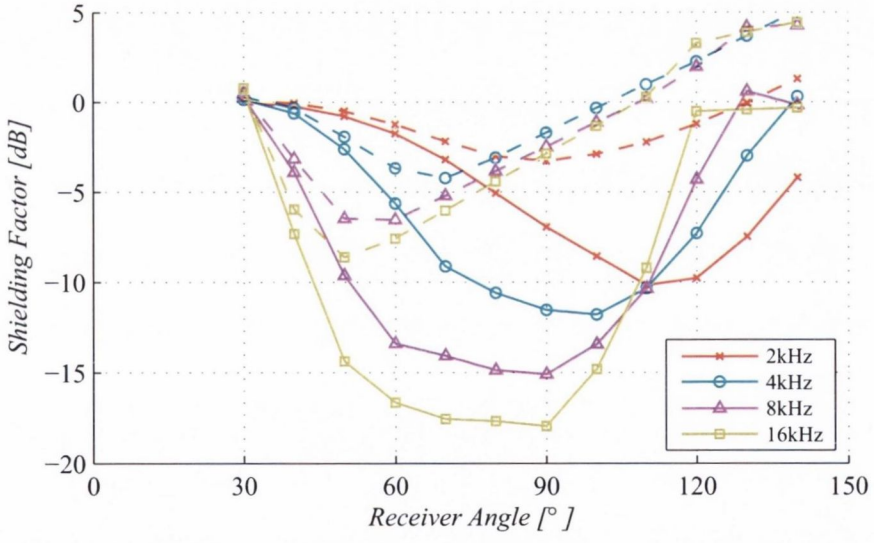

Figure 6.5: Shield generated noise: far-field shielding factor $[dB]$ directivity with $(--)$ and without $(-)$ an isolated source at the leading-edge of the shield. The amplitude of this source is only one-percent of the total jet source model amplitude.

FKM, with an additional isolated source at the leading edge location. The source strength here is just one-percent of the total source amplitude for each frequency. This is an unrealistic source as any noise generated by this mechanism would vary in location for different frequencies but it does help illustrate the point. It may seen that a considerable loss in shielding is predicted. Although this computation is quite crude, and has also changed the direction of peak shielding, it does show that any source with a clear line-of-sight to the far-field receivers would have a considerable impact on the shielding levels.

In his 1981 paper, Wang [90] examined experimentally the effects of the wing on jet noise propagation for an under-wing installation. He states that

> The boundary layer generated on the surface of the wing as the result of entrainment of the air into the region between the wing and the jet is believed to be responsible for the low-frequency noise enhancement

In addition to this boundary layer noise, a trailing-edge source, as indicated in Figure 6.4, would contribute to increased high-frequency noise. It would, therefore, seem most likely that the inclusion of additional *installation* sources is responsible for the differences between predicted and test shielding levels. The shielding factor is sensitive to contamination from additional sources.

Near-Field Excitation

Tinney and Jordan [85] have recently described an evanescent acoustic field, which dominates measurements of the irrotational hydrodynamic periphery of (coaxial) jets. This field is driven by the large-scale turbulent structures. The existence this field has been recognised for some time, and as far back as 1960, Howes [49] discussed how a microphone in the near-field will be subject to fluctuations associated with incompressible "pseudo-sound", which does not propagate, and compressible propagating sound waves. However, there is no indication in the literature of how the insertion of an object in, or near, this field influences the far-field sound. Indeed, it should be remembered that there is no consensus on large scale jet structures themselves (see section 3.1 or reference [51]).

It is speculated that the presence of the EUROPIV in the NACRE test may have scattered some of these waves to the far-field. This effectively means that additional sources may be present, which have not been included in the present shielding methodologies. Once again, any additional small amplitude source, located in a disadvantages position, could be responsible for a dramatic reduction in shielding levels.

Back-Scatter Source Amplification

The location of the acoustic shield near to the jet may alter the jet source terms themselves. It may be possible that the back-scatter from the shield increases the term $\overline{\rho}u_i u_j$. Not only would this amplify the shielded source but may also change the source locations. As the order-of-magnitude of this effect in not available from the published literature, its influence on the measured shielding levels can not be assessed at this point.

6.1.4 Pylon Effects

One remaining object present in the NACRE tests, which has not been included in the present assessment, is the nozzle pylon. Although the NACRE test established that rotating the pylon position has little effect on the shielding factor, whether or not the presence of pylon generates noise itself, which contaminates the shadow zone below the shield, has not been clarified.

The best available indicator of the influence of the pylon, is from comparing the data with NACRE's predecessor, the EU FP5 funded Research on Silent Aircraft Concepts (ROSAS) project [32], where a wind-tunnel test programme was performed for a very similar shielding configuration with a jet simulator that had no pylon. Although the observed shielding levels were marginally greater than those measured in the NACRE test, they were still unexpectedly small. It seems unlikely, from comparing these sets of data, that the poor shielding levels can simply be attributed to pylon effects.

6.2 Remaining Considerations

6.2.1 Increasing the Shielded Amplitude

The suggestion that the shielded source is somehow greater in amplitude than the isolated source must tempered against the fact that the test data does not show any significant levels of amplification. If, for example, the amplitude of the modelled small-scale jet noise sources, which have been considered in this present work, was to be uniformly increased in the shielded case, then the shielding predictions would simply be shifted in the positive direction, and positive shielding factors (amplification) might be evident. As this is not to found in the data, the overall acoustic power from the noise source region must remain reasonably constant, between the isolated and shielded configurations. Additional noise sources introduced into the shielded case would have to be small in magnitude.

The crucial factor in the effectiveness of shielding a turbulent jet is, therefore, the location of all the noise sources. The shielding factor is sensitive to the introduction of small amplitude sources, which could be generated by any of, or a combination of, the reasons discussed in the previous section.

6.2.2 Two Frequency Regimes

It may be beneficial to the assessment of jet noise shielding to define to distinct problems – low-frequency and high-frequency jet noise shielding. As has been discussed in this present work, there are significant challenges in identifying the location of low-frequency jet noise, which is paramount to shielding it. Also, low-frequency noise is not amenable to this reduction technique, in the first place, due to its distributed nature, and its long wavelength.

Referring back to the source location map in figure 5.8, it may observed that the jet transitions quite rapidly from a low-frequency distributed source to a high-frequency relatively concentrated source. The possibility of achieving reductions in the high-frequency content of the jet noise are much more realistic from a physical point-of-view, than from low-frequency noise sources. High-frequency jet noise shielding may also have a greater susceptibility to small amplitude contamination

of the shield shadow zone, than low frequency noise.

This quite subtle distinction, of two frequency regimes, which is commonly used to distinguish propagation methods, may be of benefit when considering the source itself and the shielding concept as a whole, as it would guide the design of experiments and the selection of modelling methods. In a broader context, this abstraction may assist in combining aircraft engine noise issues, like core-noise, the use of nozzle chevrons, *et cetera*, with "high-frequency jet noise", into a group of noise source types where shielding gains might be achieved.

6.2.3 Is Jet Noise Shielding a Practical Possibility?

The use of the airframe as a shield to reduce the jet noise, which propagates towards the ground, must be questioned as a plausible concept for two reason. Firstly, the possible generation of installation sources may largely negate any reduction that might be expected if the jet noise source was not effected by the introduction of the shield. This problem might not be as significant when an external flow is present, as the jet flow would be more axially compact and so interact less with the shield.

Secondly, the proposed shielding configurations are essentially low-Helmholtz number problems. Jet noise is predominantly low-frequency (see the measured spectrum in Figure 5.9), where the source is distributed over a large spatial region, and is, therefore, difficult to shield. The higher frequency content, may be more amenable to shielding, but also dissipates more readily as propagates through the atmosphere naturally. This situation may change with the introduction of technology, such as chevrons, to alter the frequency content of jet noise.

6.2.4 The Shielding Factor as a Measure?

The shielding factor compares the decibel difference between an installed shielded configuration and an isolated jet. Any true assessment of the benefits of a proposed shielding configuration, must be compared with the present under-wing installations, which enhance noise propagation towards the ground. The installed shielded configuration should be offset against the installed under-wing configuration. Jets

are *never* isolated.

An underlying assumption of the jet noise shielding concept, to-date, is that a reduction in the far-field sound pressure levels would be a positive achievement. How new configurations impact the *perceived* noise levels has only been considered to a very limited extent. The shielding factor takes no account of how the *quality* of the jet noise may be changed by the presence of the shield, and how the sound is perceived by the only receiver of true consequence – the human ear. The shielding factor is possibly too crude to truly assess jet noise shielding configurations.

6.3 New Areas of Interest

It has been found that the far-field reduction in the SPL levels from a turbulent jet, achieved by the installation of acoustic shield in the near-field, does not match the expectations of the predicted values. It would appear that the positioning of the shield may have had a number of unforeseen side-effects, which merit investigation.

Focused tests should be conducted, in which the shield is removed sufficiently from the jet so as to avoid the complications that have been discussed in section 6.1. It would also be highly beneficial to do these test with a fundamental jet shielding configuration – a single jet with a flat plate as a shield.

The jet noise should be measured both in a shielded configuration and in an *under-wing* configuration so as to assess the improvement that shielded configurations may have over traditional under-wing installation.

More near-field data is required, for both isolated and installed jets, to assist in source location, and to evaluate the evanescent acoustic field. Jet noise shielding models must successfully predict this simple shielding setup before it can be hoped to predict realistic installed configurations.

A useful benchmark would be to predict the shielding from a small ideal loudspeaker source at various locations with the jet off (but the nozzle present). Data on the interaction effect between an exterior source and the jet would also aid jet noise shielding assessment.

It would be of great interest to examine the transition effect of progressively

moving the shield from a far-field position into the near-field of the jet. This would provide substantial insight into both the location of the noise sources and the probable generation of additional noise sources. Indeed, it would also be of benefit to map the isolated jet field by moving the microphones progressively closer to the jet.

More installed flow computations are needed, and perhaps a comparison between the near flow fields from a RANS computation and a LES computation, of simple shielded configurations.

Chapter 7

Conclusions

- A jet noise model has been derived, which is a combination of traditional aeroacoustic models based on Lighthill's analogy and, the more recent, Tam-Auriault model. This model has been used to locate directional point source distributions.
- The predicted isolated far-field sound pressure levels, from these source distributions, agree well with the NACRE data.
- Present methodologies to predict the far-field shielding levels, from an installed jet configuration, fail to reproduce the NACRE data values.
- An axial source distribution is sufficient to represent the spatial volume of the jet in shielding predictions.
- A scheme has been presented to divide the jet noise source region into sub-volumes. This reduces the computational demand for far-field noise predictions, without adversely effecting accuracy.
- Identification of source locations is critical to noise shielding predictions, whereas source directivity is mildly important.
- Although isolated far-field jet noise models may be relatively robust to the inherent deficiencies in RANS flow solutions, installed far-field predictions appear to be quite sensitive to these shortcomings.

- The unexpectedly low shielding levels, observed at high frequencies in the NACRE data, are most likely due to near-field effects resultant from the introduction of the shield, which have not included in present shielding methodologies. The assumption that the noise source is the same for both the isolated and installed configurations is mostly likely invalid.

- There is a need for focused shielding experiments with simple jet and shield configurations. More near-field data is required for both isolated and installed jets.

- There is a need for more investigations into the near-field interactions between the jet noise source and the shielding object.

- It may be beneficial to future aircraft engine noise research to consider two separate frequency regimes in the jet noise source.

- The use of the shielding factor as a criteria to judge shielding configurations is questionable, and a metric is required, which considers perceived noise attenuation.

- The shielding factor is quite sensitive to contamination from sources introduced with the introduction of the shield.

Appendix A

The Wave Expansion Method

A.1 In Inhomogeneous, Irrotational, Steady Flows

If the mean flow is assumed to be irrotational and inhomogeneous then it can be modelled as a potential flow, and the governing field equation for the velocity potential, ϕ is given by

$$\frac{1}{\overline{\rho}}\nabla.\left(\overline{\rho}\,\nabla\phi\right) - L\left(\frac{1}{\overline{c}^{\,2}}L\phi\right) = 0\,, \tag{A.1}$$

where L is the complex linear operator $(i\omega + \overline{\mathbf{u}}.\nabla)$ and $\overline{\mathbf{u}}$, $\overline{\rho}$, $\overline{c}$, are the local mean velocity, density, and speed of sound respectively. The development of a solution to equation (A.1) begins with expanding the equation such that

$$\nabla^2\phi - \left(\mathbf{M}.\nabla\right)^2\phi - \mathbf{B}.\nabla\phi + K^2\phi = 0\,, \tag{A.2}$$

where

$$\mathbf{B} = 2ik\mathbf{M} + \overline{\mathbf{u}}.\nabla\left(\frac{1}{\overline{c}^{\,2}}\right)\overline{\mathbf{u}} + \frac{1}{\overline{c}^{\,2}}\overline{\mathbf{u}}.\nabla\,\overline{\mathbf{u}} - \frac{1}{\overline{\rho}}\nabla\,\overline{\rho}\,, \tag{A.3}$$

$$K^2 = \frac{\omega^2}{\overline{c}^{\,2}} - i\omega\,\overline{\mathbf{u}}.\nabla\frac{1}{\overline{c}^{\,2}}\,, \tag{A.4}$$

and where $\mathbf{M} = \overline{\mathbf{u}}/\overline{c}$.

If $\mathbf{x_0}$ is centre point in a small domain covering any stencil of the entire computational lattice, it follows that

$$\nabla^2\phi_0 - \left(\mathbf{M_0}.\nabla\right)^2\phi_0 - \mathbf{B_0}.\nabla\phi_0 + K_0^2\,\phi_0 = 0\,, \tag{A.5}$$

where $\mathbf{B_0} = \mathbf{B}(\mathbf{x_0})$, $K_0^2 = K^2(\mathbf{x_0})$ and $\mathbf{M_0} = \mathbf{M}(\mathbf{x_0})$ are constant coefficients.

Equation (A.5) is a constant coefficient, homogeneous, linear, second-order differential equation, which may be solved by, firstly, defining the characteristic equation

$$\left(1 - (\mathbf{M_0}.\mathbf{d})^2\right) R^2 - (\mathbf{B_0}.\mathbf{d})\, R + K_0^2 = 0\,, \tag{A.6}$$

where $\mathbf{d}$ is an arbitrary real unit vector. The roots of this equation are

$$R = \frac{\mathbf{B_0}.\mathbf{d} \pm \sqrt{(\mathbf{B_0}.\mathbf{d})^2 - 4K_0^2\left(1 - (\mathbf{M_0}.\mathbf{d})^2\right)}}{2\left(1 - (\mathbf{M_0}.\mathbf{d})^2\right)}\,, \tag{A.7}$$

and defining

$$q = iR = \frac{i\mathbf{B_0}.\mathbf{d} \pm \sqrt{4K_0^2\left(1 - (\mathbf{M_0}.\mathbf{d})^2\right) - (\mathbf{B_0}.\mathbf{d})^2}}{2\left(1 - (\mathbf{M_0}.\mathbf{d})^2\right)}\,. \tag{A.8}$$

Therefore a fundamental plane wave solution, ϕ_0, can be expressed as

$$\phi_0 = \exp\left[-iq\,(\mathbf{d}.\mathbf{x_0})\right]\,. \tag{A.9}$$

If the terms involving gradients in $\mathbf{B}$ and K^2 are neglected, which assumes that the nodal spacing in the computational lattice is small, then $\mathbf{B} = 2ik\mathbf{M}$ and $K^2 = k^2 = \omega^2/\bar{c}^{\,2}$. Therefore, equation (A.8) reduces to

$$q = k\frac{\pm 1 - \mathbf{M_0}.\mathbf{d}}{(1 + \mathbf{M_0}.\mathbf{d})\,(1 - \mathbf{M_0}.\mathbf{d})}\,, \tag{A.10}$$

and so equation (A.9) can be expressed simply as

$$\phi_0 = \exp\left[\frac{-ik\,(\mathbf{d}.\mathbf{x_0})}{1 + \mathbf{M_0}.\mathbf{d}}\right]\,. \tag{A.11}$$

A.2 Wave Expansion Discretisation

The velocity potential at a discrete point, ϕ_0, (and so the acoustic pressure) may be computed from the amplitude and phase of M neighbouring points. The potential at each point in a domain may be approximated by the superposition of the field

generated by N hypothetical plane waves of strength γ_n and with unit propagation in direction $\mathbf{d}_n$ such that

$$\phi_0 = \sum_{n=1}^{N} \gamma_n \exp\left[-iq\left(\mathbf{d}.\mathbf{x_0}\right)\right] = \mathbf{h}\boldsymbol{\gamma}\,, \tag{A.12}$$

where $h_n = \exp\left[-iq\left(\mathbf{d}.\mathbf{x_0}\right)\right]$. Similarly, the velocity potential at a neighbouring point, $\mathbf{m}$, in the computational lattice, where $\mathbf{m} = 1, 2, .., M$, is given as

$$\boldsymbol{\phi}_\mathbf{m} = \sum_{n=1}^{N} \gamma_n \exp\left[-iq\left(\mathbf{d}.\mathbf{x_m}\right)\right] = \mathbf{H}\boldsymbol{\gamma}\,. \tag{A.13}$$

If $\mathbf{H}^+$ is the pseudo-inverse of $\mathbf{H}$ then

$$\boldsymbol{\gamma} = \mathbf{H}^+\boldsymbol{\phi}_\mathbf{m}\,, \tag{A.14}$$

and substituting this back into equation (A.12) leads to

$$\phi_0 - \mathbf{h}\mathbf{H}^+\boldsymbol{\phi}_\mathbf{m} = 0\,. \tag{A.15}$$

If the he local stiffness vector for a computational lattice is $\kappa_0 = -\mathbf{h}\mathbf{H}^+$, then

$$\phi_0 + \kappa_0\boldsymbol{\phi}_\mathbf{m} = 0\,, \tag{A.16}$$

which may be rewritten as

$$\left\{\begin{array}{cc} 1 & \kappa_0 \end{array}\right\} \left\{\begin{array}{c} \phi_0 \\ \boldsymbol{\phi}_\mathbf{m} \end{array}\right\} = 0\,. \tag{A.17}$$

For the total computational domain, with a source vector, $\mathbf{f}$, added to the right-hand-side and where $\boldsymbol{\kappa}$ is the overall stiffness matrix, a linear system of equations may be defined of the form

$$\boldsymbol{\kappa}\boldsymbol{\phi} = \mathbf{f}\,. \tag{A.18}$$

This may, with the addition of appropriate boundary conditions, be solved for $\boldsymbol{\phi}$, a vector containing the velocity potential at each point in the overall computational lattice.

A.3 Implementation of WEM Boundary Conditions

The implementation of boundary conditions for this numerical method may implemented as follows

Dirichlet

Dirichlet boundary conditions may be implemented in the WEM by simply constraining the appropriate entries in the overall stiffness matrix.

Natural Radiation

Natural radiation boundary conditions can be imposed by only selecting the plane waves travelling out of the domain when assembling the stiffness matrix for points on the boundary. Equation (A.16) for natural radiation boundary points becomes

$$\phi_{\mathbf{0}} + \kappa_{\mathbf{0},natrad}\, \phi_{\mathbf{m}} = 0\,. \tag{A.19}$$

Neumann

To impose the normal velocity of a boundary point as

$$\frac{\partial \phi_B}{\partial \mathbf{n}} = \mathbf{v}_B\,, \tag{A.20}$$

where $\mathbf{n}$ is a unit vector normal to the boundary, equation (A.13) is augmented by each Neumann boundary point, so that

$$\left\{ \begin{array}{c} \phi_{\mathbf{m}} \\ \mathbf{v}_B \\ \vdots \end{array} \right\} = \left[\begin{array}{c} \mathbf{H} \\ \partial \mathbf{h}_B / \partial \mathbf{n}_m \\ \vdots \end{array} \right] \{\gamma\} = \mathbf{H}_{aug} \gamma\,. \tag{A.21}$$

Taking the pseudo-inverse of $\mathbf{H}_{aug}$

$$\gamma = \left[\mathbf{H}^{+}_{aug}\right] \left\{ \begin{array}{c} \phi_{\mathbf{m}} \\ \mathbf{v}_B \end{array} \right\}, \tag{A.22}$$

equation (A.15) may be partitioned, and so becomes

$$\phi_{\mathbf{0}} = \mathbf{h} H^{+}_{aug,L}\, \phi_{\mathbf{m}} + \mathbf{h} H^{+}_{aug,R}\, \mathbf{v}_B\,. \tag{A.23}$$

Bibliography

[1] M. Afsar, A. P. Dowling, and S. A. Karabasov. Comparison of jet noise models. *AIAA/CEAS 12th Aeroacoustics Conference (Cambridge, Massachusetts, USA)*, 2006. AIAA-2006-2593.

[2] A. Agarwal, A. P. Dowling, H. Shin, W. Graham, and S. Sefi. A ray tracing approach to calculate acoustic shielding by the silent aircraft airframe. *AIAA/CEAS 12th Aeroacoustics Conference (Cambridge, Massachusetts, USA)*, 2006. AIAA-2006-2618.

[3] Airbus. Global market forecast: 2007–2026. *Airbus (Toulouse , France)*, 2007.

[4] M. B. Allen, I. Herrera, and G. F. Pinder. *Numerical simulation in science and engineering.* John Wiley and Sons, 1988.

[5] C. Bailly and D. Juvé. A stochastic approach to compute subsonic-noise using linearized Eulers equations. *AIAA/CEAS 5th Aeroacoustics Conference (Seattle, Washington, USA)*, pages 496–506, 1999. AIAA-1999-1872.

[6] C. Bailly and D. Juvé. Numerical solution of acoustic propagation problems using linearized Euler equations. *AIAA journal*, 38(1):22–29, 2000.

[7] W. Béchara, C. Bailly, P. Lafon, and S. M. Candel. Stochastic approach to noise modelling for free turbulent flows. *AIAA Journal*, 32(3):455–463, 1994.

[8] W. Béchara, P. Lafon, and C. Bailly. Application of κ-ϵ turbulence model to the prediction of noise for simple and coaxial free jets. *Journal of the Acoustical Society of America*, 97(6):3518–3531, 1995.

[9] B. Bergland, T. Lindvall, and D. H. Schwela. Guidelines for community noise. *World Health Organization (Geneva, Switzerland)*, 1999.

[10] M. Billson, L. Eriksson, and L. Davidson. Jet noise prediction using stochastic turbulence modeling. *AIAA/CEAS 9th Aeroacoustics Conference (Hilton Head, South Carolina, USA)*, 2003. AIAA-2003-3282.

[11] M. Billson, L. Eriksson, and L. Davidson. Jet noise modeling using synthetic anisotropic turbulence. *AIAA/CEAS 10th Aeroacoustics Conference (Manchester, Britain)*, 2004. AIAA-2004-3028.

[12] M. Billson, L. Eriksson, L. Davidson, and P. Jordan. Modeling of synthetic anisotropic turbulence and its sound emission. *AIAA/CEAS 10th Aeroacoustics Conference (Manchester, Britain)*, 2004. AIAA-2004-2857.

[13] D. Blackstock. *Fundamentals of physical acoustics*, chapter 14, pages 472–494. Wiley-Interscience, 2000.

[14] Boeing. Summary outlook: 2008–2027. *Boeing (Seatle, Washington, USA)*, 2008.

[15] C. Bogey and C. Bailly. Investigation of sound sources in subsonic jets using causality methods on LES data. *AIAA/CEAS 11th Aeroacoustics Conference (Monterey, California, USA)*, 2005. AIAA-2005-2886.

[16] C. Bogey, C. Bailly, and D. Juvé. Noise investigation of a high subsonic, moderate Reynolds number jet using a compressible large eddy simulation. *Theoretical and Computational Fluid Dynamics*, 16(4):273, 2003.

[17] M. Bonnet. *Boundary integral methods for solids and fluids.* John Wiley and Sons, 1995.

[18] J. J. Bowman, T. B. A. Senior, and P. L. E. Uslenghi. *Electromagnetic and acoustic scattering by simple shapes*, chapter 1. Hemisphere Publishing, 1987.

[19] C. A. Brebbia. *The boundary element method for engineers.* Pentech Press, London, 1978.

[20] G. Brown and A. Roshko. On density effects and large-scale structure in turbulent mixing-layers. *Journal of Fluid Mechanics*, 64, 1974.

[21] Greener by Design. Air travel – greener by design: the challenge. *Greener by Design*, 2001.

[22] J. E. Caruthers, R. C. Engels, and G. K. Ravinprakash. A wave expansion computational method for discrete frequency acoustics within inhomogeneous flows. *AIAA/CEAS 2nd Aeroacoustics Conference (State College, Pennsylvania, USA)*, 1996. AIAA-1996-1684.

[23] J. E. Caruthers, J. C. French, and G. K. Ravinprakash. Greens function discretization for a numerical solution of the Helmholtz equation. *Journal of Sound and Vibration*, 187(4):553–568, 1995.

[24] J. E. Caruthers, J. C. French, and G. K. Ravinprakash. Recent developments concerning a new discretization method for the Helmholtz equation. *AIAA/CEAS 1st Aeroacoustics Conference (Munich, Germany)*, pages 819–826, 1995. AIAA-1995-117.

[25] L. I. Cervino, T. R. Bewley, J. Freund, and S. K. Lele. Perturbation and adjoint analyses of flow-acoustic interactions in an unsteady 2D jet. *Center for Turbulence Research – Proceedings of the summer program*, page 2740, 2002.

[26] F. Coiffet, P. Jordan, J. Delville, Y. Gervais, and F. Ricaud. Coherent structures in subsonic jets: a quasi-irrotational source mechanism? *International Journal of Aeroacoustics*, 5(1):67–89, 2006.

[27] J. C. Cooke. *Notes on the diffraction of sound.* Royal Aircraft Establishment (Great Britain), 1970.

[28] D. G. Crighton and P. Huerre. Shear layer pressure fluctuations and superdirective acoustic sources. *Journal of Fluid Mechanics*, 220, 1990.

[29] S. C. Crow and F. H. Champagne. Orderly structure in jet turbulence. *Journal of Fluid Mechanics*, 48(3):547–591, 1971.

[30] P. A. O. L. Davies, M. J. Fisher, and M. J. Barratt. The characteristics of the turbulence in the mixing region of a round jet. *Journal of Fluid Mechanics*, 15(3):337–367, 1963.

[31] R. Davy. Report on powered tail acoustic shielding WTT – Jet noise part. Technical report, EU FP6 NACRE Project – Deliverable 3.1-13A, 2007.

[32] W. Denis and R. Davy. Shielding effects on jet noise – preliminary report. Technical report, EU FP5 ROSAS Project – Technical Report No. RT 2/07065 DSNA, 2003.

[33] W. J. Devenport, C. Muthanna, R. Ma, and Glegg S. A. L. Two-point descriptions of wake turbulence with application to noise prediction. *AIAA Journal*, 39(12):2302–2307, 2001.

[34] A. P. Dowling and J. E. Ffowcs Williams. *Sound and sources of sound*, chapter 9. Ellis Horwood, 1983.

[35] European Commission. Position paper on dose-effect relationship for night time noise. *European Commission Working Group on Health and Socio-Economic Aspects*, 2004.

[36] European Union. Directive 2002/49/EC of the European Parliament and of the Council of 25 June 2002 relating to the assessment and management of environmental noise. *Official Journal of the European Communities*, 2002.

[37] R. Ewert. RPM - the fast random particle-mesh method to realize unsteady turbulent sound sources and velocity fields for CAA applications. *AIAA/CEAS 13th Aeroacoustics Conference (Rome, Italy)*, 2007. AIAA-2007-3506.

[38] F. Farassat, S. L. Padula, and M. H. Dunn. Advanced turboprop noise prediction based on recent theoretical results. *Journal of Sound and Vibration*, 119:53–79, 1987.

[39] R. T. Fenner. *Finite element methods for engineers*. Imperial College Press, London, 1996.

[40] J. B. Freund. Noise sources in a low-Reynolds-number turbulent jet at Mach 0.9. *Journal of Fluid Mechanics*, 438:277–305, 2001.

[41] H. V. Fuchs. Space correlations of the fluctuating pressure in subsonic turbulent jets. *Journal of Sound and Vibration*, 23(1):77–99, 1972.

[42] M. B. Giles and N. A. Pierce. Adjoint equations in CFD: duality, boundary conditions and solution behaviour. *AIAA 13th Computational Fluid Dynamics Conference (Snowmass Village, Colorado, USA)*, 1997. AIAA-1997-1850.

[43] M. E. Goldstein. *Aeroacoustics*, chapter 2. McGraw-Hill International Book, 1976.

[44] M. E. Goldstein and S. J. Leib. The role of instability waves in predicting jet noise. *Journal of Fluid Mechanics*, 525:37, 2005.

[45] M. E. Goldstein and B. Rosenbaum. Effect of anisotropic turbulence on aerodynamic noise. *Journal of the Acoustical Society of America*, 54(3):630–645, 1973.

[46] M. M. Haines, S. A. Stansfeld, S. Brentnall, J. Head, B. Berry, M. Jiggins, and S. Hygge. The west London schools study: the effects of chronic aircraft noise exposure on child health. *Psychological Medicine*, 31:1385–1396, 2001.

[47] M. S. Howe. Contribution to the theory of aerodynamic sound, with application to excess jet noise and the theory of the flute. *Journal of Fluid Mechanics*, 71(4):625–673, 1974.

[48] M. S. Howe. *Acoustics of fluid-structure interactions*. Cambridge University Press, 1998.

[49] W. L. Howes. Distribution of time-averaged pressure fluctuations along the boundary of a round subsonic jet. Technical report, NASA Technical Note D-468, 1960.

[50] P. Jordan and Y. Gervais. Modelling self- and shear-noise mechanisms in inhomogeneous, anisotropic turbulence. *Journal of Sound and Vibration*, 279:529–555, 2005.

[51] P. Jordan and Y. Gervais. Subsonic jet aeroacoustics: associating experiment, modelling and simulation. *Experiments in Fluids*, 44(1):1, 2007.

[52] D. Jung, S. Gamard, and W. K. George. Downstream evolution of the most energetic modes in a turbulent axisymmetric jet at high Reynolds number. Part 1 – the near-field region. *Journal of Fluid Mechanics*, 514:173–204, 2004.

[53] A. Khavaran. Role of anisotrpy in turbulent mixing noise. *AIAA Journal*, 37(7):832–841, 1999.

[54] V. F. Kopiev, M. Y. Zaitsev, S. A. Chernyshev, and A. N. Kotova. The role of large-scale vortex in a turbulent jet noise . *AIAA/CEAS 5th Aeroacoustics Conference and Exhibit (Bellevue, Washington, USA)*, 1999. AIAA-1999-1839.

[55] J. C. Lau, M. J. Fischer, and H. V. Fuchs. The intrinsic structure of turbulent jets. *Journal of Sound and Vibration*, 22(4):379–406, 1972.

[56] J. Laufer and T. C. Yen. Noise generation by a low-Mach-number jet. *Journal of Fluid Mechanics*, 134:1–31, 1983.

[57] M. J. Lighthill. On sound generated aerodynamically Part I. General theory. *Proceedings of the Royal Society of London, Series A*, 211:564–587, 1952.

[58] M. J. Lighthill. On sound generated aerodynamically Part II. Turbulence as a sound source. *Proceedings of the Royal Society of London, Series A*, 222:1–32, 1954.

[59] G. M. Lilley. On the noise from air jets. *British Aeronautical Research Council 20*, 376(40), 1958.

[60] G. M. Lilley. On the noise from jets. *AGARD Conference Proceedings*, 131(13), 1974.

[61] G. M. Lilley. The radiated noise from isotropic turbulence with applications to the theory of jet noise. *Journal of Sound and Vibration*, 190(3):463, 1996.

[62] M. Lummer. Maggi-Rubinowicz diffraction correction for ray-tracing calculations of engine noise shielding. *AIAA/CEAS 14th Aeroacoustics Conference (Vancouver, British Columbia, Canada)*, 2008. AIAA-2008-3050.

[63] J. Manera, S. Caro, R. Leneveu, and B. Schiltz. Parallel DGM scheme for LEE applied to exhaust and bypass problems. *AIAA/CEAS 13th Aeroacoustics Conference (Rome, Italy)*, 2007. AIAA-2007-3510.

[64] W. Möhring. On vortex sound at low Mach number. *Journal of Fluid Mechanics*, 85, 1978.

[65] P. J. Morris and F. Farassat. Acoustic analogy and alternative theories for jet noise prediction. *AIAA Journal*, 40(4):671–680, 2002.

[66] P. J. Morris and F. Farassat. Reply by the authors to C. K. W. Tam. *AIAA Journal*, 41(9):1845–1847, 2003.

[67] NACRE. New Aircraft Concepts Research. `cordis.europa.eu/fp6`.

[68] World Health Organization. WHO technical meeting on aircraft noise and health. *World Health Organization (Bonn, Germany)*, 2001.

[69] A. Pierce. Wave equation for sound in fluids with unsteady inhomogeneous flow. *The Journal of the Acoustical Society of America*, 87(6):2292–2299, 1990.

[70] A. Powell. Theory of vortex sound. *Journal of the Acoustical Society of America*, 16:177–195, 1964.

[71] I. Proudman. The generation of noise by isotropic turbulence. *Proceedings of the Royal Society of London, Series A*, 214:119–132, 1952.

[72] H. S. Ribner. On Spectra and Directivity of Jet Noise. *Journal of Acoustical Society of America*, 35:614–616, 1963.

[94] Z. Xiangyang, C. Kean, and S. Jincai. On the accuracy of the ray-tracing algorithms based on various sound receiver models. *Applied Acoustics*, 64(4):433, 2003.

[95] O. C. Zienkiewicz. *The finite element method*, volume 1. McGraw-Hill, London, 1989.